

Impacts of tidally driven internal mixing in the Early Eocene Ocean

Jean-Baptiste Ladant¹, Jeanne Millot-Weil¹, Casimir de Lavergne², Mattias Green³,
Sébastien Nguyen¹, and Yannick Donnadiou⁴

¹Laboratoire des Sciences du Climat et de l'Environnement

²LOCEAN Laboratory, Sorbonne Université-CNRS-IRD-MNHN,

³Bangor University

⁴CEREGE (Centre Européen de Recherche et d'Enseignement des Géosciences de l'Environnement)

December 7, 2023

Abstract

Diapycnal mixing in the ocean interior is largely fueled by internal tides. Mixing schemes that represent the breaking of internal tides are now routinely included in ocean and earth system models applied to the modern and future. However, this is more rarely the case in climate simulations of deep-time intervals of the Earth, for which estimates of the energy dissipated by the tides are not always available. Here, we present and analyze two IPSL-CM5A2 earth system model simulations of the Early Eocene made under the framework of DeepMIP. One simulation includes mixing by locally dissipating internal tides, while the other does not. We show how the inclusion of tidal mixing alters the shape of the deep ocean circulation, and thereby of large-scale biogeochemical patterns, in particular dioxygen distributions. In our simulations, the absence of tidal mixing leads to a deep North Atlantic basin mostly disconnected from the global ocean circulation, which promotes the development of a basin-scale pool of oxygen-deficient waters, at the limit of complete anoxia. The absence of large-scale anoxic records in the deep ocean posterior to the Cretaceous anoxic events suggests that such an ocean state most likely did not occur at any time across the Paleogene. This highlights how crucial it is for climate models applied to the deep-time to integrate the spatial variability of tidally-driven mixing as well as the potential of using biogeochemical models to exclude aberrant dynamical model states for which direct proxies do not exist.

Impacts of tidally driven internal mixing in the Early Eocene Ocean

Jean-Baptiste Ladant¹, Jeanne Millot-Weil^{1,*}, Casimir de Lavergne², J. A. Mattias Green³, Sébastien Nguyen¹, Yannick Donnadiou⁴

¹Laboratoire des Sciences du Climat et de l'Environnement, LSCE/IPSL, CEA-CNRS-UVSQ, Université Paris-Saclay, 91191, Gif-sur-Yvette, France.

²Laboratoire d'Océanographie et du Climat : Expérimentations et Approches Numériques, IPSL, Sorbonne Université/IRD/CNRS/MNHN, Paris, France.

³School of Ocean Sciences, Bangor University, Menai Bridge, UK.

⁴Aix Marseille Université, CNRS, IRD, INRA, Coll France, CEREGE, Aix-en-Provence, France

Corresponding author: Jean-Baptiste Ladant (jean-baptiste.ladant@lsce.ipsl.fr)

*Now at: School of Geographical Sciences, University of Bristol, Bristol, UK.

Key Points:

- Inclusion of realistic near-field tidal mixing substantially modifies global deep ocean circulation in the Early Eocene.
- These tidally-driven changes yield significantly different biogeochemical properties of water masses, in particular in the Atlantic.
- The simulation that includes tidal mixing compares more favorably to inferences from the O₂ proxy record.

34 **Abstract**

35

36 Diapycnal mixing in the ocean interior is largely fueled by internal tides. Mixing schemes that
37 represent the breaking of internal tides are now routinely included in ocean and earth system
38 models applied to the modern and future. However, this is more rarely the case in climate
39 simulations of deep-time intervals of the Earth, for which estimates of the energy dissipated by
40 the tides are not always available. Here, we present and analyze two IPSL-CM5A2 earth system
41 model simulations of the Early Eocene made under the framework of DeepMIP. One simulation
42 includes mixing by locally dissipating internal tides, while the other does not. We show how
43 the inclusion of tidal mixing alters the shape of the deep ocean circulation, and thereby of large-
44 scale biogeochemical patterns, in particular dioxygen distributions. In our simulations, the
45 absence of tidal mixing leads to a deep North Atlantic basin mostly disconnected from the
46 global ocean circulation, which promotes the development of a basin-scale pool of oxygen-
47 deficient waters, at the limit of complete anoxia. The absence of large-scale anoxic records in
48 the deep ocean posterior to the Cretaceous anoxic events suggests that such an ocean state most
49 likely did not occur at any time across the Paleogene. This highlights how crucial it is for
50 climate models applied to the deep-time to integrate the spatial variability of tidally-driven
51 mixing as well as the potential of using biogeochemical models to exclude aberrant dynamical
52 model states for which direct proxies do not exist.

53

54

55 **1. Introduction**

56

57 Tides are the main supplier of diapycnal mixing in the ocean's interior, beneath the surface
58 boundary layers (e.g., Egbert and Ray, 2000; Vic et al., 2019; de Lavergne et al., 2020).
59 Barotropic tidal currents flowing over sloping bottom topography generate internal waves at
60 tidal frequency, called internal tides (Garrett and Kunze, 2007). The propagation, non-linear
61 interaction, and ultimate breaking of internal tides into three-dimensional turbulence constitutes
62 the primary contribution to diapycnal mixing (that is, mixing across isopycnals) and thus to
63 water mass transformation in the deep ocean (de Lavergne et al., 2022; Melet et al., 2022).
64 There are multiple pathways and processes leading to the dissipation of internal tide energy.
65 Small-scale internal tides tend to dissipate close to their generation site, whereas large-scale
66 internal tides dissipate more remotely, sometimes thousands of kilometers away from the
67 generation site (Whalen et al., 2020).

68

69 The modern global overturning circulation is usually schematized as a two-loop system,
70 consisting of an adiabatic upper cell fed by deep convection in the North Atlantic (the NADW)
71 overlying a largely diabatic lower cell fed by Antarctic Bottom Water (AABW) formation in
72 the Southern Ocean (Marshall and Speer, 2012; Talley, 2013; Melet et al., 2022). Diapycnal
73 mixing plays an important role in shaping this two-cell overturning circulation (Cimoli et al.,
74 2023); in particular the tidally-driven, bottom-intensified, part of the mixing is instrumental in
75 reducing the density of northward-flowing AABW and in mixing AABW with NADW (de
76 Lavergne et al., 2022; Melet et al., 2022). It is the specific geometry of the modern Southern
77 Ocean, with its continent-free latitudinal band down to a depth of ~ 2000 m at the Drake
78 Passage, that favors the adiabatic upwelling of deep waters (NADW and Pacific/Indian Deep
79 Waters) in the surface Ekman divergence of the Southern Ocean (Toggweiler and Samuels,
80 1995, 1998). This prompts the possibility that, in periods of the deep-time past of the Earth
81 when the Drake and/or Tasman gateways were closed or shallow, diapycnal (diabatic) mixing
82 may have played a greater role in setting the mode and intensity of the global overturning
83 circulation (Green and Huber, 2013).

84

85 Since the seminal work of Munk (1966), great efforts have been made to understand what
86 controls diapycnal mixing in the ocean interior (e.g., Munk and Wunsch, 1998; St. Laurent and
87 Garrett, 2002; MacKinnon et al., 2017) and to refine the parameterizations of vertical diffusivity
88 in ocean general circulation models (GCM) (e.g., Bryan and Lewis, 1979; Gargett, 1984;
89 Simmons et al., 2004; Saenko and Merryfield, 2005; Jayne, 2009; Schmittner and Egbert, 2014;
90 Melet et al., 2016; de Lavergne et al., 2020; Song et al., 2023). Recent work has
91 comprehensively reviewed what is currently known about the role of ocean mixing in the
92 climate system (Whalen et al., 2020; de Lavergne et al., 2022; Melet et al., 2022) and, in
93 particular, the contribution of different internal wave processes (e.g., near-field and far-field
94 internal tide dissipation, lee wave dissipation and wind-induced near-inertial wave energy
95 dissipation) to the total mixing. The parameterization of all of these processes into global ocean
96 models is a currently active area of research (MacKinnon et al., 2017) and, in climate models
97 applied to the deep-time past of the Earth, such processes are generally ignored. Instead, mixing
98 in the ocean interior is parameterized either by a constant background diffusivity coefficient or
99 by simple schemes such as a horizontally uniform but depth varying diffusivity (Bryan and
100 Lewis, 1979, hereafter BL).

101

102 In recent years though, some models applied to paleoclimate studies have started to include to
103 contribution of local (near-field) internal tide dissipation (e.g., Schmittner et al., 2015;
104 Hutchinson et al., 2018; Wilmes et al., 2021), following the bottom-intensified mixing
105 parameterization of Simmons et al. (2004, hereafter S04). Wilmes et al. (2021) notably show
106 that using appropriate Last Glacial Maximum tidal dissipation, instead of modern dissipation
107 with otherwise glacial forcings, invigorates the circulation in the ocean interior and increases
108 the fit with carbon isotope measurements. Hutchinson et al. (2018) compare the S04 scheme
109 with the previously-implemented BL scheme in Late Eocene GFDL CM2.1 earth system model
110 simulations and essentially find very little differences in terms of ocean circulation structure
111 and intensity and of water mass age. This is somehow contradictory to the same exercise
112 performed by Jayne (2009) using modern simulations carried out with the NCAR POP 1.4.3
113 ocean model. In the latter work, the change from the BL parameterization to an explicit tidal
114 mixing scheme leads to small impacts on the simulated ocean heat transport (OHT) and upper
115 ocean circulation (because of similar vertical diffusivity values there) but significantly
116 increases the intensity of the deep circulation (Jayne, 2009).

117

118 Another approach has consisted in adding an explicit tidal contribution to the momentum
119 equations rather than to the parameterization of vertical diffusivity (Weber and Thomas, 2017).
120 Though limited to relatively short integration time (100 years in their 3° x 2° Early Eocene
121 ECHAM5/MPIOM configuration) because the explicit tidal forcing requires high resolution
122 simulations (Song et al., 2023), the simulations of Weber and Thomas (2017) report a weak
123 impact of tidal forcing on OHT and large-scale ocean circulation shape but a more significant
124 impact on the intensity of the overturning circulation, echoing the results of Jayne (2009).

125

126 More recently, Zhang et al. (2022) have explored the variability in ocean circulation in models
127 participating to the DeepMIP project on the Early Eocene (Lunt et al., 2017), in which the
128 models were forced by a set of Early Eocene forcings, identical across the models but for the
129 details of their implementation. The authors report large inter-model differences in simulated
130 ocean circulation structure and intensity (Zhang et al., 2022, their Figure 2). Interestingly, the
131 model simulating the most intense overturning circulation (IPSL-CM5A2) is one of the only
132 two DeepMIP models explicitly including a tidal-mixing contribution to vertical diffusivity.

133

134 Here, we investigate the impacts of the inclusion of near-field bottom-intensified tidal mixing
135 (using the S04 parameterization) on the ocean circulation and biogeochemistry in the Early

136 Eocene. We demonstrate that failing to include abyssal turbulent mixing leads to a stagnant
137 ocean with large areas of anoxia, which does not match proxy data from the Equatorial and
138 North Atlantic.

139

140

141 **2. Model and simulations**

142

143 2.1. IPSL-CM5A2 Earth System Model

144

145 The simulations presented in this work are performed with the IPSL-CM5A2 Earth System
146 Model (Sepulchre et al., 2020), itself composed of LMDZ for the atmosphere (Hourdin et al.,
147 2013), ORCHIDEE for the land surface and vegetation (Krinner et al., 2005), and NEMO
148 version 3.6 for the ocean (Madec and the NEMO team, 2016). NEMOv3.6 consists of the OPA
149 dynamic ocean model, the LIM2 sea-ice model (Fichefet and Maqueda, 1997) and the PISCES-
150 v2 marine biogeochemistry model (Aumont et al., 2015). OASIS (Valcke, 2013) is used to
151 couple the models, and XIOS (Meurdesoif et al., 2016) handles input/output processing. LMDZ
152 and ORCHIDEE shares the same horizontal resolution of $3.75^\circ \times 1.875^\circ$ (longitude x latitude)
153 and LMDZ is discretized into 39 uneven levels in the vertical. NEMO has a nominal horizontal
154 resolution of 2° , enhanced to 0.5° at the equator, and 31 vertical levels whose thickness varies
155 from 10 m at the surface to 500 m at the bottom. NEMO uses a tripolar grid to overcome the
156 North Pole singularity (Madec and Imbard, 1996). Previous deep-time paleoclimate modeling
157 with the IPSL-CM5A2 model (e.g., Laugié et al., 2021), including the IPSL-CM5A2
158 simulations carried out as part of the DeepMIP project (Zhang et al., 2020, 2022), used an
159 oceanic domain extending down to 78°S . Here the numerical ocean grid has been regenerated
160 and extended southward in latitude down to 85°S in order to better represent possible marine
161 incursions at latitudes poleward of 78°S in intervals of the last 100 Ma. We note, however, that
162 this represents a negligible issue in the standard DeepMIP paleogeography based on a hotspot
163 reference frame that we use here, though this would not be the case in Early Eocene
164 paleogeographies constructed with a paleomagnetic reference frame (Lunt et al., 2017).

165

166 2.2 Mixing in the ocean model

167

168 In this version of NEMO, vertical mixing in the water column is implemented as a Turbulent
169 Kinetic Energy (TKE) closure model (Gaspar et al., 1990; Blanke and Delecluse, 1993). This

170 closure is complemented with a parameterization for convection, consisting of enhanced
 171 vertical diffusion where stratification is unstable (Lazar et al., 1999), a parameterization for
 172 double diffusive mixing (Merryfield et al., 1999), and a tidal mixing parameterization following
 173 S04. The vertical eddy diffusivity coefficient K_v is thus expressed as:

$$175 \quad K_v = \max(K_0, K_{TKE}) + K_{ddm} + K_{Tides} \text{ for } N^2 > 0 \text{ (stable stratification)}$$

$$176 \quad K_v = K_{EVD} \text{ otherwise}$$

177
 178 with N the Brunt-Väisälä frequency, K_0 a background diffusivity effectively setting the
 179 minimum vertical diffusivity, K_{TKE} the diffusivity computed from the TKE scheme, K_{ddm} the
 180 diffusivity attributed to double diffusion, K_{Tides} the tidal diffusivity and K_{EVD} a prescribed
 181 constant convective diffusivity. Rigorously, the tidal and double diffusion schemes contribute
 182 to K_v even in regions of unstable stratification but the very large diffusivity value
 183 parameterizing convective processes renders these contributions negligible. Here, K_0 is set to
 184 $1.2 \cdot 10^{-5} \text{ m}^2 \text{ s}^{-1}$, $K_{EVD} = 100 \text{ m}^2 \text{ s}^{-1}$ and K_{Tides} has the form:

$$185 \quad K_{Tides} = \frac{q\Gamma EF}{\rho N^2} \quad (\text{Eq. 1})$$

186
 187 where q is the tidal dissipation efficiency, Γ is the mixing efficiency, E is the tidal energy flux
 188 from Green and Huber (2013), ρ is the water density, N is the buoyancy frequency along the
 189 seafloor and F is a vertical structure function that decays exponentially with height above
 190 bottom:
 191

$$192 \quad F(z) = \frac{e^{-\frac{H+z}{h_0}}}{h_0 \left(1 - e^{-\frac{H}{h_0}}\right)} \quad (\text{Eq. 2})$$

193
 194 with H the total depth of the water column and h_0 the vertical decay scale for turbulence.
 195 We use the standard model values of $q = \frac{1}{3}$, $\Gamma = 0.2$ and $h_0 = 500 \text{ m}$ (Madec and the NEMO
 196 team, 2016), which are identical to those originally chosen by S04.
 197

198 2.3 PISCES Marine Biogeochemistry Model

199
 200

201 The PISCES model (Pelagic Interactions Scheme for Carbon and Ecosystem Studies, Aumont
202 et al., 2015) simulates the lower trophic levels of marine ecosystems (nanophytoplankton,
203 diatoms, microzooplankton and mesozooplankton), carbonate chemistry and the
204 biogeochemical cycles of carbon, oxygen, and the main nutrients (phosphorus, nitrogen, iron
205 and silica). Dissolved oxygen is produced in the ocean by phytoplankton net primary production
206 and consumed by zooplankton heterotrophic respiration, oxic remineralization of organic
207 matter and nitrification. At the air-sea interface, dissolved oxygen is exchanged using the
208 parameterization of Wanninkhof (1992). The atmospheric concentration of dioxygen is set to a
209 fixed ratio of 0.21.

210

211 In the water column, PISCES explicitly represents two pools of organic matter particles that
212 differ in their average size (i.e., large and small particles) and respective sinking speed, as well
213 as a pool of semi-labile dissolved organic matter. The particle pools are degraded into the
214 dissolved one as a function of temperature and oxygen concentrations. Dissolved organic matter
215 undergoes oxic remineralization or denitrification depending on local oxygen levels. The
216 remineralization and denitrification rates are function of temperature, oxygen and nitrate
217 concentrations, and of the bacterial activity and biomass (Aumont et al., 2015). When reaching
218 the ocean floor in the form of particles, organic matter is permanently buried or degraded by
219 sedimentary denitrification or oxic remineralization. The proportion of buried carbon is
220 dependent on the organic carbon flux at the bottom and is computed according to Dunne et al.
221 (2007). The fraction of sedimentary denitrification versus oxic remineralization is computed
222 using the meta-model of Middelburg et al. (1996). Degraded organic carbon is then released
223 into the ocean bottom level in the form of DIC. Ocean bottom concentrations of dissolved
224 oxygen and nitrate are also consumed to account for sedimentary oxic remineralization and
225 denitrification, respectively (Aumont et al., 2015). In the absence of an explicit sediment
226 module, the global inventories in phosphate, nitrate, silicate and alkalinity are restored to
227 modern values so that the global mean ocean concentrations in these elements do not drift away
228 from modern mean concentrations (Aumont et al., 2015). We also use an additional inert
229 artificial tracer representing the age of water masses. This age tracer value is restored to 0 in
230 the top 10 m of the model ocean and increases at a rate of one year per year deeper than 10 m
231 (Bopp et al., 2017).

232

233 2.4 Experimental design

234

235 We present two numerical simulations of the Early Eocene based on the DeepMIP protocol
236 (Lunt et al., 2017). The boundary and initial conditions are essentially those of the 840 ppmv
237 simulations of Zhang et al. (2020), that is, we use the paleogeography of Herold et al. (2014)
238 with a prescribed atmospheric CO₂ concentration of 840 ppmv. The orbital parameters of the
239 Earth are those of present-day and other greenhouse gas concentrations are set to their
240 preindustrial values. The simulations are therefore representative of a pre-Paleocene-Eocene
241 Thermal Maximum interval, following the terminology of Lunt et al. (2017). The simulations
242 are initialized with ocean temperature and salinity distributions as in Zhang et al. (2020) and
243 only differ by the absence (“EE-noM2”) or presence (“EE-std”) of the contribution of near-
244 field internal tide energy dissipation (K_{Tides}) to the vertical diffusivity coefficient. In the
245 following, we will refer to the absence or presence of tidal mixing, though this is somewhat a
246 misnomer because the contribution of background diffusivity (i.e. K_0) to vertical diffusivity is
247 included in the two simulations. As described in S04, this background diffusivity may account
248 for the far-field dissipation of large-scale internal tides as well as other sources of mixing that
249 are not explicitly modeled, such as lee waves or wind-induced radiating near-inertial waves
250 (e.g., Melet et al., 2022).

251

252 In NEMOv3.6, the tidal energy flux E includes components for the M2, K1 and S2 tides
253 whereas Green and Huber (2013) provides an estimate only for the M2 tide (see Fig. S1 for a
254 map of the estimated M2 dissipation). Considering that 1) the M2 component dominates the
255 tide, and 2) the S2 energy flux is simply taken to be $\frac{1}{4}$ of the M2 energy flux in the NEMOv3.6
256 mixing scheme, we argue that using $\frac{5}{4}$ of the M2 estimate of Green and Huber (2013) as forcing
257 in the model (M2 + S2 contributions) is a reasonable first step, despite the missing K1
258 contribution.

259

260 The two simulations are run for 5100 model years after which both have reached quasi-
261 equilibrium with small residual trends in mean deep ocean (2750 – 4250 m) temperatures <
262 0.02°C/century (Fig. S2). The last 100 years of each model run are used to build a climatological
263 average for the ocean dynamics. In order to improve the equilibration of biogeochemistry, we
264 extend the simulations in an offline PISCES configuration for another 4000 model years. In this
265 setup, the monthly-mean climatological ocean dynamics is repeatedly read by PISCES to
266 calculate the evolution of the biogeochemical tracer fields. Again, we use the last 100 model
267 years to build a climatological average for the ocean biogeochemistry.

268

269

270 3. Results

271

272 3.1 Energetic considerations

273

274 3.1.1 Available energy

275

276 The tidal model used by Green and Huber (2013) yields an estimate of 1.44 TW of energy
277 dissipated in the Eocene ocean by the M2 barotropic tide, which, interpolated on the NEMO
278 grid, amounts to 1.473 TW. Because the tidal mixing scheme in NEMO includes the S2 tidal
279 contribution expressed as one-fourth of the M2 contribution, the total energy input from tides
280 is 1.841 TW, of which only one-third, 0.614 TW, is assumed to dissipate locally and employed
281 in the tidal mixing scheme (because $q = \frac{1}{3}$ in Equation (1) above).

282

283 The implementation of the tidal mixing scheme in the model is not fully consistent energetically
284 for two reasons. First, a fraction of the energy input is lost in the lower half of the bottom cells,
285 where stratification and diffusivity are not defined because of the no-flux boundary condition
286 at the bottom. Second, the model parameterization imposes an upper bound of $3 \times 10^{-2} \text{ m}^2 \cdot \text{s}^{-1}$ on
287 the tidal diffusivity (Madec and the NEMO team, 2016). Diagnosing the energy effectively
288 used by the tidal mixing scheme gives 0.42 TW, that is, about 70 % of the expected power
289 (0.614 TW).

290

291 We can compute the power consumption due to vertical mixing processes, expressed as in S04:

292

$$293 \quad P = \frac{1}{r} \int \rho K N^2 dV \quad (\text{Eq. 3})$$

294

295 Table 1 shows the amount of power consumed at the global scale and in each basin (Atlantic,
296 Pacific, Indian, Tethys and Arctic, represented on Fig. S3). At the global scale, the total power
297 consumed by diapycnal mixing in the model is 1.45 TW in EE-std. This is weaker than the 1.84
298 TW of total M2 + S2 tidal dissipation estimated by the model of Green and Huber (2013). Two
299 considerations shed light on this difference. First, the effective consumption by tidal vertical
300 mixing is only about 70 % of what is expected from Equation (1). Second, the background

301 diffusivity is simply prescribed and does not depend on the tidal dissipation; hence power
302 consumption by background mixing cannot be expected to match the unused two-thirds of
303 barotropic tidal energy loss.

304 Overall, we calculate that tidal mixing represents about 29 % of the total power consumed by
305 diapycnal mixing in the ocean interior. This ratio is only slightly lower to that simulated by
306 S04, somewhat surprisingly given the very different paleogeography and stratification of our
307 simulations. At the basin scale and excluding the Arctic basin, the contribution from tides
308 varies from 14 % of the total power in the Tethys basin to 32 % in the Pacific basin. This is
309 consistent with larger mean dissipation rates in the Pacific and Indian Oceans than in the
310 Atlantic and Tethys Oceans (Fig. S1).

311

312 3.1.2 Diapycnal diffusivity

313

314 The inclusion of tidal mixing substantially changes the amount of energy available to mix the
315 deep ocean. Diapycnal diffusivities are therefore considerably different both horizontally and
316 vertically in EE-std compared to EE-noM2.

317

318 In EE-noM2, the zonally averaged vertical diffusivity is generally close to the background value
319 except in the surface mixed-layer depth, in which mixing due to the winds generates elevated
320 vertical diffusivity, and in the Southern Ocean where deep convection processes mix waters
321 down to the abyss (Fig. 1a, c, e). At mid depths (2000 – 3000 m), the zonal mean vertical
322 diffusivity is elevated throughout the low latitudes (Fig. 1a). This signal mostly originates from
323 a relatively isolated abyssal sub-basin in the eastern Pacific Ocean between the East Pacific
324 Rise and the American continent (Fig. 1e) in which the weak stratification elevates K_{TKE} and
325 stimulates episodic convective instabilities. At 600 m depth (Fig. 1c), away from turbulent
326 wind-driven mixing, vertical diffusivity is close to the background value K_0 except in deep
327 convection zones of the Southern Ocean. Because the 600 m geopotential surface is also
328 generally far from bottom topography, adding tidal mixing in EE-std does not significantly alter
329 vertical diffusivity at this depth (Fig. 1d), except in deep-water formation zones close to the
330 Antarctic margins. By contrast, diffusivity at 3000 m depth is enhanced by about 2 orders of
331 magnitude in broad regions of the Pacific and Indian Oceans in EE-std relative to EE-noM2
332 (Fig. 1f). Note that because tidal mixing is implemented here as a bottom-intensified energy
333 dissipation, and because stratification generally decreases with depth, the maximum tidal
334 diffusivity in the vertical is found locally on the deepest ocean grid cell. The Atlantic basin in

335 the Eocene configuration exhibits a weaker tide than the Pacific (Green and Huber, 2013, see
336 also Fig. S1) and, therefore, vertical diffusivity does not increase as much as in the Pacific
337 Ocean in EE-std compared to EE-noM2. The zonally averaged vertical diffusivity essentially
338 shows that diapycnal mixing is substantially enhanced in the ocean interior. As we will show
339 in the next sections, the additional mixing energy available in the deep ocean has profound
340 consequences on the intensity of the overturning circulation and the pathways of water masses.

341

342 3.2 Surface changes

343

344 The upper-ocean (0 – 100 m) annual mean temperatures in EE-noM2 are roughly close to 10°C
345 in the Southern Ocean and to 5°C in the quasi-enclosed Arctic Ocean (Fig. 2a). They increase
346 equatorward to reach up to more than 37°C in the equatorial western Pacific. As expected from
347 similar simulations performed with the same model, this temperature distribution is really close
348 to that presented on Figure 2a of Zhang et al. (2020) (see Fig. S4 for a more detailed
349 comparison). Tidally-driven mixing leads to large changes in the Southern Ocean surface layer.
350 The Atlantic and Indian sectors of the Southern Ocean are warmer (locally more than 4K) in
351 EE-std than in EE-noM2 (Fig. 2b), whereas the Pacific sector is cooler, although the change is
352 smaller. Warmer (cooler) regions of the Southern Ocean in EE-std are also regions of increased
353 (decreased) upper ocean salinity (not shown).

354

355 In EE-noM2, deep convective areas are exclusively found in the Southern Ocean, in the
356 Atlantic, Indian and Pacific sectors (Fig. 2c), and there is no deep-water formation in the
357 Northern Hemisphere. The upper-ocean temperature changes in EE-std are sustained by
358 increased deep-water formation in the Atlantic and Indian sector of the Southern Ocean
359 compared to EE-noM2 as can be seen by the deepening of the winter mixed layer depth (MLD)
360 in these areas (Fig. 2d). In the South Atlantic, the MLD deepens by more than 1000 m and
361 enhances the temperature and salt advection feedback from the lower latitudes. In the Pacific
362 sector, the winter MLD instead slightly decreases, driving the opposite change in the advection
363 feedback. Figure S5 further shows that the deepening/shoaling of MLD in EE-std relative to
364 EE-noM2 is robust across the simulations and not simply an artifact of the averaging period.

365

366 3.3 Ocean circulation changes

367

368 The increase in available energy for mixing is reflected by a significant enhancement of the
369 global meridional overturning circulation (MOC) (Fig. 3). The MOC in the two simulations has
370 a roughly comparable shape consisting of a single anticlockwise overturning cell in the
371 Southern Hemisphere fed by deep-water formation in the Southern Ocean. The intensity of the
372 MOC and the penetration of deep-water in the abyss is however greater in EE-std than in EE-
373 noM2, although the maximum rate of overturning is similar in the two simulations (~ 35 Sv at
374 2000 m depth in EE-std and at 900 m depth in EE-noM2). Away from the Southern Ocean, the
375 additional tidal mixing energy sustains a stronger and deeper overturning cell extending up the
376 northern mid to high latitudes (8 Sv at 2000 m depth and 30°N in EE-std, Fig. 3b), effectively
377 increasing the ventilation of the EE-std ocean compared to EE-noM2 and acting to reduce
378 vertical tracer gradients.

379

380 This homogenization is evident from the global zonal mean distribution of temperature (Fig.
381 S6), which shows a globally warmer deep ocean (below ~ 1000 m) and a globally cooler upper
382 and intermediate ocean in EE-std compared to EE-noM2 at all latitudes except those of the
383 Southern Ocean ($80^\circ\text{S} - 40^\circ\text{S}$) where the ocean is globally warmer throughout the water
384 column. The EE-std ocean is thus more vertically well mixed than the EE-noM2 ocean.

385

386 The intensification of the global MOC has interesting consequences on the water mass
387 pathways, in particular in the Atlantic. Figure 4 shows the ocean current velocity and direction
388 at different depths in the South Atlantic and Southern Ocean. At 500 m depth, the western
389 boundary current flowing southward off the coast of South America is substantially increased
390 in EE-std. This increase confines the westward-flowing water masses close to Antarctica to the
391 Southern Ocean, whereas in EE-noM2, these waters mix with those from the South Atlantic
392 western boundary current towards the Indian Ocean. Deeper in the water column (1400 - 1800
393 m depth), the water masses flowing from the Atlantic to the Indian sector of the Southern Ocean
394 in EE-noM2 consist of recirculated waters from the Southern Ocean and locally-formed deep
395 waters, as the southward-flowing Atlantic western boundary current is absent. In contrast, in
396 EE-std, the southward western-boundary current is still active and contributes to exporting
397 water masses from the low-latitude Atlantic toward the Indian Ocean. In the abyss (3250 – 3750
398 m), only a very small fraction of the Southern Ocean water masses flows northward in the
399 Atlantic in EE-noM2 while most are exported eastward to the Indian Ocean. In EE-std an
400 intense northward current advects water masses along the western side of the basin into the
401 Equatorial and North Atlantic.

402

403 These results demonstrate that the deep Equatorial and North Atlantic Oceans are more isolated
404 from the global ocean circulation below ~ 1500 m in EE-noM2 than in EE-std. In the Early
405 Eocene, the deepest connections of the Atlantic basin are with the Southern Ocean because the
406 Central American, Tethys (Gibraltar) and Atlantic-Arctic gateways are all shallow and/or
407 narrow. Since the bathymetric configuration does not change between the two simulations, the
408 increased isolation of the EE-noM2 Equatorial and North Atlantic Oceans is purely caused by
409 lower levels of deep turbulent mixing, leading to major differences in Atlantic stratification and
410 circulation. In EE-std, tidal mixing renders abyssal water masses increasingly more buoyant as
411 they flow away from deep-water formation areas in the Southern Ocean whereas the buoyancy
412 gain across the Atlantic is weaker in EE-noM2. The isopycnal located at approximately 3000
413 m depth at 45°S (the 40.08 and 39.98 $\text{kg}\cdot\text{m}^{-3}$ σ_3 contour in EE-noM2 and EE-std respectively,
414 Fig. 5) indeed deepens to about 3400 m depth in EE-noM2 and 4500 m depth in EE-std at 35°N .
415 In other words, isopycnals of similar depth in the deep South Atlantic exhibit depth difference
416 in excess of 1 km upon reaching the deep North Atlantic. The larger northward deepening of
417 the isopycnals across the deep Atlantic generates a stronger meridional pressure gradient and,
418 thus, forces a more active deep northward circulation (e.g., Whitehead, 1998) in EE-std
419 compared to EE-noM2, leaving the latter more stagnant.

420

421 3.4 Biogeochemical changes

422

423 The more active deep circulation with tidal mixing also yields a significant reorganization of
424 the marine biogeochemistry in the deep ocean, in particular in the Atlantic. At the global scale,
425 though it is once again more evident in the Atlantic (Fig. 5c and d), the deep ocean ventilation
426 is reduced in the absence of tidal mixing. Notably, deep North Atlantic water masses are almost
427 3 times older in EE-noM2 than in EE-std. These deep water masses therefore exhibit very
428 different biogeochemical properties in EE-noM2 and EE-std, and this is particularly visible on
429 the distribution of dissolved oxygen across the water column.

430

431 In EE-noM2, the deep North Atlantic water masses possess the biogeochemical signature of
432 very old water masses: rich in nutrients and dissolved inorganic carbon (DIC) and poor in
433 oxygen. In fact, the North Atlantic is spectacularly oxygen-depleted (Fig. 6a), with hypoxia
434 (defined here as the 62.5 $\text{mmol}\cdot\text{m}^{-3}$ level) reached over the whole water column in the low
435 latitudes of the North Atlantic ($0 - 20^{\circ}\text{N}$) and below 800 m northward of 30°N . Anoxic levels

436 are reached northward of 20°N at depths between 1500 and 3000 m. The North Atlantic seafloor
437 is fully hypoxic and most of the coastal seafloor is anoxic (Fig. 6c). In contrast, deep North
438 Atlantic DIC and phosphate concentrations are high (Figs. S7 and S8) because falling organic
439 matter has been remineralized along the water mass journey and nutrients have therefore
440 accumulated in the deep ocean. Nitrate concentrations, however, rather decrease northward in
441 the deep Atlantic (Fig. S9) because the depletion in oxygen in this ocean basin triggers
442 denitrification to continue the remineralization process.

443

444 In EE-std, the younger water masses in the deep North Atlantic are relatively rich in oxygen
445 (Fig. 6b) and the seafloor is well oxygenated with only very limited hypoxic coastal areas. The
446 North Atlantic exhibits higher nitrate concentrations in EE-std than EE-noM2 in the deep (Fig.
447 S9), because the oxygen levels are above those required to trigger denitrification, and we find
448 lower DIC and phosphate concentrations (Figs. S7 and S8), as expected for better ventilated
449 water masses.

450

451 There are three main processes controlling the oxygenation of water masses in the ocean:
452 surface atmosphere-ocean interaction controlling the degree of solubility of O₂ in the ocean,
453 ocean circulation, and biological activity. Dissolved O₂ concentrations in the ocean can be
454 decomposed into a thermal and a non-thermal component, referred to as the saturation
455 component (O_{2sat}) and the Apparent Oxygen Utilization (AOU) respectively. O_{2sat} is the
456 concentration of O₂ that can be dissolved for a given temperature and salinity whereas AOU
457 integrates the contribution of ocean circulation and biology. These quantities are related as
458 such:

459

$$O_2 = O_{2sat} - AOU$$

460

461 As shown on Figure 7 for EE-noM2, surface O_{2sat} increases poleward because solubility
462 increases with decreasing temperatures (Fig. 7b). Surface O₂ concentrations are generally close
463 to O_{2sat} because, besides interacting with the atmosphere, the upper ocean layers gain dissolved
464 O₂ as the result of photosynthesis of marine phytoplankton. The AOU is therefore low (e.g., the
465 surface mid-latitudes on Fig. 7c). One notable exception is the equatorial subsurface ocean
466 because it is a region of upwelling that brings to the upper ocean water masses extremely rich
467 in nutrients allowing for intense phytoplanktonic activity. Consequently, large amounts of
468 organic matter sink and consume oxygen at a rate faster than the one at which the ocean restores
469 its O₂ concentration by atmospheric exchange.

470

471 In the intermediate and deep ocean, O_2 concentrations are close to O_{2sat} in the Southern Ocean
472 where deep convection occurs (Fig. 7a and b). As water masses age in the ocean interior (Fig.
473 7d), O_2 concentrations depart from O_{2sat} because of the increasing influence of remineralization
474 processes that consume oxygen in the water column (reflected by the increasing AOU, Fig. 7c).
475 In the deep North Atlantic, extremely old water masses that have not been in contact with the
476 atmosphere for more than a millennium exhibit AOU values almost equal to O_{2sat} , indicating
477 that almost all the available O_2 has been consumed.

478

479 Any change in dissolved O_2 concentrations between EE-noM2 and EE-std can therefore be
480 partitioned into the change in O_{2sat} , reflecting the change in temperature and, to a lesser extent,
481 salinity between EE-std and EE-noM2 and the change in AOU, which reflects circulation and
482 biological changes:

483

$$\Delta O_2 = \Delta O_{2sat} - \Delta AOU$$

484

485 In the Atlantic, the changes in dissolved O_2 concentrations are almost fully explained by
486 changes in AOU (Fig. 8). Interestingly, Figure 8 shows that contours of ΔAOU and of the water
487 age difference between EE-std and EE-noM2 are very well correlated, thereby strongly hinting
488 that the primary driver of oxygen changes is the reorganization of the ocean circulation
489 following the addition of tidally-driven mixing. This is also confirmed by the limited changes
490 in export productivity to the intermediate and deep ocean (Fig. S10).

491

492

493 **4. Discussion**

494

495 Our simulations compellingly demonstrate the crucial role played by tidally-driven abyssal
496 turbulent mixing in shaping the circulation and the distribution of biogeochemical tracers in the
497 ocean interior. However, apart from a few sensitivity simulations (Thomas et al., 2014; Weber
498 and Thomas, 2017; Hutchinson et al., 2018), most earth system models applied to deep-time
499 climates generally neglect tidally-driven mixing as a specific forcing and alter (or not) spatially-
500 constant coefficients in the implemented vertical mixing parameterization (e.g., Bryan and
501 Lewis, 1979) as a workaround (e.g., Zhang et al., 2022).

502

503 Hutchinson et al. (2018) find weak differences in terms of MOC shape and intensity and water
504 mass age between the standard BL scheme used in their CM2.1 Late Eocene simulations and
505 the same S04 bottom intensified mixing scheme as used here, indicating that the simulated
506 ocean circulation is largely similar. This is somewhat contradictory to the large change in MOC
507 intensity (and water age) found in our simulations, and we suggest a couple of explanatory
508 avenues. First, the standard BL scheme in Hutchinson et al. (2018) makes diffusivity increase
509 with depth—although without spatial dependence—and, as such, it is not rigorously similar to
510 prescribing a uniform background diffusivity coefficient K_0 . We note however that, comparing
511 the BL and S04 schemes in a modern configuration, Jayne (2009) observes a large enhancement
512 of the intensity of the deep cell of the MOC in S04 with little change in MOC structure, much
513 as we observe in our simulations. Second, though Hutchinson et al. (2018) apply the same S04
514 scheme as we do, their input dissipation rate E is recomputed directly using equation (2) of S04
515 and a uniform seafloor roughness amplitude whereas we prescribe E based on the explicit tidal
516 model of Green and Huber (2013). This results in quite different mean vertical diffusivities at
517 a basin-scale. In particular, their mean Atlantic diffusivity, when using the tidal scheme, is
518 much enhanced compared to their mean Pacific diffusivity, whereas we find the opposite ratio
519 in our simulations (Fig. S11 and Fig. 9 of Hutchinson et al., 2018). Our results are in agreement
520 with the enhanced Pacific dissipation found in the tidal model results of Green and Huber
521 (2013). Because the specifics of the calculation of the dissipation rate E are missing in
522 Hutchinson et al. (2018), it still remains unclear at this stage whether these differences stem
523 from (i) the spatial variability of the tidal forcing (which may be absent in Hutchinson et al.,
524 2018), (ii) a different model implementation of the S04 tidal dissipation scheme, (iii) the change
525 in tidal forcing across the 15 Myrs separating the Early and Late Eocene, or (iv) different levels
526 of spurious numerical mixing in GFDL-CM2.1 and IPSL-CM5A2 (e.g., Holmes et al., 2021).
527 This nonetheless suggests that the spatial distribution of the tidal forcing significantly alters the
528 simulated ocean circulation (Saenko, 2006; Jayne, 2009).

529

530 Using CCSM3-forced MITgcm simulations of the Early Eocene, which includes a Bryan-Lewis
531 diffusivity profile and an older reconstruction of the paleogeography, Thomas et al. (2014)
532 found that increasing the diffusivity beyond the standard BL coefficients allow for a large
533 increase in the intensity of the MOC and yield a circulation mode that compares better to
534 compiled Pacific ϵ_{Nd} data, in particular in the case in which abyssal mixing is increased. In an
535 additional sensitivity experiment, the authors increased the mixing approximately fivefold
536 throughout the water column; doing this significantly enhanced the poleward OHT and reduced

537 the meridional surface temperature gradients, in agreement with inferred proxy data as well as
538 previous investigations of increased upper ocean mixing effect on OHT (e.g., Jayne, 2009). In
539 our simulations, the meridional SST gradient is only weakly affected by the addition of tidal
540 mixing because vertical diffusivity in the upper 1000 m is similar in EE-noM2 and EE-std (Fig.
541 S11). Below 1000 m, diffusivity (and meridional transport) increases substantially in EE-std
542 but the vertical temperature gradient does not (Fig. S6) and the change in heat transport is small.
543 Thomas et al. (2014) however note that sustaining such elevated diffusivity across the water
544 column would require more than 20 TW; an amount of energy that tides cannot account for
545 (Green and Huber, 2013) and whose source has yet to be found.

546

547 Using the ECHAM5/MPIOM model with the Early Eocene paleogeography of Heinemann et
548 al. (2009), Weber and Thomas (2017) also investigated the response of the Eocene ocean
549 circulation to tides. They simulate the change in ocean circulation in a similar setup than the
550 one presented here, although the inclusion of tides in their model is represented by an additional,
551 explicit, tidal forcing on the momentum equations rather than the parameterization of the
552 contribution of tides to vertical diffusivity (Song et al., 2023). The simulated ocean circulation
553 of Weber and Thomas (2017) exhibits deep-water formation in the Southern Atlantic, as here,
554 but also in the North Atlantic. As in our experiments, adding tidal influence does not
555 substantially modify the location of deep-water formation regions, in contrast to the penetration
556 depth of these deep waters, but the limited integration time of their tidal simulation (100 years)
557 prompts the possibility that it might not have reached sufficient equilibrium. One possible
558 reason, among others (see, e.g., Zhang et al., 2022), explaining the different regions of deep
559 convective activity is the paleogeographic reconstruction, which, in Weber and Thomas (2017),
560 possesses in particular closed Drake Passage and Tasman Gateway and a more widely opened
561 Central American Seaway compared to the Herold et al. (2014) reconstruction that we use. We
562 indeed note that the recent DeepMIP study of Zhang et al. (2022) on Early Eocene ocean
563 circulation highlights that all of the models—with the Herold et al. (2014) paleogeography—
564 produce deep-water formation in the Southern Ocean (regardless of the sector) at the exception
565 of the GFDL model, which exhibits deep convective activity in the North Pacific, and the
566 NorESM model, which does not exhibit any deep-water formation, possibly because of
567 insufficient spinup. In contrast, the models do not produce deep-water formation in the North
568 Atlantic. Though the details of the ocean circulation differ between our simulations and those
569 of Weber and Thomas (2017), the addition of tidal mixing has similar effects on the simulated
570 circulation. Weber and Thomas (2017) also report an increase in the intensity of the MOC but

571 hardly any increase in ocean heat transport, in keeping with the notion that the impacts of the
572 Eocene tide are concentrated in the abyssal ocean (Green and Huber, 2013).

573

574 In a recent comparison of the S04 tidal mixing scheme vs. explicit tidal forcing, both approaches
575 were implemented in the FESOM2 ocean model (Song et al., 2023). The authors conclude that
576 while the parameterized tidal mixing may miss some potentially important effects, such as the
577 enhancement of bottom drag and continental shelf viscous dissipation, the explicit tidal forcing
578 typically requires resolution of the order of 0.1° to produce realistic impacts. As a result, lower
579 resolution simulations compare less favorably to observed hydrography with this scheme than
580 with the S04 parameterization. It also makes the inclusion of explicit tidal forcing currently
581 inapplicable to long-term deep-time climate simulations (Song et al., 2023).

582

583 Other studies have attempted to simulate the biogeochemical state of the Early Eocene (e.g.,
584 Heinze and Ilyina, 2015), generally in order to focus on the PETM perturbation (Winguth et
585 al., 2012; Meissner et al., 2014; Ilyina and Heinze, 2019). In particular, Winguth et al. (2012)
586 and Heinze and Ilyina (2015) have used modelling setups consisting of biogeochemical models
587 of resolution and complexity similar to PISCES and forced by or coupled to ocean-atmosphere
588 general circulation models, but the prescribed paleogeography and atmospheric CO_2 bear no
589 consistency between the studies unlike more recent coordinated efforts such as DeepMIP (Lunt
590 et al., 2017, 2021). Deep O_2 concentrations exhibit large differences between the simulations:
591 the 1120 ppmv CO_2 simulation of Winguth et al. (2012) generates a well oxygenated Pacific
592 Ocean and a more poorly oxygenated Atlantic Ocean whereas the 560 ppmv CO_2 simulation of
593 Heinze and Ilyina (2015) shows a better oxygenated Atlantic than Pacific Ocean. In our
594 simulations with tidal mixing at 840 ppmv, the deep Atlantic is better oxygenated than the
595 Pacific (Fig. S12) but the equatorial Atlantic oxygen minimum zone is more developed and has
596 lower O_2 concentrations. Interestingly, the primary production patterns in the upper ocean are
597 more similar, with for instance intense primary production in most of the equatorial Pacific, in
598 the eastern side of the Pacific and Atlantic Oceans as well as in the Southern Ocean. This
599 suggests that the diversity in O_2 distributions across the simulations largely reflects the
600 simulated ocean circulation, at least in the deep ocean.

601

602 There is currently no quantitative proxy for O_2 concentrations in the past, although semi-
603 quantitative multi-proxy approaches can provide estimates of poorly oxygenated bottom water
604 conditions ($\leq 50 \mu\text{mol/kg}$) (Lu et al., 2020). Most studies therefore report qualitative estimates

605 of the local oxygenation state of the ocean relative to a baseline value, using redox-sensitive
606 proxies such as the I/Ca ratio (e.g., Zhou et al., 2014, 2016), trace elements like molybdenum
607 or manganese (Dickson et al., 2012, 2014; Pälike et al., 2014) or magnetofossils (Xue et al.,
608 2022, 2023). Anoxic bottom water masses are perhaps more easily identifiable because the
609 sedimentary abundance of trace elements is strongly redox dependent and sedimentary
610 enrichment above average crustal values via complexification with sulfide elements is
611 interpreted as reflecting high dissolved sulfide concentrations and thus anoxic/euxinic
612 conditions (Dickson et al., 2012, 2014). If the distribution of Early Eocene redox archives is
613 relatively global (though concentrated in the peri-Tethys area, see Figure 6 of Carmichael et
614 al., 2017), the information conveyed by these estimates remains potentially strongly influenced
615 by local settings (Clarkson et al., 2021). A complementary approach therefore consists in
616 estimating the global area or volume occupied by anoxic or euxinic waters, using the isotopic
617 ratio of molybdenum (Dickson et al., 2012), sulfur (Yao et al., 2018) or uranium (Clarkson et
618 al., 2021), rather than reporting local estimates of bottom water oxygenation. For instance,
619 combining uranium isotope measurements from ODP Site 865 (Allison Guyot, equatorial
620 Pacific Ocean), DSDP Site 401 (Bay of Biscay, northeast Atlantic Ocean) and ODP Site 690
621 (Maud Rise, Atlantic sector of Southern Ocean) with box modelling, Clarkson et al. (2021)
622 propose a maximal extent of seafloor anoxia of 0.25 % prior to the PETM perturbation and 2
623 % at the PETM.

624

625 In the following, we compare the simulated oxygen concentrations in EE-noM2 and EE-std
626 with available data across a transect in the Atlantic using reported oxygen conditions at each
627 site (Fig. 9) and compute the extent of anoxic seafloor simulated by the model. Three main
628 observations can be made. First, the qualitative nature of the proxy leaves room for various
629 interpretations. At the exception of Site 1262 and 1266 at Walvis Ridge for whose oxygen-rich
630 conditions have been reported by the different proxies (Pälike et al., 2014; Xue et al., 2022),
631 low oxygen content is estimated at every site but the degree of oxygen deficiency is unclear
632 because anywhere between the anoxic ($0 \mu\text{mol/L}$) and hypoxic threshold ($\sim 60 - 70 \mu\text{mol/L}$,
633 Lu et al., 2020; Laugié et al., 2021). Second, at face value, the simulated O_2 concentrations are
634 probably too low in EE-noM2, in particular in the North Atlantic, and too high in EE-std. Third,
635 the fact that reported qualitative oxygen conditions in the data on Figure 9 reflect pre-PETM
636 conditions and that most of these proxies suggest decreasing oxygen concentrations across the
637 PETM perturbation but without extensive anoxia leads to the conservative assumption that the
638 pre-PETM ocean did not exhibit large-scale conditions too close to anoxia. In this regard, the

639 simulated oxygen concentrations suggest that the ocean biogeochemical state in EE-noM2 is
640 probably aberrant. This is confirmed by our calculation of the extent of anoxic seafloor,
641 respectively 2.3 % in EE-noM2 and 0.1 % in EE-std, which also suggests an excess in oxygen
642 depletion in EE-noM2 compared to pre-PETM estimates (Clarkson et al., 2021).

643

644 In addition, here, we do not *stricto sensu* model the biogeochemical conditions of the pre-PETM
645 as, for instance, the global mean nutrient concentrations in phosphate, nitrate, alkalinity and
646 silicate in the ocean are identical to the modern. Recent statistical box-modelling instead
647 suggests that the marine phosphate concentrations reached a peak in the Paleogene, thus
648 promoting higher primary productivity and lower deep-ocean O₂ concentrations (Sharoni and
649 Halevy, 2023). All else being equal, prescribing a higher marine nutrient content in our
650 simulations would decrease oxygen concentrations in both EE-noM2 and EE-std but with
651 opposite effect on the model-data comparison. In EE-std, this would reduce the model-data
652 mismatch because simulated O₂ concentrations are likely too high whereas in EE-noM2, it
653 would increase the proportion of anoxic waters and thereby increase the mismatch with
654 estimates from the geological record. The model-data mismatch in EE-std could be even further
655 reduced with a better representation of the smaller meridional temperature gradients that are
656 inferred from proxy data (e.g., Huber and Caballero, 2011; Evans et al., 2018) because this
657 would act to reduce the amount of oxygen stored in surface waters, and therefore decrease O₂
658 concentrations throughout the water column. This also implies that the simulated O₂
659 concentrations in EE-noM2 are likely a conservatively “high-concentration” estimate and thus
660 that the aberrant biogeochemical state likely reflects an aberrant Early Eocene dynamical ocean
661 in EE-noM2.

662

663 Finally, we note that the input energy dissipation from the M2 tide that was used here is not
664 exactly appropriate because the tidal model of Green and Huber (2013) was run with the ocean
665 stratification obtained from the low-resolution equilibrated CCSM3 simulations discussed in
666 Liu et al. (2009) instead of having been run with the IPSL-CM5A2 stratification. However,
667 these simulations use a bathymetry close to that used in Green and Huber (2013) and the abyssal
668 tidal dissipation is relatively insensitive to moderate changes in stratification. In addition, both
669 our simulations and those of Liu et al. (2009) exhibit deep-water formation in the Southern
670 Ocean. We thus argue that our results would not be significantly affected if the stratification
671 from our simulations had been used in the tidal model simulations. In contrast, a larger impact
672 is likely to be expected by the use of a higher-resolution bathymetric dataset in an improved

673 version of the tidal inversion model of Green and Huber (2013), such as that proposed in Green
674 et al. (2023), and we ambition to investigate this possibility in a near future. Alternatively, a
675 promising way lies in the use of comprehensive tidal mixing schemes accounting for both near-
676 field and far-field dissipation of internal tides (de Lavergne et al., 2020), rather than schemes
677 fixing vertical diffusivity, such as the BL scheme, or including only near-field mixing, such as
678 the S04 scheme used here.

679

680

681 **Conclusion**

682

683 Using Early Eocene IPSL-CM5A2 earth system model simulations, we demonstrate the
684 critically-overlooked impact of including a realistic estimate of the abyssal mixing driven by
685 the near-field dissipation of internal tides in deep-time paleoclimate simulations. In our
686 simulations, the global deep ocean circulation is substantially altered by the inclusion of abyssal
687 tidal mixing, in particular in the Atlantic basin, and the global meridional overturning
688 circulation is more intense and penetrates deeper in the ocean interior. This consequently drives
689 large changes in the biogeochemical properties of deep water masses. In particular, we show
690 that failing to include this abyssal turbulent mixing leads to a stagnant deep North Atlantic
691 ocean with large anoxic areas that compares less favorably to qualitative reconstruction of
692 paleo-oxygenation for this period than the more vigorous deep Atlantic ocean simulated in the
693 experiment with realistic tidal mixing. Our results therefore stress the importance of routinely
694 including abyssal turbulent mixing in upcoming deep-time paleoclimate studies and underline
695 how the use of an adjunct biogeochemical model can help disentangle dynamical ocean modes
696 for which proxies are lacking.

697

698

699 **Acknowledgment**

700 This work used computing hours on the HPC resources of the TGCC under GENCI allocations
701 A0110102212 and A0130102212. We are grateful to Olivier Marti, Laurent Bopp, Olivier
702 Aumont and Christian Ethé for discussions and help with the simulation setup. NCL
703 (<https://www.ncl.ucar.edu>) was used to make figures and most analyses, in addition to Fortran.
704 Figures use color maps developed by Fabio Cramer (Cramer et al., 2020). JAMG
705 acknowledges funding from the UK Natural Environment Research Council (grants
706 NE/F014821/1 and NE/S009566/1). YD acknowledges funding from the National Agency for

707 Research (ANR) project OXYMORE (grant 18-CE31-0020). The authors declare no conflict
708 of interest.

709
710

711 **Data availability**

712 Code availability. LMDZ, NEMO (including PISCES), ORCHIDEE and XIOS are released
713 under the terms of the CeCILL license. OASIS-MCT is released under the terms of the Lesser
714 GNU General Public License (LGPL). IPSL-CM5A2 source code is available via modipsl with
715 the command lines:

```
716 svn co -r 6039 https://forge.ipsl.jussieu.fr/igcmg/svn/modipsl/trunk modipsl;  
717 cd modipsl/util; ./model IPSLCM5A2.2
```

718 The model revision numbers used in this work can be found in the modipsl/util/mod.def file:

- 719 - NEMOGCM branch nemo_v3_6_STABLE revision 6665
- 720 - XIOS2 branches/xios-2.5 revision 1903
- 721 - IOIPSL/src svn tags/v2_2_2
- 722 - LMDZ5 branches/IPSLCM5A2.1 rev 3907
- 723 - ORCHIDEE branches/ORCHIDEE-IPSLCM5A2.1 rev 7376
- 724 - OASIS3-MCT 2.0_branch (rev 4775 IPSL server)

725 We recommend to refer to the project website for a proper installation and compilation of the
726 environment:

727 https://forge.ipsl.jussieu.fr/igcmg_doc/wiki/Doc/Config/IPSLCM5A2, last access: 21/11/2023.

728

729 Model outputs. NetCDF outputs and scripts to produce the figures used in this study are stored
730 at <https://doi.org/10.5281/zenodo.10246071>.

731
732
733
734
735
736
737
738
739
740

741 **Tables and figures**

742

		Power consumption used for diapycnal mixing (TW)			Fraction of power consumption due to tides
		K ₀	Tides	Total	
Global	EE-std	1.03	0.422	1.45	0.29
	EE-noM2	1.02	0	1.02	0
Pacific	EE-std	0.590	0.282	0.872	0.32
	EE-noM2	0.584	0	0.584	0
Atlantic	EE-std	0.162	0.0560	0.218	0.26
	EE-noM2	0.160	0	0.160	0
Indian	EE-std	0.145	0.0661	0.211	0.31
	EE-noM2	0.140	0	0.140	0
Tethys	EE-std	0.109	0.0175	0.127	0.14
	EE-noM2	0.108	0	0.108	0
Arctic	EE-std	0.0278	5 10 ⁻⁴	0.0283	0.02
	EE-noM2	0.0255	0	0.0255	0

Table 1. Power consumed by diapycnal mixing and fraction of power consumption due to tides calculated at the global-scale and for individual basins shown on Figure S3.

743

744

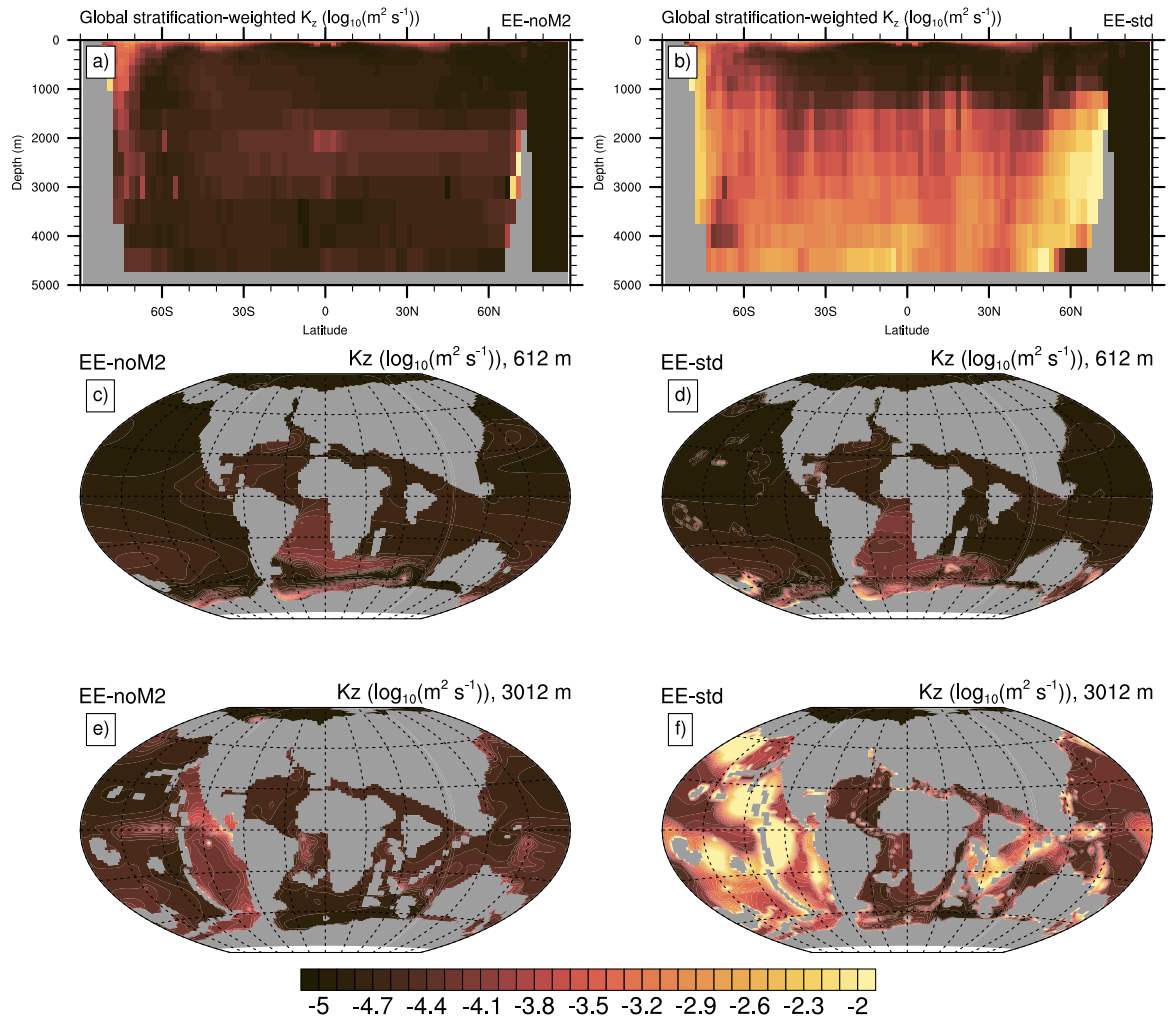


Figure 1. Stratification-weighted global zonal average of vertical diffusivity for EE-noM2 (a) and EE-std (b) ($\log_{10}(\text{m}^2 \text{s}^{-1})$). Diffusivity at 600 m and 3000 m for EE-noM2 (c, e) and EE-std (d, f) ($\log_{10}(\text{m}^2 \text{s}^{-1})$).

745

746

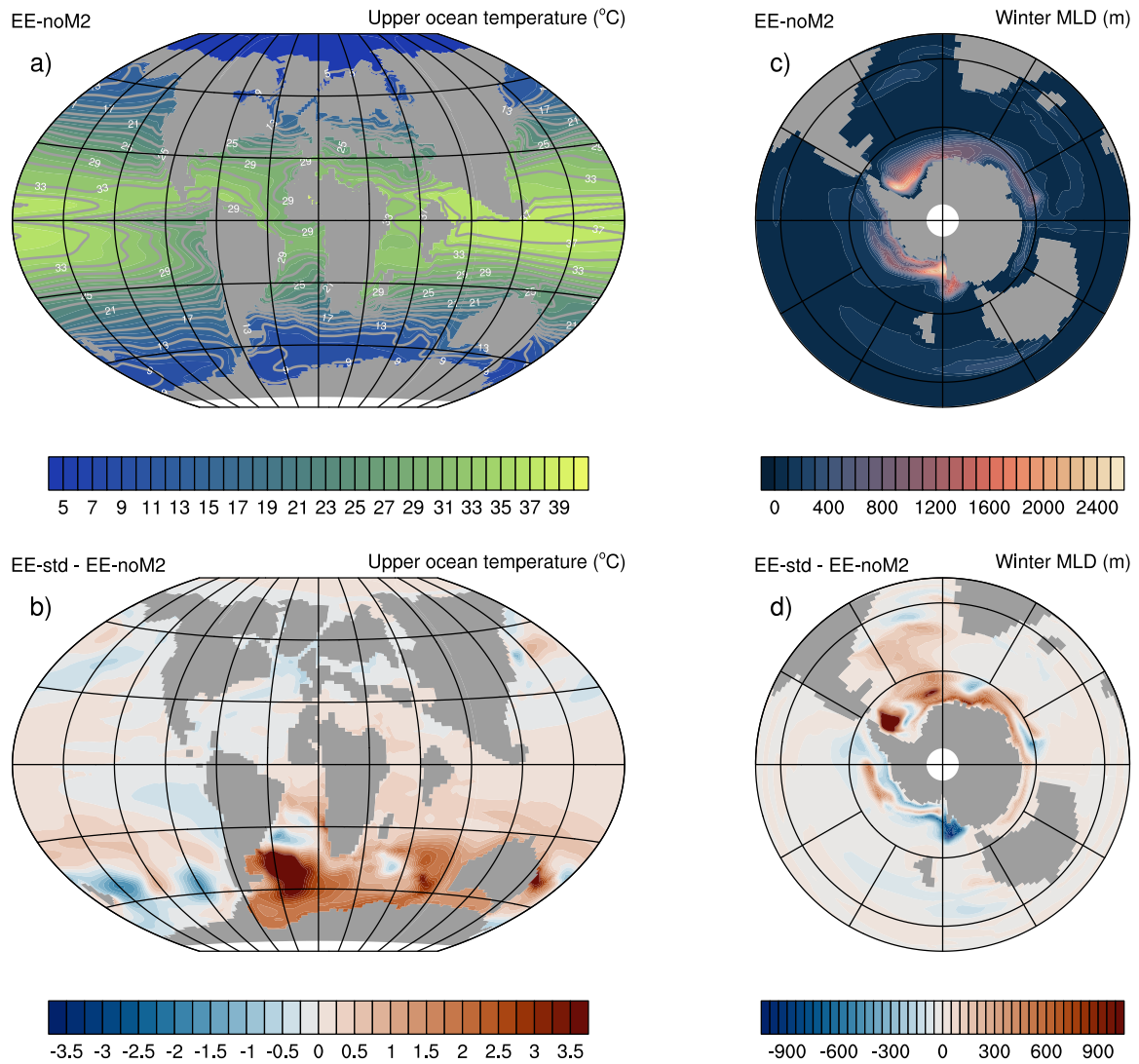


Figure 2. (a) EE-std mean annual upper ocean (0-100 m) temperatures ($^{\circ}\text{C}$). (b) Mean annual upper ocean temperature (0-100 m) difference ($^{\circ}\text{C}$) between EE-noM2 and EE-std. (c) Mean winter MLD (m) in EE-noM2. (d) Mean winter MLD difference (m) between EE-std and EE-noM2.

747

748

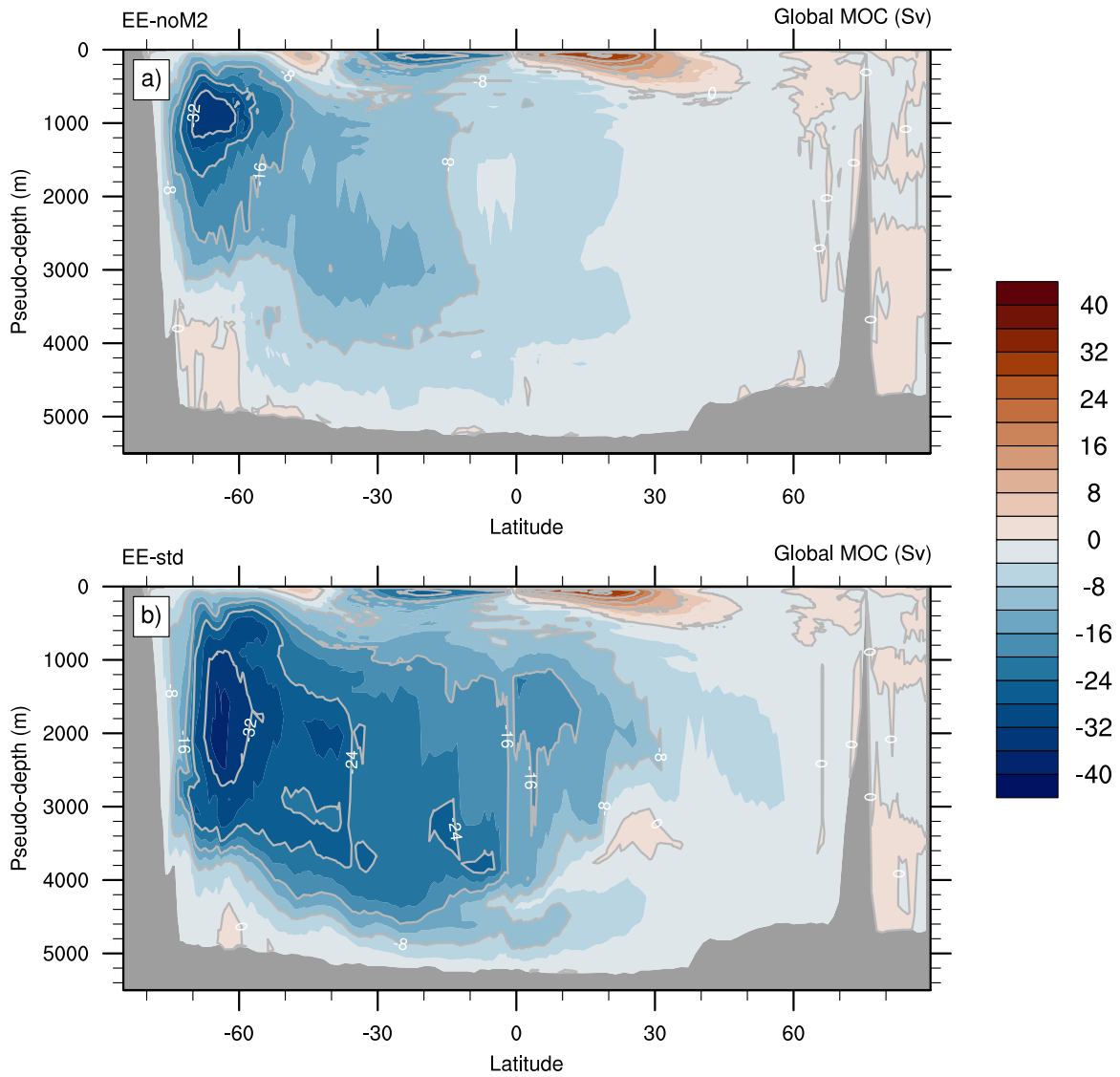


Figure 3. Global meridional overturning streamfunction (Sv) in EE-std (a) and EE-noM2 (b). Note that the MOC has been computed in density coordinates and reprojected to a pseudo-depth, following de Lavergne et al. (2017).

749

750

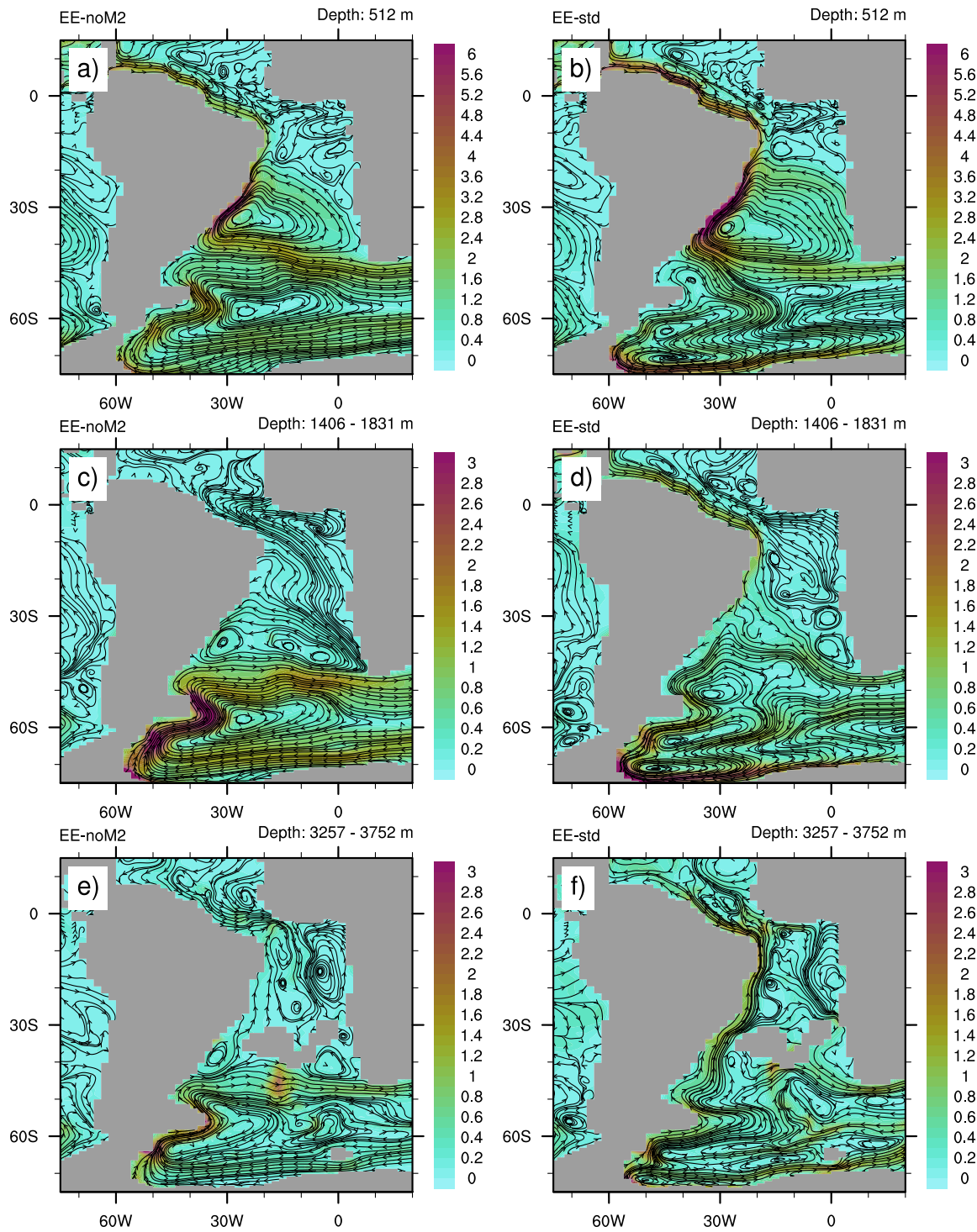


Figure 4. Ocean velocity (cm s^{-1}) at 500 m depth (a,b), averaged between 1400 and 1800 m (c, d) and averaged between 3250 and 3750 m (e, f) in EE-noM2 (a, c, e) and EE-std (b, d, f).

751

752

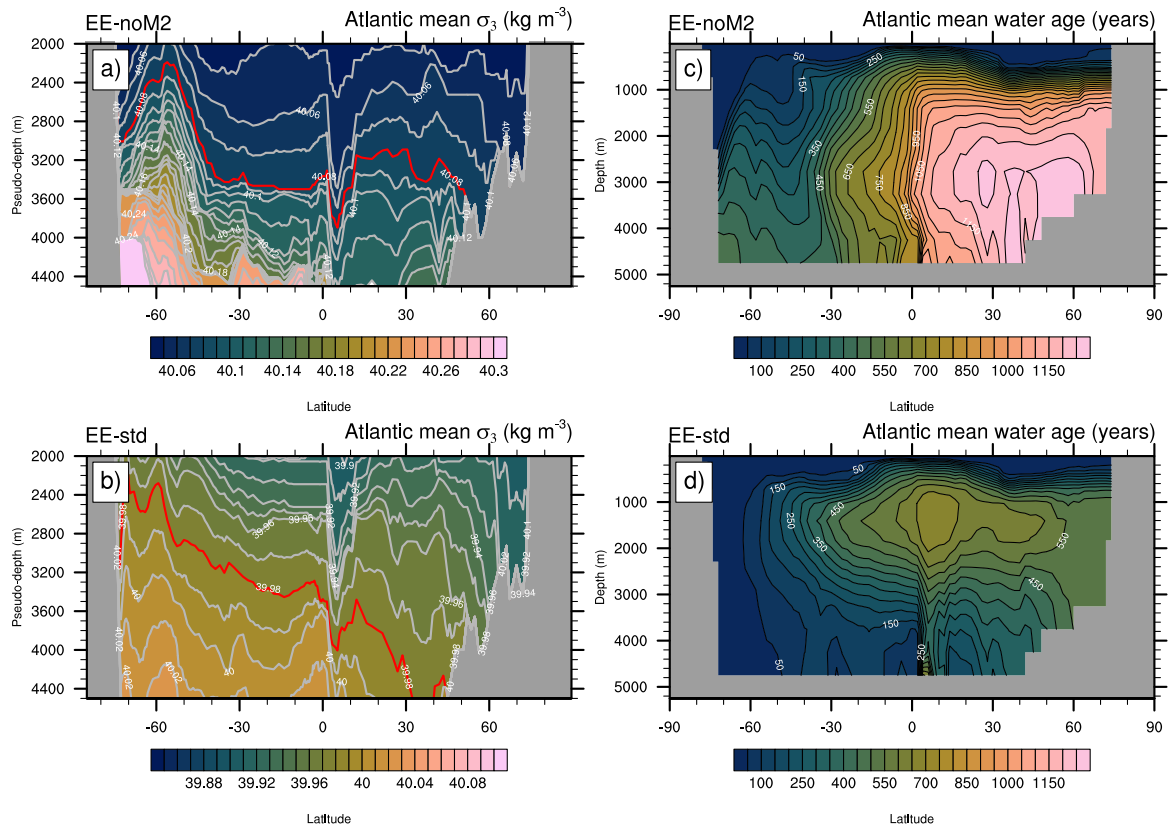


Figure 5. Zonally-averaged s_3 isopycnal profiles (kg m^{-3}) across the deep Atlantic in EE-noM2 (a) and EE-std (b) computed in density coordinates and reprojected to a pseudo-depth. The 40.06 and 39.98 kg m^{-3} s_3 contours are highlighted in red in (a) and (b) respectively, for easier visualization. Zonally averaged water age profile across the Atlantic in EE-noM2 (c) and EE-std (d). Note the different vertical axes between the two columns.

753

754

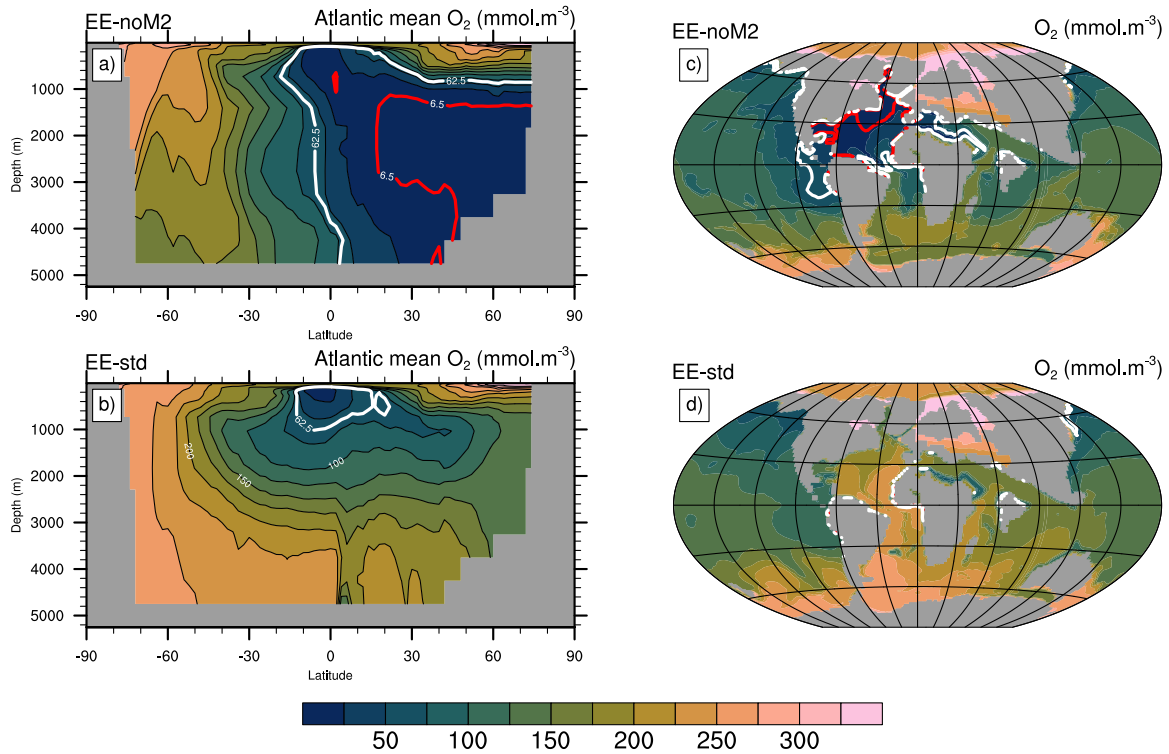


Figure 6. Zonally-averaged dissolved oxygen concentrations (mmol m^{-3}) across the Atlantic in EE-noM2 (a) and EE-std (b). Dissolved oxygen concentrations (mmol m^{-3}) at the seafloor in EE-noM2 (c) and EE-std (d). The hypoxic (62.5 mmol m^{-3}) and anoxic (6.5 mmol m^{-3}) thresholds (Laugié et al., 2021) are contoured in white and red, respectively.

755

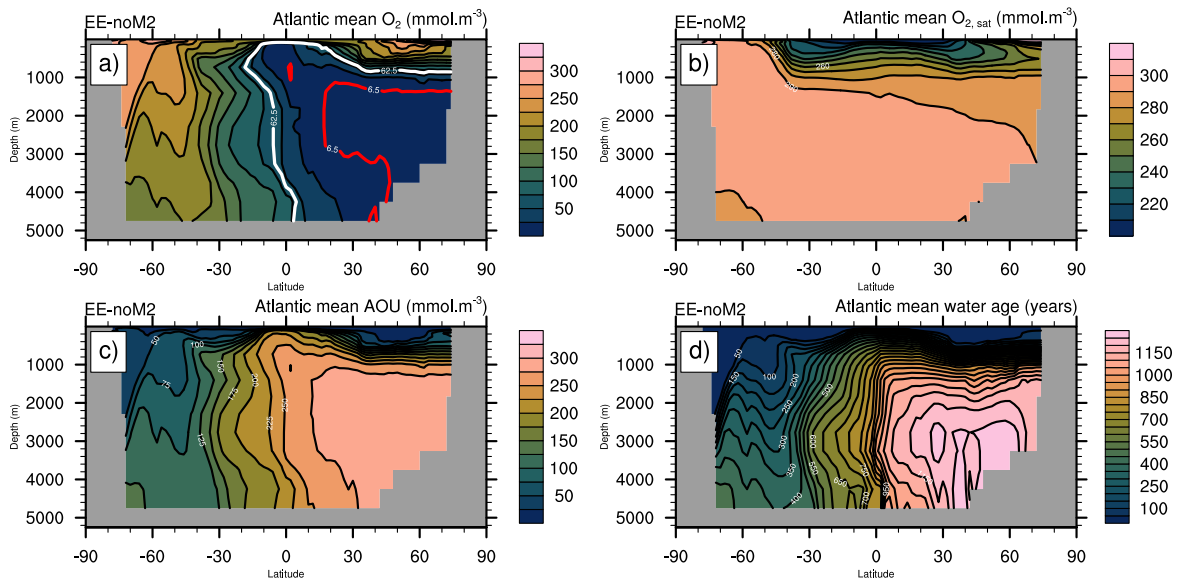


Figure 7. Zonally averaged (a) dissolved oxygen concentrations (mmol m^{-3}), (b) $\text{O}_{2\text{sat}}$ (mmol m^{-3}), (c) AOU (mmol m^{-3}) and (d) water age (years) across the Atlantic in EE-noM2. Note the different scale in panel (b) relative to (a) and (c).

756

757

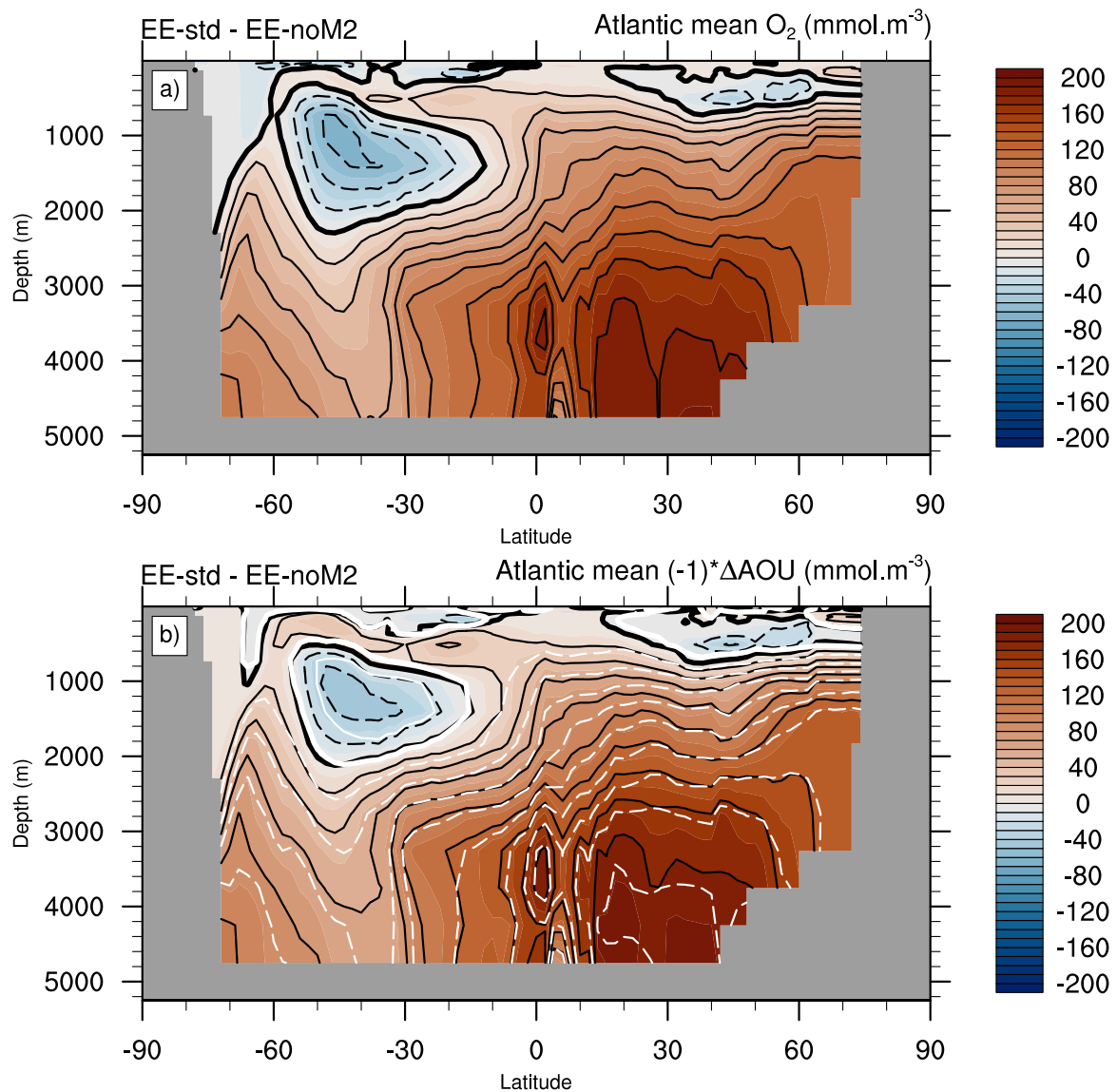


Figure 8. Zonally averaged (a) dissolved oxygen concentration difference (mmol m^{-3}) and (b) AOU difference (mmol m^{-3}) across the Atlantic between EE-std and EE-noM2 (shading and black contours). White contours denote the difference in water age between EE-std and EE-noM2 (positive solid and negative dashed).

758

759

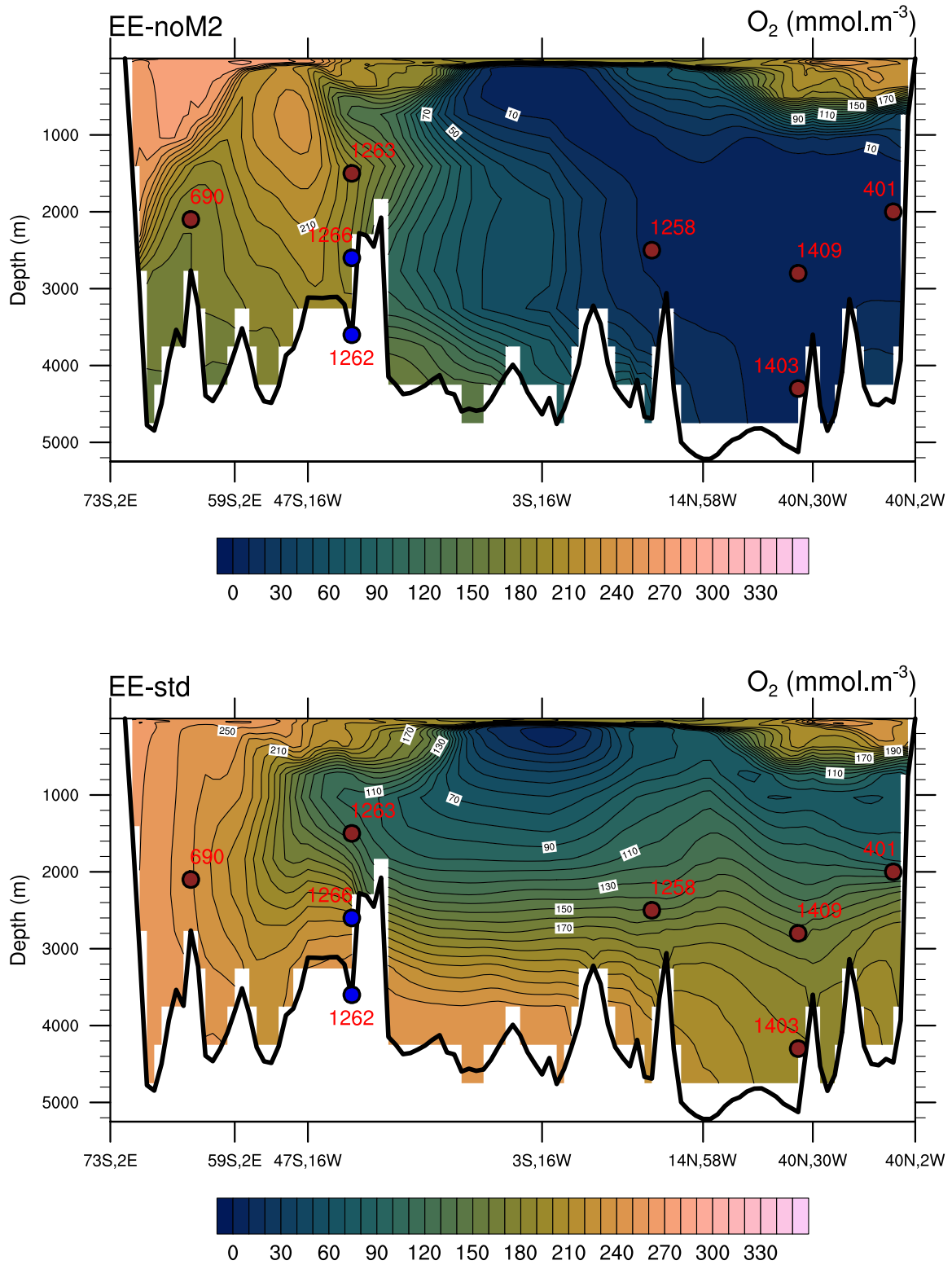


Figure 9. Dissolved oxygen concentration (mmol m^{-3}) transect across the Atlantic for EE-noM2 (a) and EE-std (b). The transect followed is shown on Fig. S3. At the exception of Sites 1262 and 1266 (blue color), for which oxygen-rich conditions have been reported, other Atlantic sites (brownish color) exhibit low oxygen conditions, according to proxy data.

761

762

763 **References**

764

- 765 Aumont, O., Ethé, C., Tagliabue, A., Bopp, L., Gehlen, M., 2015. PISCES-v2: an ocean
766 biogeochemical model for carbon and ecosystem studies. *Geosci. Model Dev.* 8, 2465–2513.
767 <https://doi.org/10.5194/gmd-8-2465-2015>
- 768 Blanke, B., Delecluse, P., 1993. Variability of the tropical Atlantic Ocean simulated by a
769 general circulation model with two different mixed-layer physics. *J. Phys. Oceanogr.* 23,
770 1363–1388. [https://doi.org/10.1175/1520-0485\(1993\)023<1363:VOTTAO>2.0.CO;2](https://doi.org/10.1175/1520-0485(1993)023<1363:VOTTAO>2.0.CO;2)
- 771 Bopp, L., Resplandy, L., Untersee, A., Le Mezo, P., Kageyama, M., 2017. Ocean (de)
772 oxygenation from the Last Glacial Maximum to the twenty-first century: insights from Earth
773 System models. *Philos. Trans. R. Soc. Math. Phys. Eng. Sci.* 375, 20160323.
- 774 Bryan, K., Lewis, L.J., 1979. A water mass model of the World Ocean. *J. Geophys. Res.*
775 *Oceans* 84, 2503–2517. <https://doi.org/10.1029/JC084iC05p02503>
- 776 Carmichael, M.J., Inglis, G.N., Badger, M.P.S., Naafs, B.D.A., Behrooz, L., Remmelzwaal,
777 S., Monteiro, F.M., Rohrsen, M., Farnsworth, A., Buss, H.L., Dickson, A.J., Valdes, P.J.,
778 Lunt, D.J., Pancost, R.D., 2017. Hydrological and associated biogeochemical consequences of
779 rapid global warming during the Paleocene-Eocene Thermal Maximum. *Glob. Planet. Change*
780 157, 114–138. <https://doi.org/10.1016/j.gloplacha.2017.07.014>
- 781 Cimoli, L., Mashayek, A., Johnson, H.L., Marshall, D.P., Naveira Garabato, A.C., Whalen,
782 C.B., Vic, C., De Lavergne, C., Alford, M.H., MacKinnon, J.A., Talley, L.D., 2023.
783 Significance of Diapycnal Mixing Within the Atlantic Meridional Overturning Circulation.
784 *AGU Adv.* 4, e2022AV000800. <https://doi.org/10.1029/2022AV000800>
- 785 Clarkson, M.O., Lenton, T.M., Andersen, M.B., Bagard, M.-L., Dickson, A.J., Vance, D.,
786 2021. Upper limits on the extent of seafloor anoxia during the PETM from uranium isotopes.
787 *Nat. Commun.* 12, 399. <https://doi.org/10.1038/s41467-020-20486-5>
- 788 Crameri, F., Shephard, G.E., Heron, P.J., 2020. The misuse of colour in science
789 communication. *Nat. Commun.* 11, 5444. <https://doi.org/10.1038/s41467-020-19160-7>
- 790 de Lavergne, C., Groeskamp, S., Zika, J., Johnson, H.L., 2022. The role of mixing in the
791 large-scale ocean circulation, in: *Ocean Mixing*. Elsevier, pp. 35–63.
792 <https://doi.org/10.1016/B978-0-12-821512-8.00010-4>
- 793 de Lavergne, C., Madec, G., Roquet, F., Holmes, R.M., McDougall, T.J., 2017. Abyssal
794 ocean overturning shaped by seafloor distribution. *Nature* 551, 181–186.
795 <https://doi.org/10.1038/nature24472>
- 796 de Lavergne, C., Vic, C., Madec, G., Roquet, F., Waterhouse, A.F., Whalen, C.B., Cuypers,
797 Y., Bouruet-Aubertot, P., Ferron, B., Hibiya, T., 2020. A Parameterization of Local and
798 Remote Tidal Mixing. *J. Adv. Model. Earth Syst.* 12, e2020MS002065.
799 <https://doi.org/10.1029/2020MS002065>
- 800 Dickson, A.J., Cohen, A.S., Coe, A.L., 2012. Seawater oxygenation during the Paleocene-
801 Eocene Thermal Maximum. *Geology* 40, 639–642. <https://doi.org/10.1130/G32977.1>
- 802 Dickson, A.J., Rees-Owen, R.L., März, C., Coe, A.L., Cohen, A.S., Pancost, R.D., Taylor, K.,
803 Shcherbinina, E., 2014. The spread of marine anoxia on the northern Tethys margin during
804 the Paleocene-Eocene Thermal Maximum: Tethys redox during the PETM. *Paleoceanography*
805 29, 471–488. <https://doi.org/10.1002/2014PA002629>
- 806 Dunne, J.P., Sarmiento, J.L., Gnanadesikan, A., 2007. A synthesis of global particle export
807 from the surface ocean and cycling through the ocean interior and on the seafloor. *Glob.*
808 *Biogeochem. Cycles* 21, 2006GB002907. <https://doi.org/10.1029/2006GB002907>

809 Egbert, G.D., Ray, R.D., 2000. Significant dissipation of tidal energy in the deep ocean
810 inferred from satellite altimeter data. *Nature* 405, 775–778.

811 Evans, D., Sagoo, N., Renema, W., Cotton, L.J., Müller, W., Todd, J.A., Saraswati, P.K.,
812 Stassen, P., Ziegler, M., Pearson, P.N., Valdes, P.J., Affek, H.P., 2018. Eocene greenhouse
813 climate revealed by coupled clumped isotope-Mg/Ca thermometry. *Proc. Natl. Acad. Sci.*
814 115, 1174–1179. <https://doi.org/10.1073/pnas.1714744115>

815 Fichfet, T., Maqueda, M.A.M., 1997. Sensitivity of a global sea ice model to the treatment of
816 ice thermodynamics and dynamics. *J. Geophys. Res. Oceans* 102, 12609–12646.
817 <https://doi.org/10.1029/97JC00480>

818 Gargett, A.E., 1984. Vertical eddy diffusivity in the ocean interior. *J. Mar. Res.* 42, 359–393.
819 <https://doi.org/10.1357/002224084788502756>

820 Garrett, C., Kunze, E., 2007. Internal Tide Generation in the Deep Ocean. *Annu. Rev. Fluid*
821 *Mech.* 39, 57–87. <https://doi.org/10.1146/annurev.fluid.39.050905.110227>

822 Gaspar, P., Grégoris, Y., Lefevre, J., 1990. A simple eddy kinetic energy model for
823 simulations of the oceanic vertical mixing: Tests at station Papa and long-term upper ocean
824 study site. *J. Geophys. Res. Oceans* 95, 16179–16193.
825 <https://doi.org/10.1029/JC095iC09p16179>

826 Green, J.A.M., Huber, M., 2013. Tidal dissipation in the early Eocene and implications for
827 ocean mixing. *Geophys. Res. Lett.* 40, 2707–2713. <https://doi.org/10.1002/grl.50510>

828 Green, M., Hadley-Pryce, D., Scotese, C., 2023. Phanerozoic (541 Ma-present day), in: *A*
829 *Journey Through Tides*. Elsevier, pp. 157–184.

830 Heinemann, M., Jungclaus, J.H., Marotzke, J., 2009. Warm Paleocene/Eocene climate as
831 simulated in ECHAM5/MPI-OM. *Clim Past* 5, 785–802. [https://doi.org/10.5194/cp-5-785-](https://doi.org/10.5194/cp-5-785-2009)
832 2009

833 Heinze, M., Ilyina, T., 2015. Ocean biogeochemistry in the warm climate of the late
834 Paleocene. *Clim. Past* 11, 63–79. <https://doi.org/10.5194/cp-11-63-2015>

835 Herold, N., Buzan, J., Seton, M., Goldner, A., Green, J.A.M., Müller, R.D., Markwick, P.,
836 Huber, M., 2014. A suite of early Eocene (~ 55 Ma) climate model boundary conditions.
837 *Geosci. Model Dev.* 7, 2077–2090. <https://doi.org/10.5194/gmd-7-2077-2014>

838 Holmes, R.M., Zika, J.D., Griffies, S.M., Hogg, A.McC., Kiss, A.E., England, M.H., 2021.
839 The Geography of Numerical Mixing in a Suite of Global Ocean Models. *J. Adv. Model.*
840 *Earth Syst.* 13, e2020MS002333. <https://doi.org/10.1029/2020MS002333>

841 Hourdin, F., Foujols, M.-A., Codron, F., Guemas, V., Dufresne, J.-L., Bony, S., Denvil, S.,
842 Guez, L., Lott, F., Ghattas, J., Braconnot, P., Marti, O., Meurdesoif, Y., Bopp, L., 2013.
843 Impact of the LMDZ atmospheric grid configuration on the climate and sensitivity of the
844 IPSL-CM5A coupled model. *Clim. Dyn.* 40, 2167–2192. [https://doi.org/10.1007/s00382-012-](https://doi.org/10.1007/s00382-012-845)
845 1411-3

846 Huber, M., Caballero, R., 2011. The early Eocene equable climate problem revisited. *Clim.*
847 *Past* 7, 603–633. <https://doi.org/10.5194/cp-7-603-2011>

848 Hutchinson, D.K., De Boer, A.M., Coxall, H.K., Caballero, R., Nilsson, J., Baatsen, M., 2018.
849 Climate sensitivity and meridional overturning circulation in the late Eocene using GFDL
850 CM2.1. *Clim. Past* 14, 789–810. <https://doi.org/10.5194/cp-14-789-2018>

851 Ilyina, T., Heinze, M., 2019. Carbonate Dissolution Enhanced by Ocean Stagnation and
852 Respiration at the Onset of the Paleocene-Eocene Thermal Maximum. *Geophys. Res. Lett.* 46,
853 842–852. <https://doi.org/10.1029/2018GL080761>

854 Jayne, S.R., 2009. The Impact of Abyssal Mixing Parameterizations in an Ocean General
855 Circulation Model. *J. Phys. Oceanogr.* 39, 1756–1775.
856 <https://doi.org/10.1175/2009JPO4085.1>

857 Krinner, G., Viovy, N., De Noblet-Ducoudré, N., Ogée, J., Polcher, J., Friedlingstein, P.,
858 Ciais, P., Sitch, S., Prentice, I.C., 2005. A dynamic global vegetation model for studies of the

859 coupled atmosphere-biosphere system. *Glob. Biogeochem. Cycles* 19, 2003GB002199.
860 <https://doi.org/10.1029/2003GB002199>

861 Laugié, M., Donnadieu, Y., Ladant, J., Bopp, L., Ethé, C., Raison, F., 2021. Exploring the
862 Impact of Cenomanian Paleogeography and Marine Gateways on Oceanic Oxygen.
863 *Paleoceanogr. Paleoclimatology* 36, e2020PA004202. <https://doi.org/10.1029/2020PA004202>

864 Lazar, A., Madec, G., Delecluse, P., 1999. The Deep Interior Downwelling, the Veronis
865 Effect, and Mesoscale Tracer Transport Parameterizations in an OGCM. *J. Phys. Oceanogr.*
866 29, 2945–2961. [https://doi.org/10.1175/1520-0485\(1999\)029<2945:TDIDTV>2.0.CO;2](https://doi.org/10.1175/1520-0485(1999)029<2945:TDIDTV>2.0.CO;2)

867 Liu, Z., Pagani, M., Zinniker, D., DeConto, R., Huber, M., Brinkhuis, H., Shah, S.R., Leckie,
868 R.M., Pearson, A., 2009. Global cooling during the Eocene-Oligocene Climate Transition.
869 *Science* 323, 1187–1190.

870 Lu, W., Rickaby, R.E.M., Hoogakker, B.A.A., Rathburn, A.E., Burkett, A.M., Dickson, A.J.,
871 Martínez-Méndez, G., Hillenbrand, C.-D., Zhou, X., Thomas, E., Lu, Z., 2020. I/Ca in
872 epifaunal benthic foraminifera: A semi-quantitative proxy for bottom water oxygen in a multi-
873 proxy compilation for glacial ocean deoxygenation. *Earth Planet. Sci. Lett.* 533, 116055.
874 <https://doi.org/10.1016/j.epsl.2019.116055>

875 Lunt, D.J., Bragg, F., Chan, W.-L., Hutchinson, D.K., Ladant, J.-B., Morozova, P.,
876 Niezgodzki, I., Steinig, S., Zhang, Z., Zhu, J., Abe-Ouchi, A., Anagnostou, E., De Boer,
877 A.M., Coxall, H.K., Donnadieu, Y., Foster, G., Inglis, G.N., Knorr, G., Langebroek, P.M.,
878 Lear, C.H., Lohmann, G., Poulsen, C.J., Sepulchre, P., Tierney, J.E., Valdes, P.J., Volodin,
879 E.M., Dunkley Jones, T., Hollis, C.J., Huber, M., Otto-Bliesner, B.L., 2021. DeepMIP: model
880 intercomparison of early Eocene climatic optimum (EECO) large-scale climate features and
881 comparison with proxy data. *Clim. Past* 17, 203–227. <https://doi.org/10.5194/cp-17-203-2021>

882 Lunt, D.J., Huber, M., Anagnostou, E., Baatsen, M.L.J., Caballero, R., DeConto, R., Dijkstra,
883 H.A., Donnadieu, Y., Evans, D., Feng, R., Foster, G.L., Gasson, E., Von Der Heydt, A.S.,
884 Hollis, C.J., Inglis, G.N., Jones, S.M., Kiehl, J., Kirtland Turner, S., Korty, R.L., Kozdon, R.,
885 Krishnan, S., Ladant, J.-B., Langebroek, P., Lear, C.H., LeGrande, A.N., Littler, K.,
886 Markwick, P., Otto-Bliesner, B., Pearson, P., Poulsen, C.J., Salzmann, U., Shields, C., Snell,
887 K., Stärz, M., Super, J., Tabor, C., Tierney, J.E., Tourte, G.J.L., Tripathi, A., Upchurch, G.R.,
888 Wade, B.S., Wing, S.L., Winguth, A.M.E., Wright, N.M., Zachos, J.C., Zeebe, R.E., 2017.
889 The DeepMIP contribution to PMIP4: experimental design for model simulations of the
890 EECO, PETM, and pre-PETM (version 1.0). *Geosci. Model Dev.* 10, 889–901.
891 <https://doi.org/10.5194/gmd-10-889-2017>

892 MacKinnon, J.A., Zhao, Z., Whalen, C.B., Waterhouse, A.F., Trossman, D.S., Sun, O.M., St.
893 Laurent, L.C., Simmons, H.L., Polzin, K., Pinkel, R., Pickering, A., Norton, N.J., Nash, J.D.,
894 Musgrave, R., Merchant, L.M., Melet, A.V., Mater, B., Legg, S., Large, W.G., Kunze, E.,
895 Klymak, J.M., Jochum, M., Jayne, S.R., Hallberg, R.W., Griffies, S.M., Diggs, S.,
896 Danabasoglu, G., Chassignet, E.P., Buijsman, M.C., Bryan, F.O., Briegleb, B.P., Barna, A.,
897 Arbic, B.K., Ansong, J.K., Alford, M.H., 2017. Climate Process Team on Internal Wave–
898 Driven Ocean Mixing. *Bull. Am. Meteorol. Soc.* 98, 2429–2454.
899 <https://doi.org/10.1175/BAMS-D-16-0030.1>

900 Madec, G., Imbard, M., 1996. A global ocean mesh to overcome the North Pole singularity.
901 *Clim. Dyn.* 12, 381–388.

902 Madec, G., the NEMO team, 2016. NEMO ocean engine. *Notes Pô Modélisation Inst. Pierre-*
903 *Simon Laplace* 27, ISSN No 1288-1619.

904 Marshall, J., Speer, K., 2012. Closure of the meridional overturning circulation through
905 Southern Ocean upwelling. *Nat. Geosci.* 5, 171–180. <https://doi.org/10.1038/ngeo1391>

906 Meissner, K.J., Bralower, T.J., Alexander, K., Jones, T.D., Sijp, W., Ward, M., 2014. The
907 Paleocene-Eocene Thermal Maximum: How much carbon is enough? *Paleoceanography* 29,
908 946–963. <https://doi.org/10.1002/2014PA002650>

909 Melet, A., Legg, S., Hallberg, R., 2016. Climatic Impacts of Parameterized Local and Remote
910 Tidal Mixing. *J. Clim.* 29, 3473–3500. <https://doi.org/10.1175/JCLI-D-15-0153.1>

911 Melet, A.V., Hallberg, R., Marshall, D.P., 2022. The role of ocean mixing in the climate
912 system, in: *Ocean Mixing*. Elsevier, pp. 5–34. [https://doi.org/10.1016/B978-0-12-821512-](https://doi.org/10.1016/B978-0-12-821512-8.00009-8)
913 [8.00009-8](https://doi.org/10.1016/B978-0-12-821512-8.00009-8)

914 Merryfield, W.J., Holloway, G., Gargett, A.E., 1999. A Global Ocean Model with Double-
915 Diffusive Mixing. *J. Phys. Oceanogr.* 29, 1124–1142. [https://doi.org/10.1175/1520-](https://doi.org/10.1175/1520-0485(1999)029<1124:AGOMWD>2.0.CO;2)
916 [0485\(1999\)029<1124:AGOMWD>2.0.CO;2](https://doi.org/10.1175/1520-0485(1999)029<1124:AGOMWD>2.0.CO;2)

917 Meurdesoif, Y., Caubel, A., Lacroix, R., Déroutillat, J., Nguyen, M.H., 2016. XIOS tutorial.
918 [Httpforgeipsl.jussieu.fr/ioserver/attach.-Tutorialpdf](http://forgeipsl.jussieu.fr/ioserver/attach/tutorial.pdf).

919 Middelburg, J.J., Soetaert, K., Herman, P.M.J., Heip, C.H.R., 1996. Denitrification in marine
920 sediments: A model study. *Glob. Biogeochem. Cycles* 10, 661–673.
921 <https://doi.org/10.1029/96GB02562>

922 Munk, W., Wunsch, C., 1998. Abyssal recipes II: Energetics of tidal and wind mixing. *Deep*
923 *Sea Res.* 45, 1977–2010.

924 Munk, W.H., 1966. Abyssal recipes. *Deep Sea Res.* 13, 707–730.

925 Pälike, C., Delaney, M.L., Zachos, J.C., 2014. Deep-sea redox across the Paleocene-Eocene
926 thermal maximum. *Geochem. Geophys. Geosystems* 15, 1038–1053.
927 <https://doi.org/10.1002/2013GC005074>

928 Saenko, O.A., 2006. The Effect of Localized Mixing on the Ocean Circulation and Time-
929 Dependent Climate Change. *J. Phys. Oceanogr.* 36, 140–160.
930 <https://doi.org/10.1175/JPO2839.1>

931 Saenko, O.A., Merryfield, W.J., 2005. On the Effect of Topographically Enhanced Mixing on
932 the Global Ocean Circulation. *J. Phys. Oceanogr.* 35, 826–834.
933 <https://doi.org/10.1175/JPO2722.1>

934 Schmittner, A., Egbert, G.D., 2014. An improved parameterization of tidal mixing for ocean
935 models. *Geosci. Model Dev.* 7, 211–224. <https://doi.org/10.5194/gmd-7-211-2014>

936 Schmittner, A., Green, J.A.M., Wilmes, S. -B., 2015. Glacial ocean overturning intensified by
937 tidal mixing in a global circulation model. *Geophys. Res. Lett.* 42, 4014–4022.
938 <https://doi.org/10.1002/2015GL063561>

939 Sepulchre, P., Caubel, A., Ladant, J.-B., Bopp, L., Boucher, O., Braconnot, P., Brockmann,
940 P., Cozic, A., Donnadieu, Y., Dufresne, J.-L., Estella-Perez, V., Ethé, C., Fluteau, F., Foujols,
941 M.-A., Gastineau, G., Ghattas, J., Hauglustaine, D., Hourdin, F., Kageyama, M., Khodri, M.,
942 Marti, O., Meurdesoif, Y., Mignot, J., Sarr, A.-C., Servonnat, J., Swingedouw, D., Szopa, S.,
943 Tardif, D., 2020. IPSL-CM5A2 – an Earth system model designed for multi-millennial
944 climate simulations. *Geosci. Model Dev.* 13, 3011–3053. [https://doi.org/10.5194/gmd-13-](https://doi.org/10.5194/gmd-13-3011-2020)
945 [3011-2020](https://doi.org/10.5194/gmd-13-3011-2020)

946 Sharoni, S., Halevy, I., 2023. Rates of seafloor and continental weathering govern
947 Phanerozoic marine phosphate levels. *Nat. Geosci.* 16, 75–81. [https://doi.org/10.1038/s41561-](https://doi.org/10.1038/s41561-022-01075-1)
948 [022-01075-1](https://doi.org/10.1038/s41561-022-01075-1)

949 Simmons, H.L., Jayne, S.R., Laurent, L.C.St., Weaver, A.J., 2004. Tidally driven mixing in a
950 numerical model of the ocean general circulation. *Ocean Model.* 6, 245–263.
951 [https://doi.org/10.1016/S1463-5003\(03\)00011-8](https://doi.org/10.1016/S1463-5003(03)00011-8)

952 Song, P., Sidorenko, D., Scholz, P., Thomas, M., Lohmann, G., 2023. The tidal effects in the
953 Finite-volume Sea ice–Ocean Model (FESOM2.1): a comparison between parameterised tidal
954 mixing and explicit tidal forcing. *Geosci. Model Dev.* 16, 383–405.
955 <https://doi.org/10.5194/gmd-16-383-2023>

956 St. Laurent, L., Garrett, C., 2002. The Role of Internal Tides in Mixing the Deep Ocean. *J.*
957 *Phys. Oceanogr.* 32, 2882–2899. [https://doi.org/10.1175/1520-](https://doi.org/10.1175/1520-0485(2002)032<2882:TROITI>2.0.CO;2)
958 [0485\(2002\)032<2882:TROITI>2.0.CO;2](https://doi.org/10.1175/1520-0485(2002)032<2882:TROITI>2.0.CO;2)

959 Talley, L., 2013. Closure of the Global Overturning Circulation Through the Indian, Pacific,
960 and Southern Oceans: Schematics and Transports. *Oceanography* 26, 80–97.
961 <https://doi.org/10.5670/oceanog.2013.07>

962 Thomas, D.J., Korty, R., Huber, M., Schubert, J.A., Haines, B., 2014. Nd isotopic structure of
963 the Pacific Ocean 70–30 Ma and numerical evidence for vigorous ocean circulation and ocean
964 heat transport in a greenhouse world. *Paleoceanography* 29, 454–469.
965 <https://doi.org/10.1002/2013PA002535>

966 Toggweiler, J.R., Samuels, B., 1998. On the Ocean’s Large-Scale Circulation near the Limit
967 of No Vertical Mixing. *J. Phys. Oceanogr.* 28, 1832–1852. [https://doi.org/10.1175/1520-0485\(1998\)028<1832:OTOSLS>2.0.CO;2](https://doi.org/10.1175/1520-0485(1998)028<1832:OTOSLS>2.0.CO;2)

969 Toggweiler, J.R., Samuels, B., 1995. Effect of Drake passage on the global thermohaline
970 circulation. *Deep Sea Res. Part Oceanogr. Res. Pap.* 42, 477–500.
971 [https://doi.org/10.1016/0967-0637\(95\)00012-U](https://doi.org/10.1016/0967-0637(95)00012-U)

972 Valcke, S., 2013. The OASIS3 coupler: a European climate modelling community software.
973 *Geosci. Model Dev.* 6, 373–388. <https://doi.org/10.5194/gmd-6-373-2013>

974 Vic, C., Naveira Garabato, A.C., Green, J.A.M., Waterhouse, A.F., Zhao, Z., Melet, A., De
975 Lavergne, C., Buijsman, M.C., Stephenson, G.R., 2019. Deep-ocean mixing driven by small-
976 scale internal tides. *Nat. Commun.* 10, 2099. <https://doi.org/10.1038/s41467-019-10149-5>

977 Wanninkhof, R., 1992. Relationship between wind speed and gas exchange over the ocean. *J.*
978 *Geophys. Res. Oceans* 97, 7373–7382. <https://doi.org/10.1029/92JC00188>

979 Weber, T., Thomas, M., 2017. Influence of ocean tides on the general ocean circulation in the
980 early Eocene. *Paleoceanography* 32, 553–570. <https://doi.org/10.1002/2016PA002997>

981 Whalen, C.B., de Lavergne, C., Naveira Garabato, A.C., Klymak, J.M., MacKinnon, J.A.,
982 Sheen, K.L., 2020. Internal wave-driven mixing: governing processes and consequences for
983 climate. *Nat. Rev. Earth Environ.* 1, 606–621. <https://doi.org/10.1038/s43017-020-0097-z>

984 Whitehead, J.A., 1998. Topographic control of oceanic flows in deep passages and straits.
985 *Rev. Geophys.* 36, 423–440. <https://doi.org/10.1029/98RG01014>

986 Wilmes, S.-B., Green, J.A.M., Schmittner, A., 2021. Enhanced vertical mixing in the glacial
987 ocean inferred from sedimentary carbon isotopes. *Commun. Earth Environ.* 2, 166.
988 <https://doi.org/10.1038/s43247-021-00239-y>

989 Winguth, A.M.E., Thomas, E., Winguth, C., 2012. Global decline in ocean ventilation,
990 oxygenation, and productivity during the Paleocene-Eocene Thermal Maximum: Implications
991 for the benthic extinction. *Geology* 40, 263–266. <https://doi.org/10.1130/G32529.1>

992 Xue, P., Chang, L., Dickens, G.R., Thomas, E., 2022. A Depth-Transect of Ocean
993 Deoxygenation During the Paleocene-Eocene Thermal Maximum: Magnetofossils in
994 Sediment Cores From the Southeast Atlantic. *J. Geophys. Res. Solid Earth* 127,
995 e2022JB024714. <https://doi.org/10.1029/2022JB024714>

996 Xue, P., Chang, L., Thomas, E., 2023. Abrupt Northwest Atlantic deep-sea oxygenation
997 decline preceded the Palaeocene-Eocene Thermal Maximum. *Earth Planet. Sci. Lett.* 618,
998 118304. <https://doi.org/10.1016/j.epsl.2023.118304>

999 Yao, W., Paytan, A., Wortmann, U.G., 2018. Large-scale ocean deoxygenation during the
1000 Paleocene-Eocene Thermal Maximum. *Science* 361, 804–806.
1001 <https://doi.org/10.1126/science.aar8658>

1002 Zhang, Y., De Boer, A.M., Lunt, D.J., Hutchinson, D.K., Ross, P., Van De Flierdt, T., Sexton,
1003 P., Coxall, H.K., Steinig, S., Ladant, J., Zhu, J., Donnadieu, Y., Zhang, Z., Chan, W., Abe-
1004 Ouchi, A., Niezgodzki, I., Lohmann, G., Knorr, G., Poulsen, C.J., Huber, M., 2022. Early
1005 Eocene Ocean Meridional Overturning Circulation: The Roles of Atmospheric Forcing and
1006 Strait Geometry. *Paleoceanogr. Paleoclimatology* 37, e2021PA004329.
1007 <https://doi.org/10.1029/2021PA004329>

1008 Zhang, Y., Huck, T., Lique, C., Donnadieu, Y., Ladant, J.-B., Rabineau, M., Aslanian, D.,

1009 2020. Early Eocene vigorous ocean overturning and its contribution to a warm Southern
1010 Ocean. *Clim. Past* 16, 1263–1283. <https://doi.org/10.5194/cp-16-1263-2020>
1011 Zhou, X., Thomas, E., Rickaby, R.E.M., Winguth, A.M.E., Lu, Z., 2014. I/Ca evidence for
1012 upper ocean deoxygenation during the PETM. *Paleoceanography* 29, 964–975.
1013 <https://doi.org/10.1002/2014PA002702>
1014 Zhou, X., Thomas, E., Winguth, A.M.E., Ridgwell, A., Scher, H., Hoogakker, B.A.A.,
1015 Rickaby, R.E.M., Lu, Z., 2016. Expanded oxygen minimum zones during the late Paleocene-
1016 early Eocene: Hints from multiproxy comparison and ocean modeling. *Paleoceanography* 31,
1017 1532–1546. <https://doi.org/10.1002/2016PA003020>
1018

Impacts of tidally driven internal mixing in the Early Eocene Ocean

Jean-Baptiste Ladant¹, Jeanne Millot-Weil^{1,*}, Casimir de Lavergne², J. A. Mattias Green³, Sébastien Nguyen¹, Yannick Donnadiou⁴

¹Laboratoire des Sciences du Climat et de l'Environnement, LSCE/IPSL, CEA-CNRS-UVSQ, Université Paris-Saclay, 91191, Gif-sur-Yvette, France.

²Laboratoire d'Océanographie et du Climat : Expérimentations et Approches Numériques, IPSL, Sorbonne Université/IRD/CNRS/MNHN, Paris, France.

³School of Ocean Sciences, Bangor University, Menai Bridge, UK.

⁴Aix Marseille Université, CNRS, IRD, INRA, Coll France, CEREGE, Aix-en-Provence, France

Corresponding author: Jean-Baptiste Ladant (jean-baptiste.ladant@lsce.ipsl.fr)

*Now at: School of Geographical Sciences, University of Bristol, Bristol, UK.

Key Points:

- Inclusion of realistic near-field tidal mixing substantially modifies global deep ocean circulation in the Early Eocene.
- These tidally-driven changes yield significantly different biogeochemical properties of water masses, in particular in the Atlantic.
- The simulation that includes tidal mixing compares more favorably to inferences from the O₂ proxy record.

34 **Abstract**

35

36 Diapycnal mixing in the ocean interior is largely fueled by internal tides. Mixing schemes that
37 represent the breaking of internal tides are now routinely included in ocean and earth system
38 models applied to the modern and future. However, this is more rarely the case in climate
39 simulations of deep-time intervals of the Earth, for which estimates of the energy dissipated by
40 the tides are not always available. Here, we present and analyze two IPSL-CM5A2 earth system
41 model simulations of the Early Eocene made under the framework of DeepMIP. One simulation
42 includes mixing by locally dissipating internal tides, while the other does not. We show how
43 the inclusion of tidal mixing alters the shape of the deep ocean circulation, and thereby of large-
44 scale biogeochemical patterns, in particular dioxygen distributions. In our simulations, the
45 absence of tidal mixing leads to a deep North Atlantic basin mostly disconnected from the
46 global ocean circulation, which promotes the development of a basin-scale pool of oxygen-
47 deficient waters, at the limit of complete anoxia. The absence of large-scale anoxic records in
48 the deep ocean posterior to the Cretaceous anoxic events suggests that such an ocean state most
49 likely did not occur at any time across the Paleogene. This highlights how crucial it is for
50 climate models applied to the deep-time to integrate the spatial variability of tidally-driven
51 mixing as well as the potential of using biogeochemical models to exclude aberrant dynamical
52 model states for which direct proxies do not exist.

53

54

55 **1. Introduction**

56

57 Tides are the main supplier of diapycnal mixing in the ocean's interior, beneath the surface
58 boundary layers (e.g., Egbert and Ray, 2000; Vic et al., 2019; de Lavergne et al., 2020).
59 Barotropic tidal currents flowing over sloping bottom topography generate internal waves at
60 tidal frequency, called internal tides (Garrett and Kunze, 2007). The propagation, non-linear
61 interaction, and ultimate breaking of internal tides into three-dimensional turbulence constitutes
62 the primary contribution to diapycnal mixing (that is, mixing across isopycnals) and thus to
63 water mass transformation in the deep ocean (de Lavergne et al., 2022; Melet et al., 2022).
64 There are multiple pathways and processes leading to the dissipation of internal tide energy.
65 Small-scale internal tides tend to dissipate close to their generation site, whereas large-scale
66 internal tides dissipate more remotely, sometimes thousands of kilometers away from the
67 generation site (Whalen et al., 2020).

68

69 The modern global overturning circulation is usually schematized as a two-loop system,
70 consisting of an adiabatic upper cell fed by deep convection in the North Atlantic (the NADW)
71 overlying a largely diabatic lower cell fed by Antarctic Bottom Water (AABW) formation in
72 the Southern Ocean (Marshall and Speer, 2012; Talley, 2013; Melet et al., 2022). Diapycnal
73 mixing plays an important role in shaping this two-cell overturning circulation (Cimoli et al.,
74 2023); in particular the tidally-driven, bottom-intensified, part of the mixing is instrumental in
75 reducing the density of northward-flowing AABW and in mixing AABW with NADW (de
76 Lavergne et al., 2022; Melet et al., 2022). It is the specific geometry of the modern Southern
77 Ocean, with its continent-free latitudinal band down to a depth of ~ 2000 m at the Drake
78 Passage, that favors the adiabatic upwelling of deep waters (NADW and Pacific/Indian Deep
79 Waters) in the surface Ekman divergence of the Southern Ocean (Toggweiler and Samuels,
80 1995, 1998). This prompts the possibility that, in periods of the deep-time past of the Earth
81 when the Drake and/or Tasman gateways were closed or shallow, diapycnal (diabatic) mixing
82 may have played a greater role in setting the mode and intensity of the global overturning
83 circulation (Green and Huber, 2013).

84

85 Since the seminal work of Munk (1966), great efforts have been made to understand what
86 controls diapycnal mixing in the ocean interior (e.g., Munk and Wunsch, 1998; St. Laurent and
87 Garrett, 2002; MacKinnon et al., 2017) and to refine the parameterizations of vertical diffusivity
88 in ocean general circulation models (GCM) (e.g., Bryan and Lewis, 1979; Gargett, 1984;
89 Simmons et al., 2004; Saenko and Merryfield, 2005; Jayne, 2009; Schmittner and Egbert, 2014;
90 Melet et al., 2016; de Lavergne et al., 2020; Song et al., 2023). Recent work has
91 comprehensively reviewed what is currently known about the role of ocean mixing in the
92 climate system (Whalen et al., 2020; de Lavergne et al., 2022; Melet et al., 2022) and, in
93 particular, the contribution of different internal wave processes (e.g., near-field and far-field
94 internal tide dissipation, lee wave dissipation and wind-induced near-inertial wave energy
95 dissipation) to the total mixing. The parameterization of all of these processes into global ocean
96 models is a currently active area of research (MacKinnon et al., 2017) and, in climate models
97 applied to the deep-time past of the Earth, such processes are generally ignored. Instead, mixing
98 in the ocean interior is parameterized either by a constant background diffusivity coefficient or
99 by simple schemes such as a horizontally uniform but depth varying diffusivity (Bryan and
100 Lewis, 1979, hereafter BL).

101

102 In recent years though, some models applied to paleoclimate studies have started to include to
103 contribution of local (near-field) internal tide dissipation (e.g., Schmittner et al., 2015;
104 Hutchinson et al., 2018; Wilmes et al., 2021), following the bottom-intensified mixing
105 parameterization of Simmons et al. (2004, hereafter S04). Wilmes et al. (2021) notably show
106 that using appropriate Last Glacial Maximum tidal dissipation, instead of modern dissipation
107 with otherwise glacial forcings, invigorates the circulation in the ocean interior and increases
108 the fit with carbon isotope measurements. Hutchinson et al. (2018) compare the S04 scheme
109 with the previously-implemented BL scheme in Late Eocene GFDL CM2.1 earth system model
110 simulations and essentially find very little differences in terms of ocean circulation structure
111 and intensity and of water mass age. This is somehow contradictory to the same exercise
112 performed by Jayne (2009) using modern simulations carried out with the NCAR POP 1.4.3
113 ocean model. In the latter work, the change from the BL parameterization to an explicit tidal
114 mixing scheme leads to small impacts on the simulated ocean heat transport (OHT) and upper
115 ocean circulation (because of similar vertical diffusivity values there) but significantly
116 increases the intensity of the deep circulation (Jayne, 2009).

117

118 Another approach has consisted in adding an explicit tidal contribution to the momentum
119 equations rather than to the parameterization of vertical diffusivity (Weber and Thomas, 2017).
120 Though limited to relatively short integration time (100 years in their $3^\circ \times 2^\circ$ Early Eocene
121 ECHAM5/MPIOM configuration) because the explicit tidal forcing requires high resolution
122 simulations (Song et al., 2023), the simulations of Weber and Thomas (2017) report a weak
123 impact of tidal forcing on OHT and large-scale ocean circulation shape but a more significant
124 impact on the intensity of the overturning circulation, echoing the results of Jayne (2009).

125

126 More recently, Zhang et al. (2022) have explored the variability in ocean circulation in models
127 participating to the DeepMIP project on the Early Eocene (Lunt et al., 2017), in which the
128 models were forced by a set of Early Eocene forcings, identical across the models but for the
129 details of their implementation. The authors report large inter-model differences in simulated
130 ocean circulation structure and intensity (Zhang et al., 2022, their Figure 2). Interestingly, the
131 model simulating the most intense overturning circulation (IPSL-CM5A2) is one of the only
132 two DeepMIP models explicitly including a tidal-mixing contribution to vertical diffusivity.

133

134 Here, we investigate the impacts of the inclusion of near-field bottom-intensified tidal mixing
135 (using the S04 parameterization) on the ocean circulation and biogeochemistry in the Early

136 Eocene. We demonstrate that failing to include abyssal turbulent mixing leads to a stagnant
137 ocean with large areas of anoxia, which does not match proxy data from the Equatorial and
138 North Atlantic.

139

140

141 **2. Model and simulations**

142

143 2.1. IPSL-CM5A2 Earth System Model

144

145 The simulations presented in this work are performed with the IPSL-CM5A2 Earth System
146 Model (Sepulchre et al., 2020), itself composed of LMDZ for the atmosphere (Hourdin et al.,
147 2013), ORCHIDEE for the land surface and vegetation (Krinner et al., 2005), and NEMO
148 version 3.6 for the ocean (Madec and the NEMO team, 2016). NEMOv3.6 consists of the OPA
149 dynamic ocean model, the LIM2 sea-ice model (Fichefet and Maqueda, 1997) and the PISCES-
150 v2 marine biogeochemistry model (Aumont et al., 2015). OASIS (Valcke, 2013) is used to
151 couple the models, and XIOS (Meurdesoif et al., 2016) handles input/output processing. LMDZ
152 and ORCHIDEE shares the same horizontal resolution of $3.75^\circ \times 1.875^\circ$ (longitude x latitude)
153 and LMDZ is discretized into 39 uneven levels in the vertical. NEMO has a nominal horizontal
154 resolution of 2° , enhanced to 0.5° at the equator, and 31 vertical levels whose thickness varies
155 from 10 m at the surface to 500 m at the bottom. NEMO uses a tripolar grid to overcome the
156 North Pole singularity (Madec and Imbard, 1996). Previous deep-time paleoclimate modeling
157 with the IPSL-CM5A2 model (e.g., Laugié et al., 2021), including the IPSL-CM5A2
158 simulations carried out as part of the DeepMIP project (Zhang et al., 2020, 2022), used an
159 oceanic domain extending down to 78°S . Here the numerical ocean grid has been regenerated
160 and extended southward in latitude down to 85°S in order to better represent possible marine
161 incursions at latitudes poleward of 78°S in intervals of the last 100 Ma. We note, however, that
162 this represents a negligible issue in the standard DeepMIP paleogeography based on a hotspot
163 reference frame that we use here, though this would not be the case in Early Eocene
164 paleogeographies constructed with a paleomagnetic reference frame (Lunt et al., 2017).

165

166 2.2 Mixing in the ocean model

167

168 In this version of NEMO, vertical mixing in the water column is implemented as a Turbulent
169 Kinetic Energy (TKE) closure model (Gaspar et al., 1990; Blanke and Delecluse, 1993). This

170 closure is complemented with a parameterization for convection, consisting of enhanced
 171 vertical diffusion where stratification is unstable (Lazar et al., 1999), a parameterization for
 172 double diffusive mixing (Merryfield et al., 1999), and a tidal mixing parameterization following
 173 S04. The vertical eddy diffusivity coefficient K_v is thus expressed as:

$$175 \quad K_v = \max(K_0, K_{TKE}) + K_{ddm} + K_{Tides} \text{ for } N^2 > 0 \text{ (stable stratification)}$$

$$176 \quad K_v = K_{EVD} \text{ otherwise}$$

177
 178 with N the Brunt-Väisälä frequency, K_0 a background diffusivity effectively setting the
 179 minimum vertical diffusivity, K_{TKE} the diffusivity computed from the TKE scheme, K_{ddm} the
 180 diffusivity attributed to double diffusion, K_{Tides} the tidal diffusivity and K_{EVD} a prescribed
 181 constant convective diffusivity. Rigorously, the tidal and double diffusion schemes contribute
 182 to K_v even in regions of unstable stratification but the very large diffusivity value
 183 parameterizing convective processes renders these contributions negligible. Here, K_0 is set to
 184 $1.2 \cdot 10^{-5} \text{ m}^2 \text{ s}^{-1}$, $K_{EVD} = 100 \text{ m}^2 \text{ s}^{-1}$ and K_{Tides} has the form:

$$185 \quad K_{Tides} = \frac{q\Gamma EF}{\rho N^2} \quad (\text{Eq. 1})$$

186
 187 where q is the tidal dissipation efficiency, Γ is the mixing efficiency, E is the tidal energy flux
 188 from Green and Huber (2013), ρ is the water density, N is the buoyancy frequency along the
 189 seafloor and F is a vertical structure function that decays exponentially with height above
 190 bottom:
 191

$$192 \quad F(z) = \frac{e^{-\frac{H+z}{h_0}}}{h_0 \left(1 - e^{-\frac{H}{h_0}}\right)} \quad (\text{Eq. 2})$$

193
 194 with H the total depth of the water column and h_0 the vertical decay scale for turbulence.
 195 We use the standard model values of $q = \frac{1}{3}$, $\Gamma = 0.2$ and $h_0 = 500 \text{ m}$ (Madec and the NEMO
 196 team, 2016), which are identical to those originally chosen by S04.
 197

198 2.3 PISCES Marine Biogeochemistry Model

199
 200

201 The PISCES model (Pelagic Interactions Scheme for Carbon and Ecosystem Studies, Aumont
202 et al., 2015) simulates the lower trophic levels of marine ecosystems (nanophytoplankton,
203 diatoms, microzooplankton and mesozooplankton), carbonate chemistry and the
204 biogeochemical cycles of carbon, oxygen, and the main nutrients (phosphorus, nitrogen, iron
205 and silica). Dissolved oxygen is produced in the ocean by phytoplankton net primary production
206 and consumed by zooplankton heterotrophic respiration, oxic remineralization of organic
207 matter and nitrification. At the air-sea interface, dissolved oxygen is exchanged using the
208 parameterization of Wanninkhof (1992). The atmospheric concentration of dioxygen is set to a
209 fixed ratio of 0.21.

210

211 In the water column, PISCES explicitly represents two pools of organic matter particles that
212 differ in their average size (i.e., large and small particles) and respective sinking speed, as well
213 as a pool of semi-labile dissolved organic matter. The particle pools are degraded into the
214 dissolved one as a function of temperature and oxygen concentrations. Dissolved organic matter
215 undergoes oxic remineralization or denitrification depending on local oxygen levels. The
216 remineralization and denitrification rates are function of temperature, oxygen and nitrate
217 concentrations, and of the bacterial activity and biomass (Aumont et al., 2015). When reaching
218 the ocean floor in the form of particles, organic matter is permanently buried or degraded by
219 sedimentary denitrification or oxic remineralization. The proportion of buried carbon is
220 dependent on the organic carbon flux at the bottom and is computed according to Dunne et al.
221 (2007). The fraction of sedimentary denitrification versus oxic remineralization is computed
222 using the meta-model of Middelburg et al. (1996). Degraded organic carbon is then released
223 into the ocean bottom level in the form of DIC. Ocean bottom concentrations of dissolved
224 oxygen and nitrate are also consumed to account for sedimentary oxic remineralization and
225 denitrification, respectively (Aumont et al., 2015). In the absence of an explicit sediment
226 module, the global inventories in phosphate, nitrate, silicate and alkalinity are restored to
227 modern values so that the global mean ocean concentrations in these elements do not drift away
228 from modern mean concentrations (Aumont et al., 2015). We also use an additional inert
229 artificial tracer representing the age of water masses. This age tracer value is restored to 0 in
230 the top 10 m of the model ocean and increases at a rate of one year per year deeper than 10 m
231 (Bopp et al., 2017).

232

233 2.4 Experimental design

234

235 We present two numerical simulations of the Early Eocene based on the DeepMIP protocol
236 (Lunt et al., 2017). The boundary and initial conditions are essentially those of the 840 ppmv
237 simulations of Zhang et al. (2020), that is, we use the paleogeography of Herold et al. (2014)
238 with a prescribed atmospheric CO₂ concentration of 840 ppmv. The orbital parameters of the
239 Earth are those of present-day and other greenhouse gas concentrations are set to their
240 preindustrial values. The simulations are therefore representative of a pre-Paleocene-Eocene
241 Thermal Maximum interval, following the terminology of Lunt et al. (2017). The simulations
242 are initialized with ocean temperature and salinity distributions as in Zhang et al. (2020) and
243 only differ by the absence (“EE-noM2”) or presence (“EE-std”) of the contribution of near-
244 field internal tide energy dissipation (K_{Tides}) to the vertical diffusivity coefficient. In the
245 following, we will refer to the absence or presence of tidal mixing, though this is somewhat a
246 misnomer because the contribution of background diffusivity (i.e. K_0) to vertical diffusivity is
247 included in the two simulations. As described in S04, this background diffusivity may account
248 for the far-field dissipation of large-scale internal tides as well as other sources of mixing that
249 are not explicitly modeled, such as lee waves or wind-induced radiating near-inertial waves
250 (e.g., Melet et al., 2022).

251

252 In NEMOv3.6, the tidal energy flux E includes components for the M2, K1 and S2 tides
253 whereas Green and Huber (2013) provides an estimate only for the M2 tide (see Fig. S1 for a
254 map of the estimated M2 dissipation). Considering that 1) the M2 component dominates the
255 tide, and 2) the S2 energy flux is simply taken to be $\frac{1}{4}$ of the M2 energy flux in the NEMOv3.6
256 mixing scheme, we argue that using $\frac{5}{4}$ of the M2 estimate of Green and Huber (2013) as forcing
257 in the model (M2 + S2 contributions) is a reasonable first step, despite the missing K1
258 contribution.

259

260 The two simulations are run for 5100 model years after which both have reached quasi-
261 equilibrium with small residual trends in mean deep ocean (2750 – 4250 m) temperatures <
262 0.02°C/century (Fig. S2). The last 100 years of each model run are used to build a climatological
263 average for the ocean dynamics. In order to improve the equilibration of biogeochemistry, we
264 extend the simulations in an offline PISCES configuration for another 4000 model years. In this
265 setup, the monthly-mean climatological ocean dynamics is repeatedly read by PISCES to
266 calculate the evolution of the biogeochemical tracer fields. Again, we use the last 100 model
267 years to build a climatological average for the ocean biogeochemistry.

268

269

270 3. Results

271

272 3.1 Energetic considerations

273

274 3.1.1 Available energy

275

276 The tidal model used by Green and Huber (2013) yields an estimate of 1.44 TW of energy
277 dissipated in the Eocene ocean by the M2 barotropic tide, which, interpolated on the NEMO
278 grid, amounts to 1.473 TW. Because the tidal mixing scheme in NEMO includes the S2 tidal
279 contribution expressed as one-fourth of the M2 contribution, the total energy input from tides
280 is 1.841 TW, of which only one-third, 0.614 TW, is assumed to dissipate locally and employed
281 in the tidal mixing scheme (because $q = \frac{1}{3}$ in Equation (1) above).

282

283 The implementation of the tidal mixing scheme in the model is not fully consistent energetically
284 for two reasons. First, a fraction of the energy input is lost in the lower half of the bottom cells,
285 where stratification and diffusivity are not defined because of the no-flux boundary condition
286 at the bottom. Second, the model parameterization imposes an upper bound of $3 \times 10^{-2} \text{ m}^2 \cdot \text{s}^{-1}$ on
287 the tidal diffusivity (Madec and the NEMO team, 2016). Diagnosing the energy effectively
288 used by the tidal mixing scheme gives 0.42 TW, that is, about 70 % of the expected power
289 (0.614 TW).

290

291 We can compute the power consumption due to vertical mixing processes, expressed as in S04:

292

$$293 \quad P = \frac{1}{r} \int \rho K N^2 dV \quad (\text{Eq. 3})$$

294

295 Table 1 shows the amount of power consumed at the global scale and in each basin (Atlantic,
296 Pacific, Indian, Tethys and Arctic, represented on Fig. S3). At the global scale, the total power
297 consumed by diapycnal mixing in the model is 1.45 TW in EE-std. This is weaker than the 1.84
298 TW of total M2 + S2 tidal dissipation estimated by the model of Green and Huber (2013). Two
299 considerations shed light on this difference. First, the effective consumption by tidal vertical
300 mixing is only about 70 % of what is expected from Equation (1). Second, the background

301 diffusivity is simply prescribed and does not depend on the tidal dissipation; hence power
302 consumption by background mixing cannot be expected to match the unused two-thirds of
303 barotropic tidal energy loss.

304 Overall, we calculate that tidal mixing represents about 29 % of the total power consumed by
305 diapycnal mixing in the ocean interior. This ratio is only slightly lower to that simulated by
306 S04, somewhat surprisingly given the very different paleogeography and stratification of our
307 simulations. At the basin scale and excluding the Arctic basin, the contribution from tides
308 varies from 14 % of the total power in the Tethys basin to 32 % in the Pacific basin. This is
309 consistent with larger mean dissipation rates in the Pacific and Indian Oceans than in the
310 Atlantic and Tethys Oceans (Fig. S1).

311

312 3.1.2 Diapycnal diffusivity

313

314 The inclusion of tidal mixing substantially changes the amount of energy available to mix the
315 deep ocean. Diapycnal diffusivities are therefore considerably different both horizontally and
316 vertically in EE-std compared to EE-noM2.

317

318 In EE-noM2, the zonally averaged vertical diffusivity is generally close to the background value
319 except in the surface mixed-layer depth, in which mixing due to the winds generates elevated
320 vertical diffusivity, and in the Southern Ocean where deep convection processes mix waters
321 down to the abyss (Fig. 1a, c, e). At mid depths (2000 – 3000 m), the zonal mean vertical
322 diffusivity is elevated throughout the low latitudes (Fig. 1a). This signal mostly originates from
323 a relatively isolated abyssal sub-basin in the eastern Pacific Ocean between the East Pacific
324 Rise and the American continent (Fig. 1e) in which the weak stratification elevates K_{TKE} and
325 stimulates episodic convective instabilities. At 600 m depth (Fig. 1c), away from turbulent
326 wind-driven mixing, vertical diffusivity is close to the background value K_0 except in deep
327 convection zones of the Southern Ocean. Because the 600 m geopotential surface is also
328 generally far from bottom topography, adding tidal mixing in EE-std does not significantly alter
329 vertical diffusivity at this depth (Fig. 1d), except in deep-water formation zones close to the
330 Antarctic margins. By contrast, diffusivity at 3000 m depth is enhanced by about 2 orders of
331 magnitude in broad regions of the Pacific and Indian Oceans in EE-std relative to EE-noM2
332 (Fig. 1f). Note that because tidal mixing is implemented here as a bottom-intensified energy
333 dissipation, and because stratification generally decreases with depth, the maximum tidal
334 diffusivity in the vertical is found locally on the deepest ocean grid cell. The Atlantic basin in

335 the Eocene configuration exhibits a weaker tide than the Pacific (Green and Huber, 2013, see
336 also Fig. S1) and, therefore, vertical diffusivity does not increase as much as in the Pacific
337 Ocean in EE-std compared to EE-noM2. The zonally averaged vertical diffusivity essentially
338 shows that diapycnal mixing is substantially enhanced in the ocean interior. As we will show
339 in the next sections, the additional mixing energy available in the deep ocean has profound
340 consequences on the intensity of the overturning circulation and the pathways of water masses.

341

342 3.2 Surface changes

343

344 The upper-ocean (0 – 100 m) annual mean temperatures in EE-noM2 are roughly close to 10°C
345 in the Southern Ocean and to 5°C in the quasi-enclosed Arctic Ocean (Fig. 2a). They increase
346 equatorward to reach up to more than 37°C in the equatorial western Pacific. As expected from
347 similar simulations performed with the same model, this temperature distribution is really close
348 to that presented on Figure 2a of Zhang et al. (2020) (see Fig. S4 for a more detailed
349 comparison). Tidally-driven mixing leads to large changes in the Southern Ocean surface layer.
350 The Atlantic and Indian sectors of the Southern Ocean are warmer (locally more than 4K) in
351 EE-std than in EE-noM2 (Fig. 2b), whereas the Pacific sector is cooler, although the change is
352 smaller. Warmer (cooler) regions of the Southern Ocean in EE-std are also regions of increased
353 (decreased) upper ocean salinity (not shown).

354

355 In EE-noM2, deep convective areas are exclusively found in the Southern Ocean, in the
356 Atlantic, Indian and Pacific sectors (Fig. 2c), and there is no deep-water formation in the
357 Northern Hemisphere. The upper-ocean temperature changes in EE-std are sustained by
358 increased deep-water formation in the Atlantic and Indian sector of the Southern Ocean
359 compared to EE-noM2 as can be seen by the deepening of the winter mixed layer depth (MLD)
360 in these areas (Fig. 2d). In the South Atlantic, the MLD deepens by more than 1000 m and
361 enhances the temperature and salt advection feedback from the lower latitudes. In the Pacific
362 sector, the winter MLD instead slightly decreases, driving the opposite change in the advection
363 feedback. Figure S5 further shows that the deepening/shoaling of MLD in EE-std relative to
364 EE-noM2 is robust across the simulations and not simply an artifact of the averaging period.

365

366 3.3 Ocean circulation changes

367

368 The increase in available energy for mixing is reflected by a significant enhancement of the
369 global meridional overturning circulation (MOC) (Fig. 3). The MOC in the two simulations has
370 a roughly comparable shape consisting of a single anticlockwise overturning cell in the
371 Southern Hemisphere fed by deep-water formation in the Southern Ocean. The intensity of the
372 MOC and the penetration of deep-water in the abyss is however greater in EE-std than in EE-
373 noM2, although the maximum rate of overturning is similar in the two simulations (~ 35 Sv at
374 2000 m depth in EE-std and at 900 m depth in EE-noM2). Away from the Southern Ocean, the
375 additional tidal mixing energy sustains a stronger and deeper overturning cell extending up the
376 northern mid to high latitudes (8 Sv at 2000 m depth and 30°N in EE-std, Fig. 3b), effectively
377 increasing the ventilation of the EE-std ocean compared to EE-noM2 and acting to reduce
378 vertical tracer gradients.

379

380 This homogenization is evident from the global zonal mean distribution of temperature (Fig.
381 S6), which shows a globally warmer deep ocean (below ~ 1000 m) and a globally cooler upper
382 and intermediate ocean in EE-std compared to EE-noM2 at all latitudes except those of the
383 Southern Ocean ($80^\circ\text{S} - 40^\circ\text{S}$) where the ocean is globally warmer throughout the water
384 column. The EE-std ocean is thus more vertically well mixed than the EE-noM2 ocean.

385

386 The intensification of the global MOC has interesting consequences on the water mass
387 pathways, in particular in the Atlantic. Figure 4 shows the ocean current velocity and direction
388 at different depths in the South Atlantic and Southern Ocean. At 500 m depth, the western
389 boundary current flowing southward off the coast of South America is substantially increased
390 in EE-std. This increase confines the westward-flowing water masses close to Antarctica to the
391 Southern Ocean, whereas in EE-noM2, these waters mix with those from the South Atlantic
392 western boundary current towards the Indian Ocean. Deeper in the water column (1400 - 1800
393 m depth), the water masses flowing from the Atlantic to the Indian sector of the Southern Ocean
394 in EE-noM2 consist of recirculated waters from the Southern Ocean and locally-formed deep
395 waters, as the southward-flowing Atlantic western boundary current is absent. In contrast, in
396 EE-std, the southward western-boundary current is still active and contributes to exporting
397 water masses from the low-latitude Atlantic toward the Indian Ocean. In the abyss (3250 – 3750
398 m), only a very small fraction of the Southern Ocean water masses flows northward in the
399 Atlantic in EE-noM2 while most are exported eastward to the Indian Ocean. In EE-std an
400 intense northward current advects water masses along the western side of the basin into the
401 Equatorial and North Atlantic.

402

403 These results demonstrate that the deep Equatorial and North Atlantic Oceans are more isolated
404 from the global ocean circulation below ~ 1500 m in EE-noM2 than in EE-std. In the Early
405 Eocene, the deepest connections of the Atlantic basin are with the Southern Ocean because the
406 Central American, Tethys (Gibraltar) and Atlantic-Arctic gateways are all shallow and/or
407 narrow. Since the bathymetric configuration does not change between the two simulations, the
408 increased isolation of the EE-noM2 Equatorial and North Atlantic Oceans is purely caused by
409 lower levels of deep turbulent mixing, leading to major differences in Atlantic stratification and
410 circulation. In EE-std, tidal mixing renders abyssal water masses increasingly more buoyant as
411 they flow away from deep-water formation areas in the Southern Ocean whereas the buoyancy
412 gain across the Atlantic is weaker in EE-noM2. The isopycnal located at approximately 3000
413 m depth at 45°S (the 40.08 and 39.98 $\text{kg}\cdot\text{m}^{-3}$ σ_3 contour in EE-noM2 and EE-std respectively,
414 Fig. 5) indeed deepens to about 3400 m depth in EE-noM2 and 4500 m depth in EE-std at 35°N .
415 In other words, isopycnals of similar depth in the deep South Atlantic exhibit depth difference
416 in excess of 1 km upon reaching the deep North Atlantic. The larger northward deepening of
417 the isopycnals across the deep Atlantic generates a stronger meridional pressure gradient and,
418 thus, forces a more active deep northward circulation (e.g., Whitehead, 1998) in EE-std
419 compared to EE-noM2, leaving the latter more stagnant.

420

421 3.4 Biogeochemical changes

422

423 The more active deep circulation with tidal mixing also yields a significant reorganization of
424 the marine biogeochemistry in the deep ocean, in particular in the Atlantic. At the global scale,
425 though it is once again more evident in the Atlantic (Fig. 5c and d), the deep ocean ventilation
426 is reduced in the absence of tidal mixing. Notably, deep North Atlantic water masses are almost
427 3 times older in EE-noM2 than in EE-std. These deep water masses therefore exhibit very
428 different biogeochemical properties in EE-noM2 and EE-std, and this is particularly visible on
429 the distribution of dissolved oxygen across the water column.

430

431 In EE-noM2, the deep North Atlantic water masses possess the biogeochemical signature of
432 very old water masses: rich in nutrients and dissolved inorganic carbon (DIC) and poor in
433 oxygen. In fact, the North Atlantic is spectacularly oxygen-depleted (Fig. 6a), with hypoxia
434 (defined here as the 62.5 $\text{mmol}\cdot\text{m}^{-3}$ level) reached over the whole water column in the low
435 latitudes of the North Atlantic ($0 - 20^\circ\text{N}$) and below 800 m northward of 30°N . Anoxic levels

436 are reached northward of 20°N at depths between 1500 and 3000 m. The North Atlantic seafloor
437 is fully hypoxic and most of the coastal seafloor is anoxic (Fig. 6c). In contrast, deep North
438 Atlantic DIC and phosphate concentrations are high (Figs. S7 and S8) because falling organic
439 matter has been remineralized along the water mass journey and nutrients have therefore
440 accumulated in the deep ocean. Nitrate concentrations, however, rather decrease northward in
441 the deep Atlantic (Fig. S9) because the depletion in oxygen in this ocean basin triggers
442 denitrification to continue the remineralization process.

443

444 In EE-std, the younger water masses in the deep North Atlantic are relatively rich in oxygen
445 (Fig. 6b) and the seafloor is well oxygenated with only very limited hypoxic coastal areas. The
446 North Atlantic exhibits higher nitrate concentrations in EE-std than EE-noM2 in the deep (Fig.
447 S9), because the oxygen levels are above those required to trigger denitrification, and we find
448 lower DIC and phosphate concentrations (Figs. S7 and S8), as expected for better ventilated
449 water masses.

450

451 There are three main processes controlling the oxygenation of water masses in the ocean:
452 surface atmosphere-ocean interaction controlling the degree of solubility of O₂ in the ocean,
453 ocean circulation, and biological activity. Dissolved O₂ concentrations in the ocean can be
454 decomposed into a thermal and a non-thermal component, referred to as the saturation
455 component (O_{2sat}) and the Apparent Oxygen Utilization (AOU) respectively. O_{2sat} is the
456 concentration of O₂ that can be dissolved for a given temperature and salinity whereas AOU
457 integrates the contribution of ocean circulation and biology. These quantities are related as
458 such:

459

$$O_2 = O_{2sat} - AOU$$

460

461 As shown on Figure 7 for EE-noM2, surface O_{2sat} increases poleward because solubility
462 increases with decreasing temperatures (Fig. 7b). Surface O₂ concentrations are generally close
463 to O_{2sat} because, besides interacting with the atmosphere, the upper ocean layers gain dissolved
464 O₂ as the result of photosynthesis of marine phytoplankton. The AOU is therefore low (e.g., the
465 surface mid-latitudes on Fig. 7c). One notable exception is the equatorial subsurface ocean
466 because it is a region of upwelling that brings to the upper ocean water masses extremely rich
467 in nutrients allowing for intense phytoplanktonic activity. Consequently, large amounts of
468 organic matter sink and consume oxygen at a rate faster than the one at which the ocean restores
469 its O₂ concentration by atmospheric exchange.

470

471 In the intermediate and deep ocean, O_2 concentrations are close to O_{2sat} in the Southern Ocean
472 where deep convection occurs (Fig. 7a and b). As water masses age in the ocean interior (Fig.
473 7d), O_2 concentrations depart from O_{2sat} because of the increasing influence of remineralization
474 processes that consume oxygen in the water column (reflected by the increasing AOU, Fig. 7c).
475 In the deep North Atlantic, extremely old water masses that have not been in contact with the
476 atmosphere for more than a millennium exhibit AOU values almost equal to O_{2sat} , indicating
477 that almost all the available O_2 has been consumed.

478

479 Any change in dissolved O_2 concentrations between EE-noM2 and EE-std can therefore be
480 partitioned into the change in O_{2sat} , reflecting the change in temperature and, to a lesser extent,
481 salinity between EE-std and EE-noM2 and the change in AOU, which reflects circulation and
482 biological changes:

483

$$\Delta O_2 = \Delta O_{2sat} - \Delta AOU$$

484

485 In the Atlantic, the changes in dissolved O_2 concentrations are almost fully explained by
486 changes in AOU (Fig. 8). Interestingly, Figure 8 shows that contours of ΔAOU and of the water
487 age difference between EE-std and EE-noM2 are very well correlated, thereby strongly hinting
488 that the primary driver of oxygen changes is the reorganization of the ocean circulation
489 following the addition of tidally-driven mixing. This is also confirmed by the limited changes
490 in export productivity to the intermediate and deep ocean (Fig. S10).

491

492

493 **4. Discussion**

494

495 Our simulations compellingly demonstrate the crucial role played by tidally-driven abyssal
496 turbulent mixing in shaping the circulation and the distribution of biogeochemical tracers in the
497 ocean interior. However, apart from a few sensitivity simulations (Thomas et al., 2014; Weber
498 and Thomas, 2017; Hutchinson et al., 2018), most earth system models applied to deep-time
499 climates generally neglect tidally-driven mixing as a specific forcing and alter (or not) spatially-
500 constant coefficients in the implemented vertical mixing parameterization (e.g., Bryan and
501 Lewis, 1979) as a workaround (e.g., Zhang et al., 2022).

502

503 Hutchinson et al. (2018) find weak differences in terms of MOC shape and intensity and water
504 mass age between the standard BL scheme used in their CM2.1 Late Eocene simulations and
505 the same S04 bottom intensified mixing scheme as used here, indicating that the simulated
506 ocean circulation is largely similar. This is somewhat contradictory to the large change in MOC
507 intensity (and water age) found in our simulations, and we suggest a couple of explanatory
508 avenues. First, the standard BL scheme in Hutchinson et al. (2018) makes diffusivity increase
509 with depth—although without spatial dependence—and, as such, it is not rigorously similar to
510 prescribing a uniform background diffusivity coefficient K_0 . We note however that, comparing
511 the BL and S04 schemes in a modern configuration, Jayne (2009) observes a large enhancement
512 of the intensity of the deep cell of the MOC in S04 with little change in MOC structure, much
513 as we observe in our simulations. Second, though Hutchinson et al. (2018) apply the same S04
514 scheme as we do, their input dissipation rate E is recomputed directly using equation (2) of S04
515 and a uniform seafloor roughness amplitude whereas we prescribe E based on the explicit tidal
516 model of Green and Huber (2013). This results in quite different mean vertical diffusivities at
517 a basin-scale. In particular, their mean Atlantic diffusivity, when using the tidal scheme, is
518 much enhanced compared to their mean Pacific diffusivity, whereas we find the opposite ratio
519 in our simulations (Fig. S11 and Fig. 9 of Hutchinson et al., 2018). Our results are in agreement
520 with the enhanced Pacific dissipation found in the tidal model results of Green and Huber
521 (2013). Because the specifics of the calculation of the dissipation rate E are missing in
522 Hutchinson et al. (2018), it still remains unclear at this stage whether these differences stem
523 from (i) the spatial variability of the tidal forcing (which may be absent in Hutchinson et al.,
524 2018), (ii) a different model implementation of the S04 tidal dissipation scheme, (iii) the change
525 in tidal forcing across the 15 Myrs separating the Early and Late Eocene, or (iv) different levels
526 of spurious numerical mixing in GFDL-CM2.1 and IPSL-CM5A2 (e.g., Holmes et al., 2021).
527 This nonetheless suggests that the spatial distribution of the tidal forcing significantly alters the
528 simulated ocean circulation (Saenko, 2006; Jayne, 2009).

529

530 Using CCSM3-forced MITgcm simulations of the Early Eocene, which includes a Bryan-Lewis
531 diffusivity profile and an older reconstruction of the paleogeography, Thomas et al. (2014)
532 found that increasing the diffusivity beyond the standard BL coefficients allow for a large
533 increase in the intensity of the MOC and yield a circulation mode that compares better to
534 compiled Pacific ϵ_{Nd} data, in particular in the case in which abyssal mixing is increased. In an
535 additional sensitivity experiment, the authors increased the mixing approximately fivefold
536 throughout the water column; doing this significantly enhanced the poleward OHT and reduced

537 the meridional surface temperature gradients, in agreement with inferred proxy data as well as
538 previous investigations of increased upper ocean mixing effect on OHT (e.g., Jayne, 2009). In
539 our simulations, the meridional SST gradient is only weakly affected by the addition of tidal
540 mixing because vertical diffusivity in the upper 1000 m is similar in EE-noM2 and EE-std (Fig.
541 S11). Below 1000 m, diffusivity (and meridional transport) increases substantially in EE-std
542 but the vertical temperature gradient does not (Fig. S6) and the change in heat transport is small.
543 Thomas et al. (2014) however note that sustaining such elevated diffusivity across the water
544 column would require more than 20 TW; an amount of energy that tides cannot account for
545 (Green and Huber, 2013) and whose source has yet to be found.

546

547 Using the ECHAM5/MPIOM model with the Early Eocene paleogeography of Heinemann et
548 al. (2009), Weber and Thomas (2017) also investigated the response of the Eocene ocean
549 circulation to tides. They simulate the change in ocean circulation in a similar setup than the
550 one presented here, although the inclusion of tides in their model is represented by an additional,
551 explicit, tidal forcing on the momentum equations rather than the parameterization of the
552 contribution of tides to vertical diffusivity (Song et al., 2023). The simulated ocean circulation
553 of Weber and Thomas (2017) exhibits deep-water formation in the Southern Atlantic, as here,
554 but also in the North Atlantic. As in our experiments, adding tidal influence does not
555 substantially modify the location of deep-water formation regions, in contrast to the penetration
556 depth of these deep waters, but the limited integration time of their tidal simulation (100 years)
557 prompts the possibility that it might not have reached sufficient equilibrium. One possible
558 reason, among others (see, e.g., Zhang et al., 2022), explaining the different regions of deep
559 convective activity is the paleogeographic reconstruction, which, in Weber and Thomas (2017),
560 possesses in particular closed Drake Passage and Tasman Gateway and a more widely opened
561 Central American Seaway compared to the Herold et al. (2014) reconstruction that we use. We
562 indeed note that the recent DeepMIP study of Zhang et al. (2022) on Early Eocene ocean
563 circulation highlights that all of the models—with the Herold et al. (2014) paleogeography—
564 produce deep-water formation in the Southern Ocean (regardless of the sector) at the exception
565 of the GFDL model, which exhibits deep convective activity in the North Pacific, and the
566 NorESM model, which does not exhibit any deep-water formation, possibly because of
567 insufficient spinup. In contrast, the models do not produce deep-water formation in the North
568 Atlantic. Though the details of the ocean circulation differ between our simulations and those
569 of Weber and Thomas (2017), the addition of tidal mixing has similar effects on the simulated
570 circulation. Weber and Thomas (2017) also report an increase in the intensity of the MOC but

571 hardly any increase in ocean heat transport, in keeping with the notion that the impacts of the
572 Eocene tide are concentrated in the abyssal ocean (Green and Huber, 2013).

573

574 In a recent comparison of the S04 tidal mixing scheme vs. explicit tidal forcing, both approaches
575 were implemented in the FESOM2 ocean model (Song et al., 2023). The authors conclude that
576 while the parameterized tidal mixing may miss some potentially important effects, such as the
577 enhancement of bottom drag and continental shelf viscous dissipation, the explicit tidal forcing
578 typically requires resolution of the order of 0.1° to produce realistic impacts. As a result, lower
579 resolution simulations compare less favorably to observed hydrography with this scheme than
580 with the S04 parameterization. It also makes the inclusion of explicit tidal forcing currently
581 inapplicable to long-term deep-time climate simulations (Song et al., 2023).

582

583 Other studies have attempted to simulate the biogeochemical state of the Early Eocene (e.g.,
584 Heinze and Ilyina, 2015), generally in order to focus on the PETM perturbation (Winguth et
585 al., 2012; Meissner et al., 2014; Ilyina and Heinze, 2019). In particular, Winguth et al. (2012)
586 and Heinze and Ilyina (2015) have used modelling setups consisting of biogeochemical models
587 of resolution and complexity similar to PISCES and forced by or coupled to ocean-atmosphere
588 general circulation models, but the prescribed paleogeography and atmospheric CO_2 bear no
589 consistency between the studies unlike more recent coordinated efforts such as DeepMIP (Lunt
590 et al., 2017, 2021). Deep O_2 concentrations exhibit large differences between the simulations:
591 the 1120 ppmv CO_2 simulation of Winguth et al. (2012) generates a well oxygenated Pacific
592 Ocean and a more poorly oxygenated Atlantic Ocean whereas the 560 ppmv CO_2 simulation of
593 Heinze and Ilyina (2015) shows a better oxygenated Atlantic than Pacific Ocean. In our
594 simulations with tidal mixing at 840 ppmv, the deep Atlantic is better oxygenated than the
595 Pacific (Fig. S12) but the equatorial Atlantic oxygen minimum zone is more developed and has
596 lower O_2 concentrations. Interestingly, the primary production patterns in the upper ocean are
597 more similar, with for instance intense primary production in most of the equatorial Pacific, in
598 the eastern side of the Pacific and Atlantic Oceans as well as in the Southern Ocean. This
599 suggests that the diversity in O_2 distributions across the simulations largely reflects the
600 simulated ocean circulation, at least in the deep ocean.

601

602 There is currently no quantitative proxy for O_2 concentrations in the past, although semi-
603 quantitative multi-proxy approaches can provide estimates of poorly oxygenated bottom water
604 conditions ($\leq 50 \mu\text{mol/kg}$) (Lu et al., 2020). Most studies therefore report qualitative estimates

605 of the local oxygenation state of the ocean relative to a baseline value, using redox-sensitive
606 proxies such as the I/Ca ratio (e.g., Zhou et al., 2014, 2016), trace elements like molybdenum
607 or manganese (Dickson et al., 2012, 2014; Pälike et al., 2014) or magnetofossils (Xue et al.,
608 2022, 2023). Anoxic bottom water masses are perhaps more easily identifiable because the
609 sedimentary abundance of trace elements is strongly redox dependent and sedimentary
610 enrichment above average crustal values via complexification with sulfide elements is
611 interpreted as reflecting high dissolved sulfide concentrations and thus anoxic/euxinic
612 conditions (Dickson et al., 2012, 2014). If the distribution of Early Eocene redox archives is
613 relatively global (though concentrated in the peri-Tethys area, see Figure 6 of Carmichael et
614 al., 2017), the information conveyed by these estimates remains potentially strongly influenced
615 by local settings (Clarkson et al., 2021). A complementary approach therefore consists in
616 estimating the global area or volume occupied by anoxic or euxinic waters, using the isotopic
617 ratio of molybdenum (Dickson et al., 2012), sulfur (Yao et al., 2018) or uranium (Clarkson et
618 al., 2021), rather than reporting local estimates of bottom water oxygenation. For instance,
619 combining uranium isotope measurements from ODP Site 865 (Allison Guyot, equatorial
620 Pacific Ocean), DSDP Site 401 (Bay of Biscay, northeast Atlantic Ocean) and ODP Site 690
621 (Maud Rise, Atlantic sector of Southern Ocean) with box modelling, Clarkson et al. (2021)
622 propose a maximal extent of seafloor anoxia of 0.25 % prior to the PETM perturbation and 2
623 % at the PETM.

624

625 In the following, we compare the simulated oxygen concentrations in EE-noM2 and EE-std
626 with available data across a transect in the Atlantic using reported oxygen conditions at each
627 site (Fig. 9) and compute the extent of anoxic seafloor simulated by the model. Three main
628 observations can be made. First, the qualitative nature of the proxy leaves room for various
629 interpretations. At the exception of Site 1262 and 1266 at Walvis Ridge for whose oxygen-rich
630 conditions have been reported by the different proxies (Pälike et al., 2014; Xue et al., 2022),
631 low oxygen content is estimated at every site but the degree of oxygen deficiency is unclear
632 because anywhere between the anoxic ($0 \mu\text{mol/L}$) and hypoxic threshold ($\sim 60 - 70 \mu\text{mol/L}$,
633 Lu et al., 2020; Laugié et al., 2021). Second, at face value, the simulated O_2 concentrations are
634 probably too low in EE-noM2, in particular in the North Atlantic, and too high in EE-std. Third,
635 the fact that reported qualitative oxygen conditions in the data on Figure 9 reflect pre-PETM
636 conditions and that most of these proxies suggest decreasing oxygen concentrations across the
637 PETM perturbation but without extensive anoxia leads to the conservative assumption that the
638 pre-PETM ocean did not exhibit large-scale conditions too close to anoxia. In this regard, the

639 simulated oxygen concentrations suggest that the ocean biogeochemical state in EE-noM2 is
640 probably aberrant. This is confirmed by our calculation of the extent of anoxic seafloor,
641 respectively 2.3 % in EE-noM2 and 0.1 % in EE-std, which also suggests an excess in oxygen
642 depletion in EE-noM2 compared to pre-PETM estimates (Clarkson et al., 2021).

643

644 In addition, here, we do not *stricto sensu* model the biogeochemical conditions of the pre-PETM
645 as, for instance, the global mean nutrient concentrations in phosphate, nitrate, alkalinity and
646 silicate in the ocean are identical to the modern. Recent statistical box-modelling instead
647 suggests that the marine phosphate concentrations reached a peak in the Paleogene, thus
648 promoting higher primary productivity and lower deep-ocean O₂ concentrations (Sharoni and
649 Halevy, 2023). All else being equal, prescribing a higher marine nutrient content in our
650 simulations would decrease oxygen concentrations in both EE-noM2 and EE-std but with
651 opposite effect on the model-data comparison. In EE-std, this would reduce the model-data
652 mismatch because simulated O₂ concentrations are likely too high whereas in EE-noM2, it
653 would increase the proportion of anoxic waters and thereby increase the mismatch with
654 estimates from the geological record. The model-data mismatch in EE-std could be even further
655 reduced with a better representation of the smaller meridional temperature gradients that are
656 inferred from proxy data (e.g., Huber and Caballero, 2011; Evans et al., 2018) because this
657 would act to reduce the amount of oxygen stored in surface waters, and therefore decrease O₂
658 concentrations throughout the water column. This also implies that the simulated O₂
659 concentrations in EE-noM2 are likely a conservatively “high-concentration” estimate and thus
660 that the aberrant biogeochemical state likely reflects an aberrant Early Eocene dynamical ocean
661 in EE-noM2.

662

663 Finally, we note that the input energy dissipation from the M2 tide that was used here is not
664 exactly appropriate because the tidal model of Green and Huber (2013) was run with the ocean
665 stratification obtained from the low-resolution equilibrated CCSM3 simulations discussed in
666 Liu et al. (2009) instead of having been run with the IPSL-CM5A2 stratification. However,
667 these simulations use a bathymetry close to that used in Green and Huber (2013) and the abyssal
668 tidal dissipation is relatively insensitive to moderate changes in stratification. In addition, both
669 our simulations and those of Liu et al. (2009) exhibit deep-water formation in the Southern
670 Ocean. We thus argue that our results would not be significantly affected if the stratification
671 from our simulations had been used in the tidal model simulations. In contrast, a larger impact
672 is likely to be expected by the use of a higher-resolution bathymetric dataset in an improved

673 version of the tidal inversion model of Green and Huber (2013), such as that proposed in Green
674 et al. (2023), and we ambition to investigate this possibility in a near future. Alternatively, a
675 promising way lies in the use of comprehensive tidal mixing schemes accounting for both near-
676 field and far-field dissipation of internal tides (de Lavergne et al., 2020), rather than schemes
677 fixing vertical diffusivity, such as the BL scheme, or including only near-field mixing, such as
678 the S04 scheme used here.

679

680

681 **Conclusion**

682

683 Using Early Eocene IPSL-CM5A2 earth system model simulations, we demonstrate the
684 critically-overlooked impact of including a realistic estimate of the abyssal mixing driven by
685 the near-field dissipation of internal tides in deep-time paleoclimate simulations. In our
686 simulations, the global deep ocean circulation is substantially altered by the inclusion of abyssal
687 tidal mixing, in particular in the Atlantic basin, and the global meridional overturning
688 circulation is more intense and penetrates deeper in the ocean interior. This consequently drives
689 large changes in the biogeochemical properties of deep water masses. In particular, we show
690 that failing to include this abyssal turbulent mixing leads to a stagnant deep North Atlantic
691 ocean with large anoxic areas that compares less favorably to qualitative reconstruction of
692 paleo-oxygenation for this period than the more vigorous deep Atlantic ocean simulated in the
693 experiment with realistic tidal mixing. Our results therefore stress the importance of routinely
694 including abyssal turbulent mixing in upcoming deep-time paleoclimate studies and underline
695 how the use of an adjunct biogeochemical model can help disentangle dynamical ocean modes
696 for which proxies are lacking.

697

698

699 **Acknowledgment**

700 This work used computing hours on the HPC resources of the TGCC under GENCI allocations
701 A0110102212 and A0130102212. We are grateful to Olivier Marti, Laurent Bopp, Olivier
702 Aumont and Christian Ethé for discussions and help with the simulation setup. NCL
703 (<https://www.ncl.ucar.edu>) was used to make figures and most analyses, in addition to Fortran.
704 Figures use color maps developed by Fabio Cramer (Cramer et al., 2020). JAMG
705 acknowledges funding from the UK Natural Environment Research Council (grants
706 NE/F014821/1 and NE/S009566/1). YD acknowledges funding from the National Agency for

707 Research (ANR) project OXYMORE (grant 18-CE31-0020). The authors declare no conflict
708 of interest.

709
710

711 **Data availability**

712 Code availability. LMDZ, NEMO (including PISCES), ORCHIDEE and XIOS are released
713 under the terms of the CeCILL license. OASIS-MCT is released under the terms of the Lesser
714 GNU General Public License (LGPL). IPSL-CM5A2 source code is available via modipsl with
715 the command lines:

```
716 svn co -r 6039 https://forge.ipsl.jussieu.fr/igcmg/svn/modipsl/trunk modipsl;  
717 cd modipsl/util; ./model IPSLCM5A2.2
```

718 The model revision numbers used in this work can be found in the modipsl/util/mod.def file:

- 719 - NEMOGCM branch nemo_v3_6_STABLE revision 6665
- 720 - XIOS2 branches/xios-2.5 revision 1903
- 721 - IOIPSL/src svn tags/v2_2_2
- 722 - LMDZ5 branches/IPSLCM5A2.1 rev 3907
- 723 - ORCHIDEE branches/ORCHIDEE-IPSLCM5A2.1 rev 7376
- 724 - OASIS3-MCT 2.0_branch (rev 4775 IPSL server)

725 We recommend to refer to the project website for a proper installation and compilation of the
726 environment:

727 https://forge.ipsl.jussieu.fr/igcmg_doc/wiki/Doc/Config/IPSLCM5A2, last access: 21/11/2023.

728

729 Model outputs. NetCDF outputs and scripts to produce the figures used in this study are stored
730 at <https://doi.org/10.5281/zenodo.10246071>.

731
732
733
734
735
736
737
738
739
740

741 **Tables and figures**

742

		Power consumption used for diapycnal mixing (TW)			Fraction of power consumption due to tides
		K ₀	Tides	Total	
Global	EE-std	1.03	0.422	1.45	0.29
	EE-noM2	1.02	0	1.02	0
Pacific	EE-std	0.590	0.282	0.872	0.32
	EE-noM2	0.584	0	0.584	0
Atlantic	EE-std	0.162	0.0560	0.218	0.26
	EE-noM2	0.160	0	0.160	0
Indian	EE-std	0.145	0.0661	0.211	0.31
	EE-noM2	0.140	0	0.140	0
Tethys	EE-std	0.109	0.0175	0.127	0.14
	EE-noM2	0.108	0	0.108	0
Arctic	EE-std	0.0278	5 10 ⁻⁴	0.0283	0.02
	EE-noM2	0.0255	0	0.0255	0

Table 1. Power consumed by diapycnal mixing and fraction of power consumption due to tides calculated at the global-scale and for individual basins shown on Figure S3.

743

744

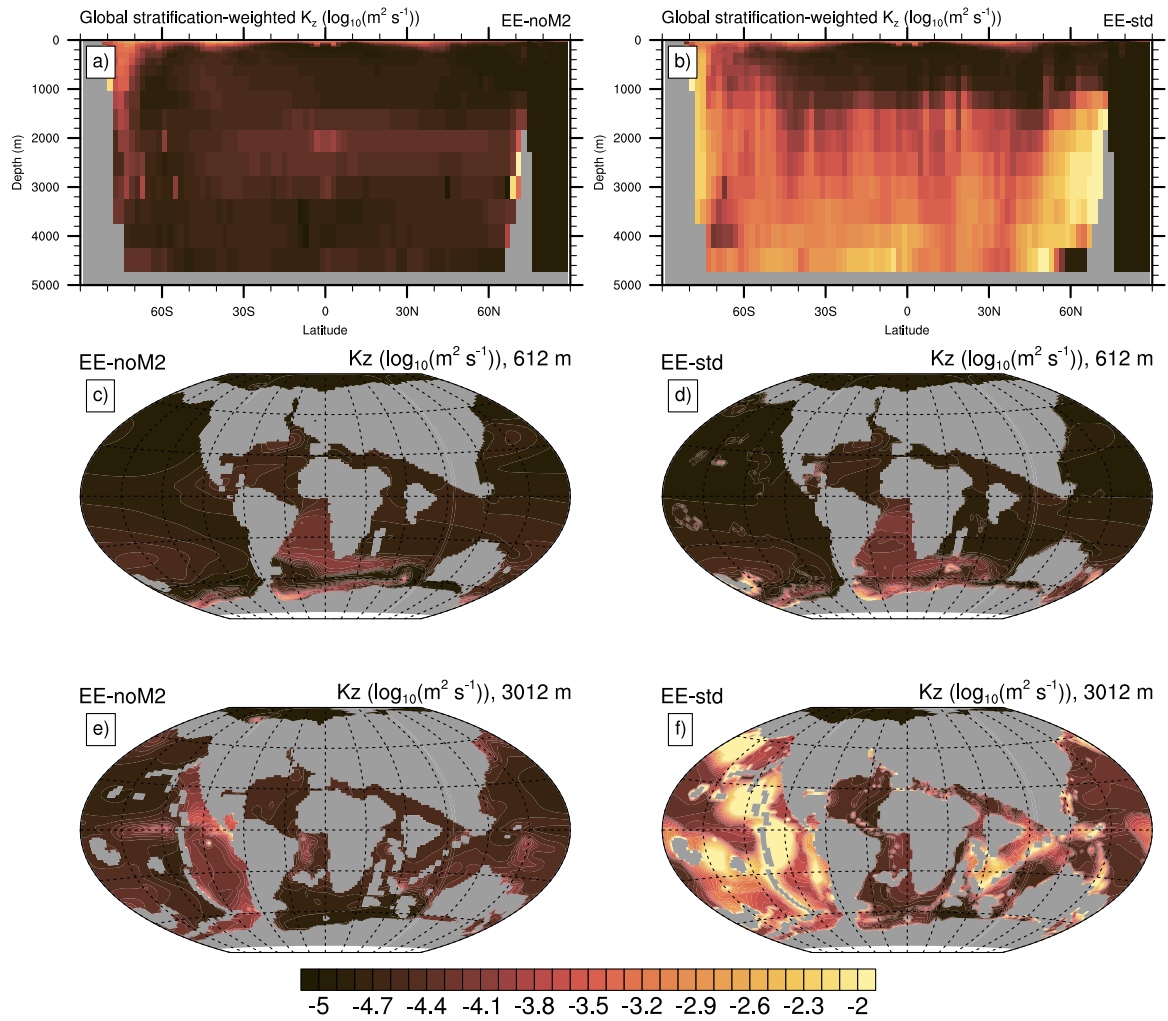


Figure 1. Stratification-weighted global zonal average of vertical diffusivity for EE-noM2 (a) and EE-std (b) ($\log_{10}(\text{m}^2 \text{s}^{-1})$). Diffusivity at 600 m and 3000 m for EE-noM2 (c, e) and EE-std (d, f) ($\log_{10}(\text{m}^2 \text{s}^{-1})$).

745

746

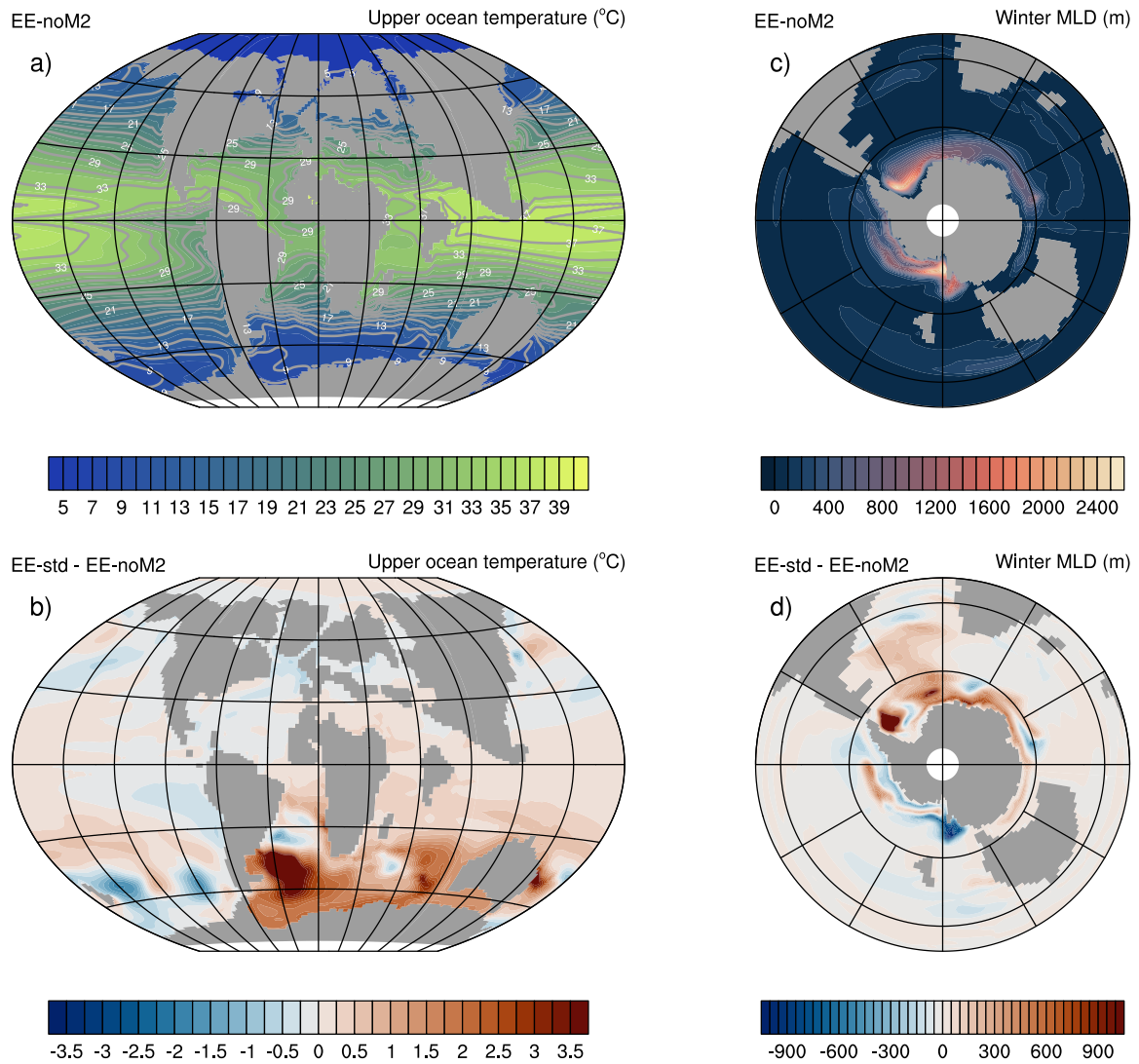


Figure 2. (a) EE-std mean annual upper ocean (0-100 m) temperatures ($^{\circ}\text{C}$). (b) Mean annual upper ocean temperature (0-100 m) difference ($^{\circ}\text{C}$) between EE-noM2 and EE-std. (c) Mean winter MLD (m) in EE-noM2. (d) Mean winter MLD difference (m) between EE-std and EE-noM2.

747

748

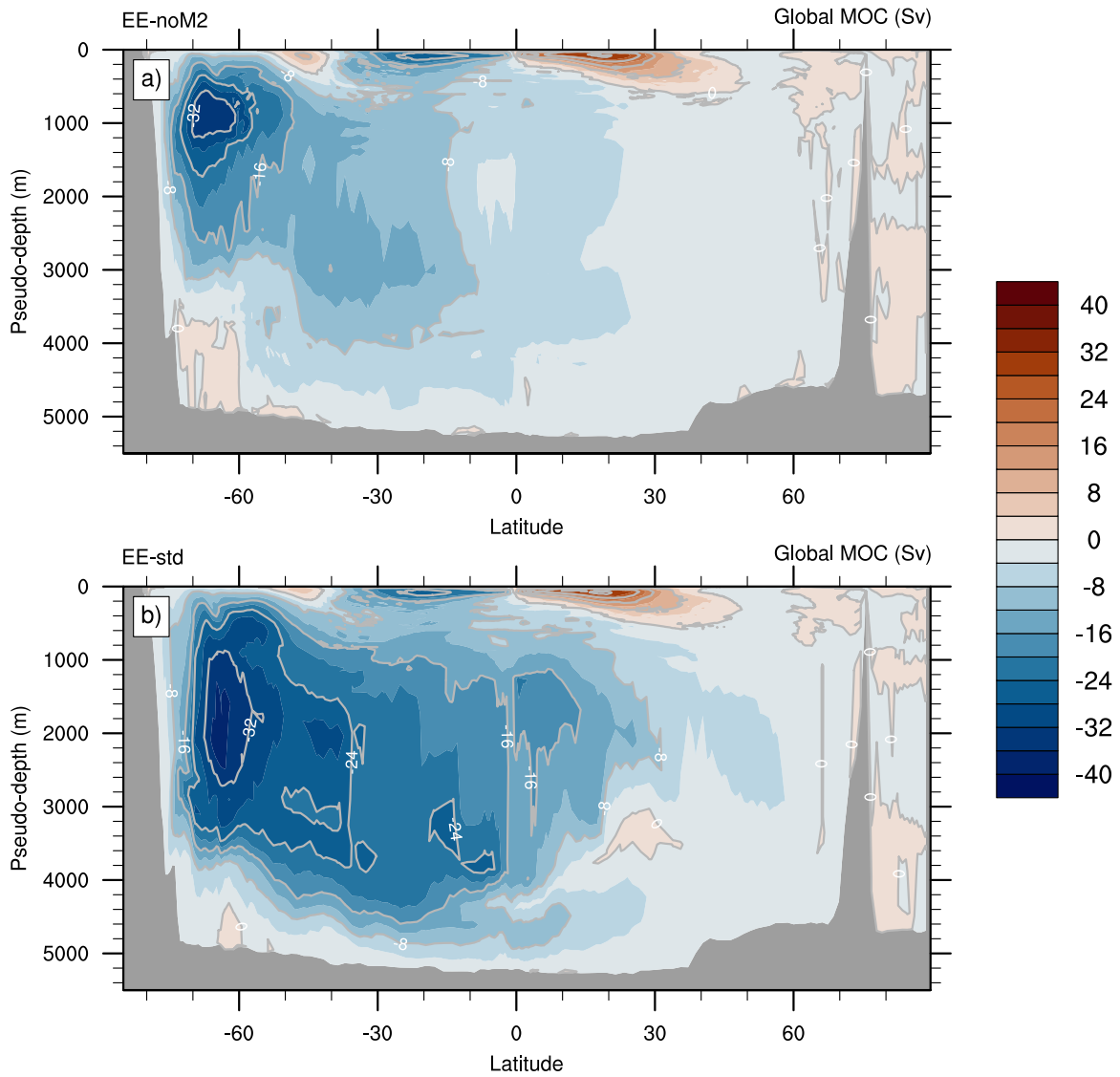


Figure 3. Global meridional overturning streamfunction (Sv) in EE-std (a) and EE-noM2 (b). Note that the MOC has been computed in density coordinates and reprojected to a pseudo-depth, following de Lavergne et al. (2017).

749

750

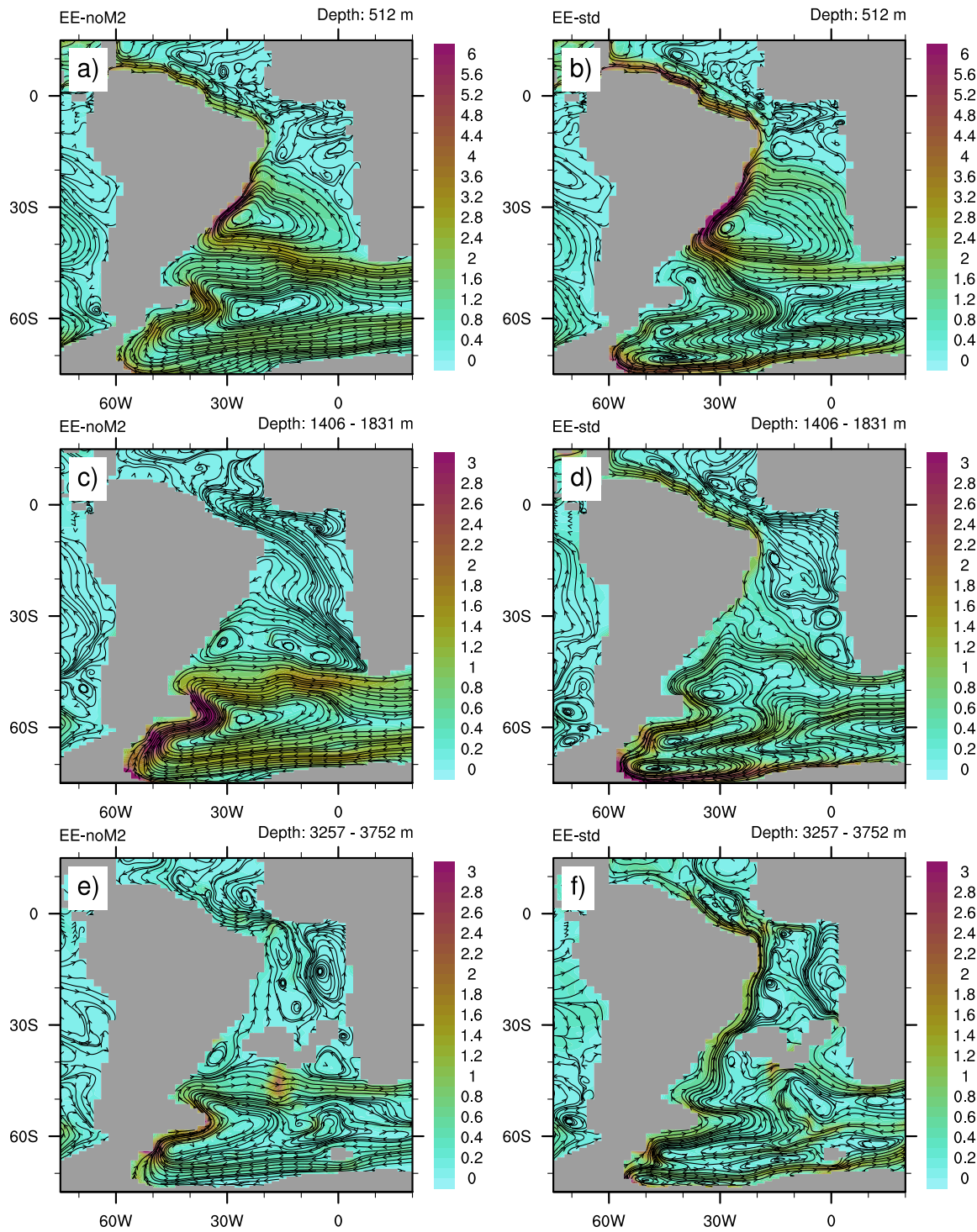


Figure 4. Ocean velocity (cm s⁻¹) at 500 m depth (a,b), averaged between 1400 and 1800 m (c, d) and averaged between 3250 and 3750 m (e, f) in EE-noM2 (a, c, e) and EE-std (b, d, f).

751

752

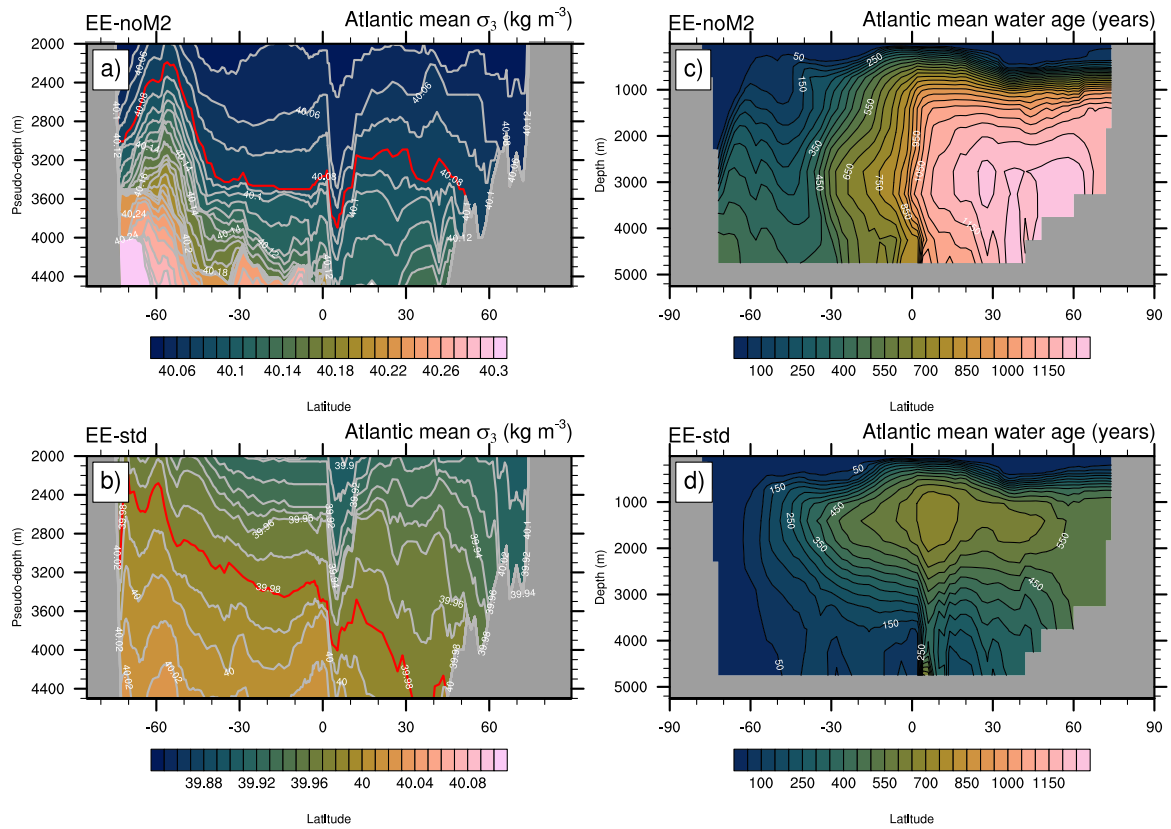


Figure 5. Zonally-averaged s_3 isopycnal profiles (kg m^{-3}) across the deep Atlantic in EE-noM2 (a) and EE-std (b) computed in density coordinates and reprojected to a pseudo-depth. The 40.08 and 39.98 kg m^{-3} s_3 contours are highlighted in red in (a) and (b) respectively, for easier visualization. Zonally averaged water age profile across the Atlantic in EE-noM2 (c) and EE-std (d). Note the different vertical axes between the two columns.

753

754

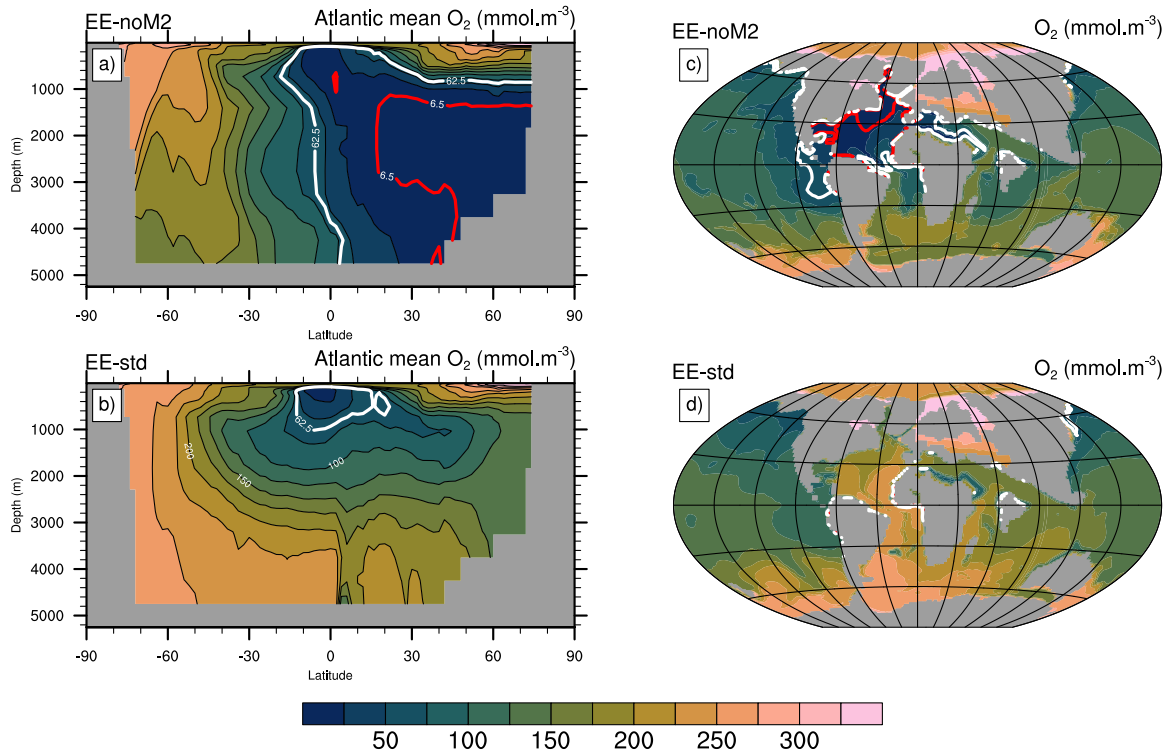


Figure 6. Zonally-averaged dissolved oxygen concentrations (mmol m^{-3}) across the Atlantic in EE-noM2 (a) and EE-std (b). Dissolved oxygen concentrations (mmol m^{-3}) at the seafloor in EE-noM2 (c) and EE-std (d). The hypoxic (62.5 mmol m^{-3}) and anoxic (6.5 mmol m^{-3}) thresholds (Laugié et al., 2021) are contoured in white and red, respectively.

755

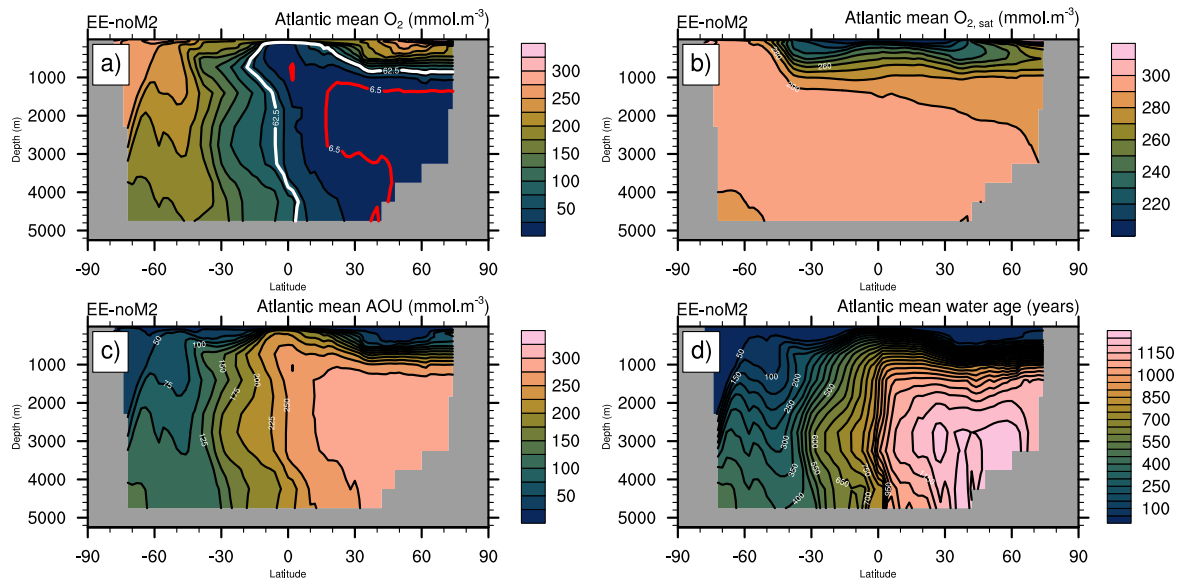


Figure 7. Zonally averaged (a) dissolved oxygen concentrations (mmol m^{-3}), (b) $\text{O}_{2\text{sat}}$ (mmol m^{-3}), (c) AOU (mmol m^{-3}) and (d) water age (years) across the Atlantic in EE-noM2. Note the different scale in panel (b) relative to (a) and (c).

756

757

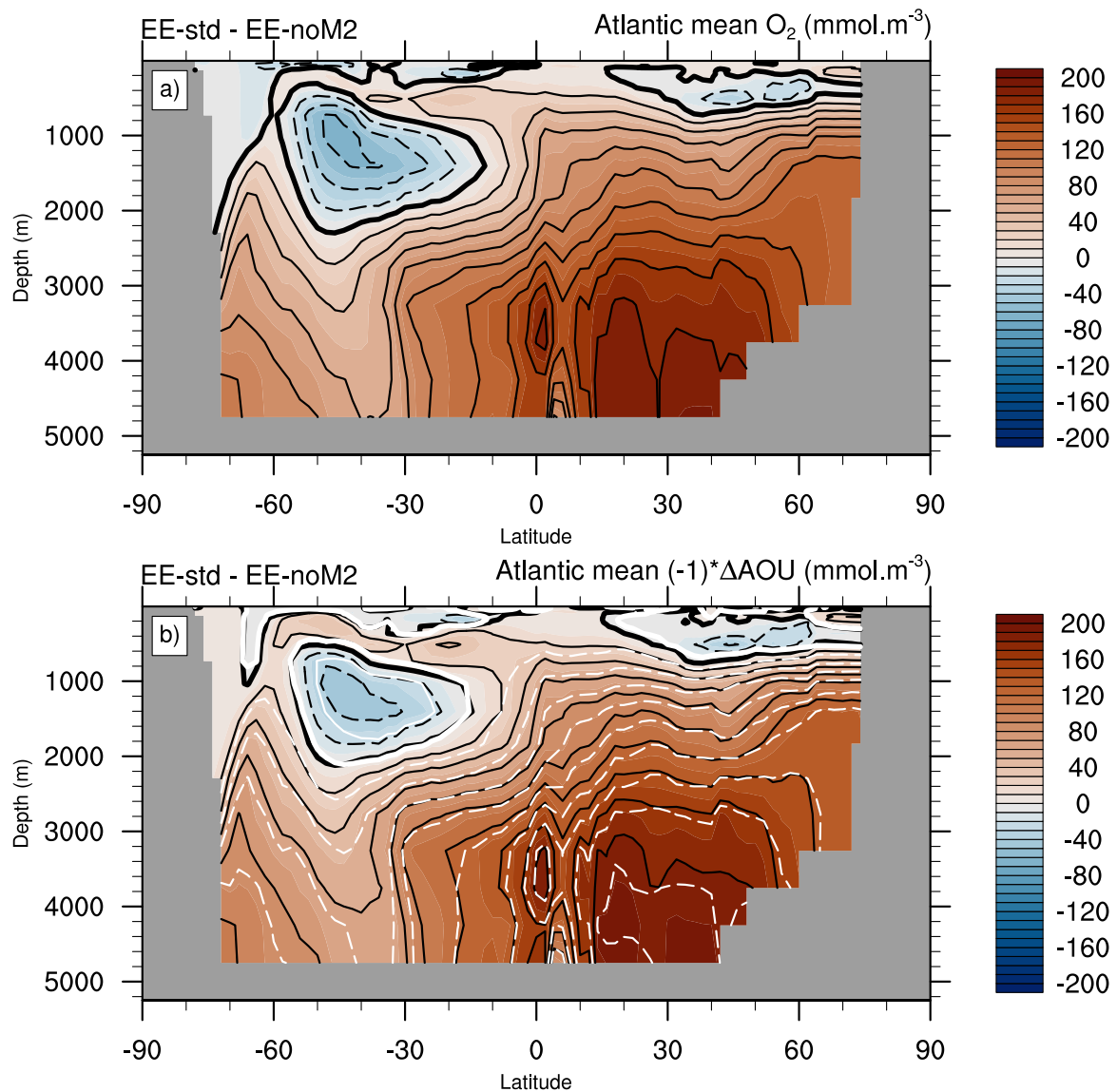


Figure 8. Zonally averaged (a) dissolved oxygen concentration difference (mmol m^{-3}) and (b) AOU difference (mmol m^{-3}) across the Atlantic between EE-std and EE-noM2 (shading and black contours). White contours denote the difference in water age between EE-std and EE-noM2 (positive solid and negative dashed).

758

759

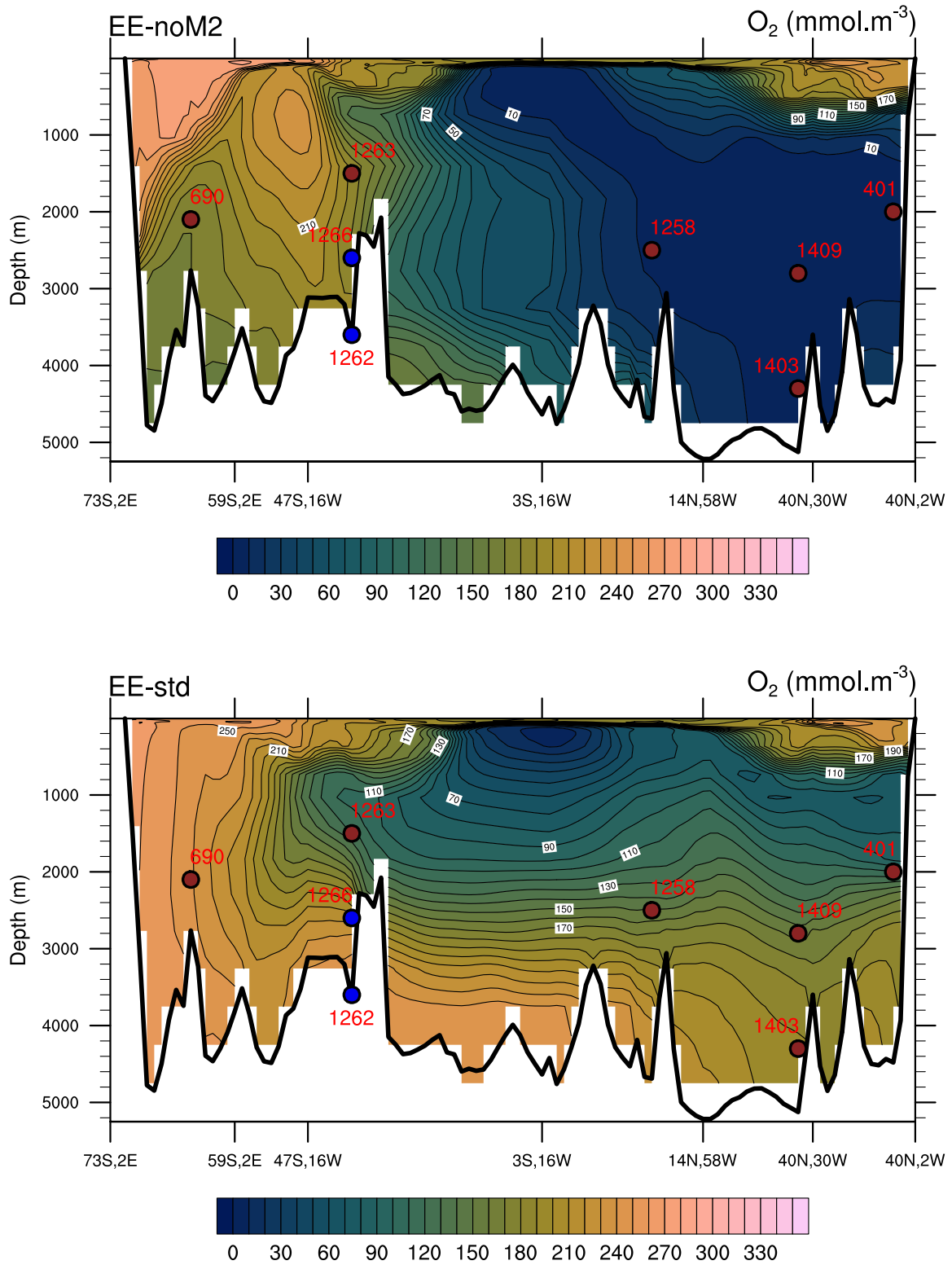


Figure 9. Dissolved oxygen concentration (mmol m^{-3}) transect across the Atlantic for EE-noM2 (a) and EE-std (b). The transect followed is shown on Fig. S3. At the exception of Sites 1262 and 1266 (blue color), for which oxygen-rich conditions have been reported, other Atlantic sites (brownish color) exhibit low oxygen conditions, according to proxy data.

761

762

763 **References**

764

- 765 Aumont, O., Ethé, C., Tagliabue, A., Bopp, L., Gehlen, M., 2015. PISCES-v2: an ocean
766 biogeochemical model for carbon and ecosystem studies. *Geosci. Model Dev.* 8, 2465–2513.
767 <https://doi.org/10.5194/gmd-8-2465-2015>
- 768 Blanke, B., Delecluse, P., 1993. Variability of the tropical Atlantic Ocean simulated by a
769 general circulation model with two different mixed-layer physics. *J. Phys. Oceanogr.* 23,
770 1363–1388. [https://doi.org/10.1175/1520-0485\(1993\)023<1363:VOTTAO>2.0.CO;2](https://doi.org/10.1175/1520-0485(1993)023<1363:VOTTAO>2.0.CO;2)
- 771 Bopp, L., Resplandy, L., Untersee, A., Le Mezo, P., Kageyama, M., 2017. Ocean (de)
772 oxygenation from the Last Glacial Maximum to the twenty-first century: insights from Earth
773 System models. *Philos. Trans. R. Soc. Math. Phys. Eng. Sci.* 375, 20160323.
- 774 Bryan, K., Lewis, L.J., 1979. A water mass model of the World Ocean. *J. Geophys. Res.*
775 *Oceans* 84, 2503–2517. <https://doi.org/10.1029/JC084iC05p02503>
- 776 Carmichael, M.J., Inglis, G.N., Badger, M.P.S., Naafs, B.D.A., Behrooz, L., Remmelzwaal,
777 S., Monteiro, F.M., Rohrsen, M., Farnsworth, A., Buss, H.L., Dickson, A.J., Valdes, P.J.,
778 Lunt, D.J., Pancost, R.D., 2017. Hydrological and associated biogeochemical consequences of
779 rapid global warming during the Paleocene-Eocene Thermal Maximum. *Glob. Planet. Change*
780 157, 114–138. <https://doi.org/10.1016/j.gloplacha.2017.07.014>
- 781 Cimoli, L., Mashayek, A., Johnson, H.L., Marshall, D.P., Naveira Garabato, A.C., Whalen,
782 C.B., Vic, C., De Lavergne, C., Alford, M.H., MacKinnon, J.A., Talley, L.D., 2023.
783 Significance of Diapycnal Mixing Within the Atlantic Meridional Overturning Circulation.
784 *AGU Adv.* 4, e2022AV000800. <https://doi.org/10.1029/2022AV000800>
- 785 Clarkson, M.O., Lenton, T.M., Andersen, M.B., Bagard, M.-L., Dickson, A.J., Vance, D.,
786 2021. Upper limits on the extent of seafloor anoxia during the PETM from uranium isotopes.
787 *Nat. Commun.* 12, 399. <https://doi.org/10.1038/s41467-020-20486-5>
- 788 Crameri, F., Shephard, G.E., Heron, P.J., 2020. The misuse of colour in science
789 communication. *Nat. Commun.* 11, 5444. <https://doi.org/10.1038/s41467-020-19160-7>
- 790 de Lavergne, C., Groeskamp, S., Zika, J., Johnson, H.L., 2022. The role of mixing in the
791 large-scale ocean circulation, in: *Ocean Mixing*. Elsevier, pp. 35–63.
792 <https://doi.org/10.1016/B978-0-12-821512-8.00010-4>
- 793 de Lavergne, C., Madec, G., Roquet, F., Holmes, R.M., McDougall, T.J., 2017. Abyssal
794 ocean overturning shaped by seafloor distribution. *Nature* 551, 181–186.
795 <https://doi.org/10.1038/nature24472>
- 796 de Lavergne, C., Vic, C., Madec, G., Roquet, F., Waterhouse, A.F., Whalen, C.B., Cuypers,
797 Y., Bouruet-Aubertot, P., Ferron, B., Hibiya, T., 2020. A Parameterization of Local and
798 Remote Tidal Mixing. *J. Adv. Model. Earth Syst.* 12, e2020MS002065.
799 <https://doi.org/10.1029/2020MS002065>
- 800 Dickson, A.J., Cohen, A.S., Coe, A.L., 2012. Seawater oxygenation during the Paleocene-
801 Eocene Thermal Maximum. *Geology* 40, 639–642. <https://doi.org/10.1130/G32977.1>
- 802 Dickson, A.J., Rees-Owen, R.L., März, C., Coe, A.L., Cohen, A.S., Pancost, R.D., Taylor, K.,
803 Shcherbinina, E., 2014. The spread of marine anoxia on the northern Tethys margin during
804 the Paleocene-Eocene Thermal Maximum: Tethys redox during the PETM. *Paleoceanography*
805 29, 471–488. <https://doi.org/10.1002/2014PA002629>
- 806 Dunne, J.P., Sarmiento, J.L., Gnanadesikan, A., 2007. A synthesis of global particle export
807 from the surface ocean and cycling through the ocean interior and on the seafloor. *Glob.*
808 *Biogeochem. Cycles* 21, 2006GB002907. <https://doi.org/10.1029/2006GB002907>

809 Egbert, G.D., Ray, R.D., 2000. Significant dissipation of tidal energy in the deep ocean
810 inferred from satellite altimeter data. *Nature* 405, 775–778.

811 Evans, D., Sagoo, N., Renema, W., Cotton, L.J., Müller, W., Todd, J.A., Saraswati, P.K.,
812 Stassen, P., Ziegler, M., Pearson, P.N., Valdes, P.J., Affek, H.P., 2018. Eocene greenhouse
813 climate revealed by coupled clumped isotope-Mg/Ca thermometry. *Proc. Natl. Acad. Sci.*
814 115, 1174–1179. <https://doi.org/10.1073/pnas.1714744115>

815 Fichfet, T., Maqueda, M.A.M., 1997. Sensitivity of a global sea ice model to the treatment of
816 ice thermodynamics and dynamics. *J. Geophys. Res. Oceans* 102, 12609–12646.
817 <https://doi.org/10.1029/97JC00480>

818 Gargett, A.E., 1984. Vertical eddy diffusivity in the ocean interior. *J. Mar. Res.* 42, 359–393.
819 <https://doi.org/10.1357/002224084788502756>

820 Garrett, C., Kunze, E., 2007. Internal Tide Generation in the Deep Ocean. *Annu. Rev. Fluid*
821 *Mech.* 39, 57–87. <https://doi.org/10.1146/annurev.fluid.39.050905.110227>

822 Gaspar, P., Grégoris, Y., Lefevre, J., 1990. A simple eddy kinetic energy model for
823 simulations of the oceanic vertical mixing: Tests at station Papa and long-term upper ocean
824 study site. *J. Geophys. Res. Oceans* 95, 16179–16193.
825 <https://doi.org/10.1029/JC095iC09p16179>

826 Green, J.A.M., Huber, M., 2013. Tidal dissipation in the early Eocene and implications for
827 ocean mixing. *Geophys. Res. Lett.* 40, 2707–2713. <https://doi.org/10.1002/grl.50510>

828 Green, M., Hadley-Pryce, D., Scotese, C., 2023. Phanerozoic (541 Ma-present day), in: *A*
829 *Journey Through Tides*. Elsevier, pp. 157–184.

830 Heinemann, M., Jungclaus, J.H., Marotzke, J., 2009. Warm Paleocene/Eocene climate as
831 simulated in ECHAM5/MPI-OM. *Clim Past* 5, 785–802. [https://doi.org/10.5194/cp-5-785-](https://doi.org/10.5194/cp-5-785-2009)
832 2009

833 Heinze, M., Ilyina, T., 2015. Ocean biogeochemistry in the warm climate of the late
834 Paleocene. *Clim. Past* 11, 63–79. <https://doi.org/10.5194/cp-11-63-2015>

835 Herold, N., Buzan, J., Seton, M., Goldner, A., Green, J.A.M., Müller, R.D., Markwick, P.,
836 Huber, M., 2014. A suite of early Eocene (~ 55 Ma) climate model boundary conditions.
837 *Geosci. Model Dev.* 7, 2077–2090. <https://doi.org/10.5194/gmd-7-2077-2014>

838 Holmes, R.M., Zika, J.D., Griffies, S.M., Hogg, A.McC., Kiss, A.E., England, M.H., 2021.
839 The Geography of Numerical Mixing in a Suite of Global Ocean Models. *J. Adv. Model.*
840 *Earth Syst.* 13, e2020MS002333. <https://doi.org/10.1029/2020MS002333>

841 Hourdin, F., Foujols, M.-A., Codron, F., Guemas, V., Dufresne, J.-L., Bony, S., Denvil, S.,
842 Guez, L., Lott, F., Ghattas, J., Braconnot, P., Marti, O., Meurdesoif, Y., Bopp, L., 2013.
843 Impact of the LMDZ atmospheric grid configuration on the climate and sensitivity of the
844 IPSL-CM5A coupled model. *Clim. Dyn.* 40, 2167–2192. [https://doi.org/10.1007/s00382-012-](https://doi.org/10.1007/s00382-012-845)
845 1411-3

846 Huber, M., Caballero, R., 2011. The early Eocene equable climate problem revisited. *Clim.*
847 *Past* 7, 603–633. <https://doi.org/10.5194/cp-7-603-2011>

848 Hutchinson, D.K., De Boer, A.M., Coxall, H.K., Caballero, R., Nilsson, J., Baatsen, M., 2018.
849 Climate sensitivity and meridional overturning circulation in the late Eocene using GFDL
850 CM2.1. *Clim. Past* 14, 789–810. <https://doi.org/10.5194/cp-14-789-2018>

851 Ilyina, T., Heinze, M., 2019. Carbonate Dissolution Enhanced by Ocean Stagnation and
852 Respiration at the Onset of the Paleocene-Eocene Thermal Maximum. *Geophys. Res. Lett.* 46,
853 842–852. <https://doi.org/10.1029/2018GL080761>

854 Jayne, S.R., 2009. The Impact of Abyssal Mixing Parameterizations in an Ocean General
855 Circulation Model. *J. Phys. Oceanogr.* 39, 1756–1775.
856 <https://doi.org/10.1175/2009JPO4085.1>

857 Krinner, G., Viovy, N., De Noblet-Ducoudré, N., Ogée, J., Polcher, J., Friedlingstein, P.,
858 Ciais, P., Sitch, S., Prentice, I.C., 2005. A dynamic global vegetation model for studies of the

859 coupled atmosphere-biosphere system. *Glob. Biogeochem. Cycles* 19, 2003GB002199.
860 <https://doi.org/10.1029/2003GB002199>

861 Laugié, M., Donnadieu, Y., Ladant, J., Bopp, L., Ethé, C., Raison, F., 2021. Exploring the
862 Impact of Cenomanian Paleogeography and Marine Gateways on Oceanic Oxygen.
863 *Paleoceanogr. Paleoclimatology* 36, e2020PA004202. <https://doi.org/10.1029/2020PA004202>

864 Lazar, A., Madec, G., Delecluse, P., 1999. The Deep Interior Downwelling, the Veronis
865 Effect, and Mesoscale Tracer Transport Parameterizations in an OGCM. *J. Phys. Oceanogr.*
866 29, 2945–2961. [https://doi.org/10.1175/1520-0485\(1999\)029<2945:TDIDTV>2.0.CO;2](https://doi.org/10.1175/1520-0485(1999)029<2945:TDIDTV>2.0.CO;2)

867 Liu, Z., Pagani, M., Zinniker, D., DeConto, R., Huber, M., Brinkhuis, H., Shah, S.R., Leckie,
868 R.M., Pearson, A., 2009. Global cooling during the Eocene-Oligocene Climate Transition.
869 *Science* 323, 1187–1190.

870 Lu, W., Rickaby, R.E.M., Hoogakker, B.A.A., Rathburn, A.E., Burkett, A.M., Dickson, A.J.,
871 Martínez-Méndez, G., Hillenbrand, C.-D., Zhou, X., Thomas, E., Lu, Z., 2020. I/Ca in
872 epifaunal benthic foraminifera: A semi-quantitative proxy for bottom water oxygen in a multi-
873 proxy compilation for glacial ocean deoxygenation. *Earth Planet. Sci. Lett.* 533, 116055.
874 <https://doi.org/10.1016/j.epsl.2019.116055>

875 Lunt, D.J., Bragg, F., Chan, W.-L., Hutchinson, D.K., Ladant, J.-B., Morozova, P.,
876 Niezgodzki, I., Steinig, S., Zhang, Z., Zhu, J., Abe-Ouchi, A., Anagnostou, E., De Boer,
877 A.M., Coxall, H.K., Donnadieu, Y., Foster, G., Inglis, G.N., Knorr, G., Langebroek, P.M.,
878 Lear, C.H., Lohmann, G., Poulsen, C.J., Sepulchre, P., Tierney, J.E., Valdes, P.J., Volodin,
879 E.M., Dunkley Jones, T., Hollis, C.J., Huber, M., Otto-Bliesner, B.L., 2021. DeepMIP: model
880 intercomparison of early Eocene climatic optimum (EECO) large-scale climate features and
881 comparison with proxy data. *Clim. Past* 17, 203–227. <https://doi.org/10.5194/cp-17-203-2021>

882 Lunt, D.J., Huber, M., Anagnostou, E., Baatsen, M.L.J., Caballero, R., DeConto, R., Dijkstra,
883 H.A., Donnadieu, Y., Evans, D., Feng, R., Foster, G.L., Gasson, E., Von Der Heydt, A.S.,
884 Hollis, C.J., Inglis, G.N., Jones, S.M., Kiehl, J., Kirtland Turner, S., Korty, R.L., Kozdon, R.,
885 Krishnan, S., Ladant, J.-B., Langebroek, P., Lear, C.H., LeGrande, A.N., Littler, K.,
886 Markwick, P., Otto-Bliesner, B., Pearson, P., Poulsen, C.J., Salzmann, U., Shields, C., Snell,
887 K., Stärz, M., Super, J., Tabor, C., Tierney, J.E., Tourte, G.J.L., Tripathi, A., Upchurch, G.R.,
888 Wade, B.S., Wing, S.L., Winguth, A.M.E., Wright, N.M., Zachos, J.C., Zeebe, R.E., 2017.
889 The DeepMIP contribution to PMIP4: experimental design for model simulations of the
890 EECO, PETM, and pre-PETM (version 1.0). *Geosci. Model Dev.* 10, 889–901.
891 <https://doi.org/10.5194/gmd-10-889-2017>

892 MacKinnon, J.A., Zhao, Z., Whalen, C.B., Waterhouse, A.F., Trossman, D.S., Sun, O.M., St.
893 Laurent, L.C., Simmons, H.L., Polzin, K., Pinkel, R., Pickering, A., Norton, N.J., Nash, J.D.,
894 Musgrave, R., Merchant, L.M., Melet, A.V., Mater, B., Legg, S., Large, W.G., Kunze, E.,
895 Klymak, J.M., Jochum, M., Jayne, S.R., Hallberg, R.W., Griffies, S.M., Diggs, S.,
896 Danabasoglu, G., Chassignet, E.P., Buijsman, M.C., Bryan, F.O., Briegleb, B.P., Barna, A.,
897 Arbic, B.K., Ansong, J.K., Alford, M.H., 2017. Climate Process Team on Internal Wave–
898 Driven Ocean Mixing. *Bull. Am. Meteorol. Soc.* 98, 2429–2454.
899 <https://doi.org/10.1175/BAMS-D-16-0030.1>

900 Madec, G., Imbard, M., 1996. A global ocean mesh to overcome the North Pole singularity.
901 *Clim. Dyn.* 12, 381–388.

902 Madec, G., the NEMO team, 2016. NEMO ocean engine. *Notes Pô Modélisation Inst. Pierre-*
903 *Simon Laplace* 27, ISSN No 1288-1619.

904 Marshall, J., Speer, K., 2012. Closure of the meridional overturning circulation through
905 Southern Ocean upwelling. *Nat. Geosci.* 5, 171–180. <https://doi.org/10.1038/ngeo1391>

906 Meissner, K.J., Bralower, T.J., Alexander, K., Jones, T.D., Sijp, W., Ward, M., 2014. The
907 Paleocene-Eocene Thermal Maximum: How much carbon is enough? *Paleoceanography* 29,
908 946–963. <https://doi.org/10.1002/2014PA002650>

909 Melet, A., Legg, S., Hallberg, R., 2016. Climatic Impacts of Parameterized Local and Remote
910 Tidal Mixing. *J. Clim.* 29, 3473–3500. <https://doi.org/10.1175/JCLI-D-15-0153.1>

911 Melet, A.V., Hallberg, R., Marshall, D.P., 2022. The role of ocean mixing in the climate
912 system, in: *Ocean Mixing*. Elsevier, pp. 5–34. [https://doi.org/10.1016/B978-0-12-821512-](https://doi.org/10.1016/B978-0-12-821512-8.00009-8)
913 [8.00009-8](https://doi.org/10.1016/B978-0-12-821512-8.00009-8)

914 Merryfield, W.J., Holloway, G., Gargett, A.E., 1999. A Global Ocean Model with Double-
915 Diffusive Mixing. *J. Phys. Oceanogr.* 29, 1124–1142. [https://doi.org/10.1175/1520-](https://doi.org/10.1175/1520-0485(1999)029<1124:AGOMWD>2.0.CO;2)
916 [0485\(1999\)029<1124:AGOMWD>2.0.CO;2](https://doi.org/10.1175/1520-0485(1999)029<1124:AGOMWD>2.0.CO;2)

917 Meurdesoif, Y., Caubel, A., Lacroix, R., Déroutillat, J., Nguyen, M.H., 2016. XIOS tutorial.
918 [Httpforgeipsl.jussieu.fr/ioserver/attach.-Tutorialpdf](http://forgeipsl.jussieu.fr/ioserver/attach/tutorial.pdf).

919 Middelburg, J.J., Soetaert, K., Herman, P.M.J., Heip, C.H.R., 1996. Denitrification in marine
920 sediments: A model study. *Glob. Biogeochem. Cycles* 10, 661–673.
921 <https://doi.org/10.1029/96GB02562>

922 Munk, W., Wunsch, C., 1998. Abyssal recipes II: Energetics of tidal and wind mixing. *Deep*
923 *Sea Res.* 45, 1977–2010.

924 Munk, W.H., 1966. Abyssal recipes. *Deep Sea Res.* 13, 707–730.

925 Pälike, C., Delaney, M.L., Zachos, J.C., 2014. Deep-sea redox across the Paleocene-Eocene
926 thermal maximum. *Geochem. Geophys. Geosystems* 15, 1038–1053.
927 <https://doi.org/10.1002/2013GC005074>

928 Saenko, O.A., 2006. The Effect of Localized Mixing on the Ocean Circulation and Time-
929 Dependent Climate Change. *J. Phys. Oceanogr.* 36, 140–160.
930 <https://doi.org/10.1175/JPO2839.1>

931 Saenko, O.A., Merryfield, W.J., 2005. On the Effect of Topographically Enhanced Mixing on
932 the Global Ocean Circulation. *J. Phys. Oceanogr.* 35, 826–834.
933 <https://doi.org/10.1175/JPO2722.1>

934 Schmittner, A., Egbert, G.D., 2014. An improved parameterization of tidal mixing for ocean
935 models. *Geosci. Model Dev.* 7, 211–224. <https://doi.org/10.5194/gmd-7-211-2014>

936 Schmittner, A., Green, J.A.M., Wilmes, S. -B., 2015. Glacial ocean overturning intensified by
937 tidal mixing in a global circulation model. *Geophys. Res. Lett.* 42, 4014–4022.
938 <https://doi.org/10.1002/2015GL063561>

939 Sepulchre, P., Caubel, A., Ladant, J.-B., Bopp, L., Boucher, O., Braconnot, P., Brockmann,
940 P., Cozic, A., Donnadiou, Y., Dufresne, J.-L., Estella-Perez, V., Ethé, C., Fluteau, F., Foujols,
941 M.-A., Gastineau, G., Ghattas, J., Hauglustaine, D., Hourdin, F., Kageyama, M., Khodri, M.,
942 Marti, O., Meurdesoif, Y., Mignot, J., Sarr, A.-C., Servonnat, J., Swingedouw, D., Szopa, S.,
943 Tardif, D., 2020. IPSL-CM5A2 – an Earth system model designed for multi-millennial
944 climate simulations. *Geosci. Model Dev.* 13, 3011–3053. [https://doi.org/10.5194/gmd-13-](https://doi.org/10.5194/gmd-13-3011-2020)
945 [3011-2020](https://doi.org/10.5194/gmd-13-3011-2020)

946 Sharoni, S., Halevy, I., 2023. Rates of seafloor and continental weathering govern
947 Phanerozoic marine phosphate levels. *Nat. Geosci.* 16, 75–81. [https://doi.org/10.1038/s41561-](https://doi.org/10.1038/s41561-022-01075-1)
948 [022-01075-1](https://doi.org/10.1038/s41561-022-01075-1)

949 Simmons, H.L., Jayne, S.R., Laurent, L.C.St., Weaver, A.J., 2004. Tidally driven mixing in a
950 numerical model of the ocean general circulation. *Ocean Model.* 6, 245–263.
951 [https://doi.org/10.1016/S1463-5003\(03\)00011-8](https://doi.org/10.1016/S1463-5003(03)00011-8)

952 Song, P., Sidorenko, D., Scholz, P., Thomas, M., Lohmann, G., 2023. The tidal effects in the
953 Finite-volume Sea ice–Ocean Model (FESOM2.1): a comparison between parameterised tidal
954 mixing and explicit tidal forcing. *Geosci. Model Dev.* 16, 383–405.
955 <https://doi.org/10.5194/gmd-16-383-2023>

956 St. Laurent, L., Garrett, C., 2002. The Role of Internal Tides in Mixing the Deep Ocean. *J.*
957 *Phys. Oceanogr.* 32, 2882–2899. [https://doi.org/10.1175/1520-](https://doi.org/10.1175/1520-0485(2002)032<2882:TROITI>2.0.CO;2)
958 [0485\(2002\)032<2882:TROITI>2.0.CO;2](https://doi.org/10.1175/1520-0485(2002)032<2882:TROITI>2.0.CO;2)

959 Talley, L., 2013. Closure of the Global Overturning Circulation Through the Indian, Pacific,
960 and Southern Oceans: Schematics and Transports. *Oceanography* 26, 80–97.
961 <https://doi.org/10.5670/oceanog.2013.07>

962 Thomas, D.J., Korty, R., Huber, M., Schubert, J.A., Haines, B., 2014. Nd isotopic structure of
963 the Pacific Ocean 70–30 Ma and numerical evidence for vigorous ocean circulation and ocean
964 heat transport in a greenhouse world. *Paleoceanography* 29, 454–469.
965 <https://doi.org/10.1002/2013PA002535>

966 Toggweiler, J.R., Samuels, B., 1998. On the Ocean’s Large-Scale Circulation near the Limit
967 of No Vertical Mixing. *J. Phys. Oceanogr.* 28, 1832–1852. [https://doi.org/10.1175/1520-0485\(1998\)028<1832:OTOSLS>2.0.CO;2](https://doi.org/10.1175/1520-0485(1998)028<1832:OTOSLS>2.0.CO;2)

969 Toggweiler, J.R., Samuels, B., 1995. Effect of Drake passage on the global thermohaline
970 circulation. *Deep Sea Res. Part Oceanogr. Res. Pap.* 42, 477–500.
971 [https://doi.org/10.1016/0967-0637\(95\)00012-U](https://doi.org/10.1016/0967-0637(95)00012-U)

972 Valcke, S., 2013. The OASIS3 coupler: a European climate modelling community software.
973 *Geosci. Model Dev.* 6, 373–388. <https://doi.org/10.5194/gmd-6-373-2013>

974 Vic, C., Naveira Garabato, A.C., Green, J.A.M., Waterhouse, A.F., Zhao, Z., Melet, A., De
975 Lavergne, C., Buijsman, M.C., Stephenson, G.R., 2019. Deep-ocean mixing driven by small-
976 scale internal tides. *Nat. Commun.* 10, 2099. <https://doi.org/10.1038/s41467-019-10149-5>

977 Wanninkhof, R., 1992. Relationship between wind speed and gas exchange over the ocean. *J.*
978 *Geophys. Res. Oceans* 97, 7373–7382. <https://doi.org/10.1029/92JC00188>

979 Weber, T., Thomas, M., 2017. Influence of ocean tides on the general ocean circulation in the
980 early Eocene. *Paleoceanography* 32, 553–570. <https://doi.org/10.1002/2016PA002997>

981 Whalen, C.B., de Lavergne, C., Naveira Garabato, A.C., Klymak, J.M., MacKinnon, J.A.,
982 Sheen, K.L., 2020. Internal wave-driven mixing: governing processes and consequences for
983 climate. *Nat. Rev. Earth Environ.* 1, 606–621. <https://doi.org/10.1038/s43017-020-0097-z>

984 Whitehead, J.A., 1998. Topographic control of oceanic flows in deep passages and straits.
985 *Rev. Geophys.* 36, 423–440. <https://doi.org/10.1029/98RG01014>

986 Wilmes, S.-B., Green, J.A.M., Schmittner, A., 2021. Enhanced vertical mixing in the glacial
987 ocean inferred from sedimentary carbon isotopes. *Commun. Earth Environ.* 2, 166.
988 <https://doi.org/10.1038/s43247-021-00239-y>

989 Winguth, A.M.E., Thomas, E., Winguth, C., 2012. Global decline in ocean ventilation,
990 oxygenation, and productivity during the Paleocene-Eocene Thermal Maximum: Implications
991 for the benthic extinction. *Geology* 40, 263–266. <https://doi.org/10.1130/G32529.1>

992 Xue, P., Chang, L., Dickens, G.R., Thomas, E., 2022. A Depth-Transect of Ocean
993 Deoxygenation During the Paleocene-Eocene Thermal Maximum: Magnetofossils in
994 Sediment Cores From the Southeast Atlantic. *J. Geophys. Res. Solid Earth* 127,
995 e2022JB024714. <https://doi.org/10.1029/2022JB024714>

996 Xue, P., Chang, L., Thomas, E., 2023. Abrupt Northwest Atlantic deep-sea oxygenation
997 decline preceded the Palaeocene-Eocene Thermal Maximum. *Earth Planet. Sci. Lett.* 618,
998 118304. <https://doi.org/10.1016/j.epsl.2023.118304>

999 Yao, W., Paytan, A., Wortmann, U.G., 2018. Large-scale ocean deoxygenation during the
1000 Paleocene-Eocene Thermal Maximum. *Science* 361, 804–806.
1001 <https://doi.org/10.1126/science.aar8658>

1002 Zhang, Y., De Boer, A.M., Lunt, D.J., Hutchinson, D.K., Ross, P., Van De Flierdt, T., Sexton,
1003 P., Coxall, H.K., Steinig, S., Ladant, J., Zhu, J., Donnadieu, Y., Zhang, Z., Chan, W., Abe-
1004 Ouchi, A., Niezgodzki, I., Lohmann, G., Knorr, G., Poulsen, C.J., Huber, M., 2022. Early
1005 Eocene Ocean Meridional Overturning Circulation: The Roles of Atmospheric Forcing and
1006 Strait Geometry. *Paleoceanogr. Paleoclimatology* 37, e2021PA004329.
1007 <https://doi.org/10.1029/2021PA004329>

1008 Zhang, Y., Huck, T., Lique, C., Donnadieu, Y., Ladant, J.-B., Rabineau, M., Aslanian, D.,

1009 2020. Early Eocene vigorous ocean overturning and its contribution to a warm Southern
1010 Ocean. *Clim. Past* 16, 1263–1283. <https://doi.org/10.5194/cp-16-1263-2020>
1011 Zhou, X., Thomas, E., Rickaby, R.E.M., Winguth, A.M.E., Lu, Z., 2014. I/Ca evidence for
1012 upper ocean deoxygenation during the PETM. *Paleoceanography* 29, 964–975.
1013 <https://doi.org/10.1002/2014PA002702>
1014 Zhou, X., Thomas, E., Winguth, A.M.E., Ridgwell, A., Scher, H., Hoogakker, B.A.A.,
1015 Rickaby, R.E.M., Lu, Z., 2016. Expanded oxygen minimum zones during the late Paleocene-
1016 early Eocene: Hints from multiproxy comparison and ocean modeling. *Paleoceanography* 31,
1017 1532–1546. <https://doi.org/10.1002/2016PA003020>
1018

Supplementary Figures for Biogeochemical impacts of tidally driven internal mixing in the Early Eocene

Jean-Baptiste Ladant¹, Jeanne Millot-Weil^{1,*}, Casimir de Lavergne², Mattias Green³,
Sébastien Nguyen¹, Yannick Donnadieu⁴

¹LSCE

²LOCEAN

³Bangor University

⁴CEREGE

Figures S1 – S12.

References.

M2 tidal dissipation

$\log_{10}(\text{W}\cdot\text{m}^{-2})$

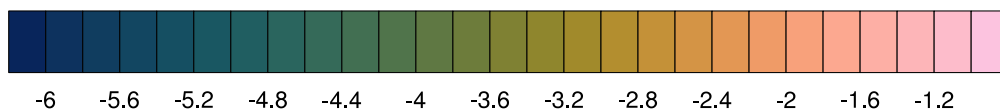
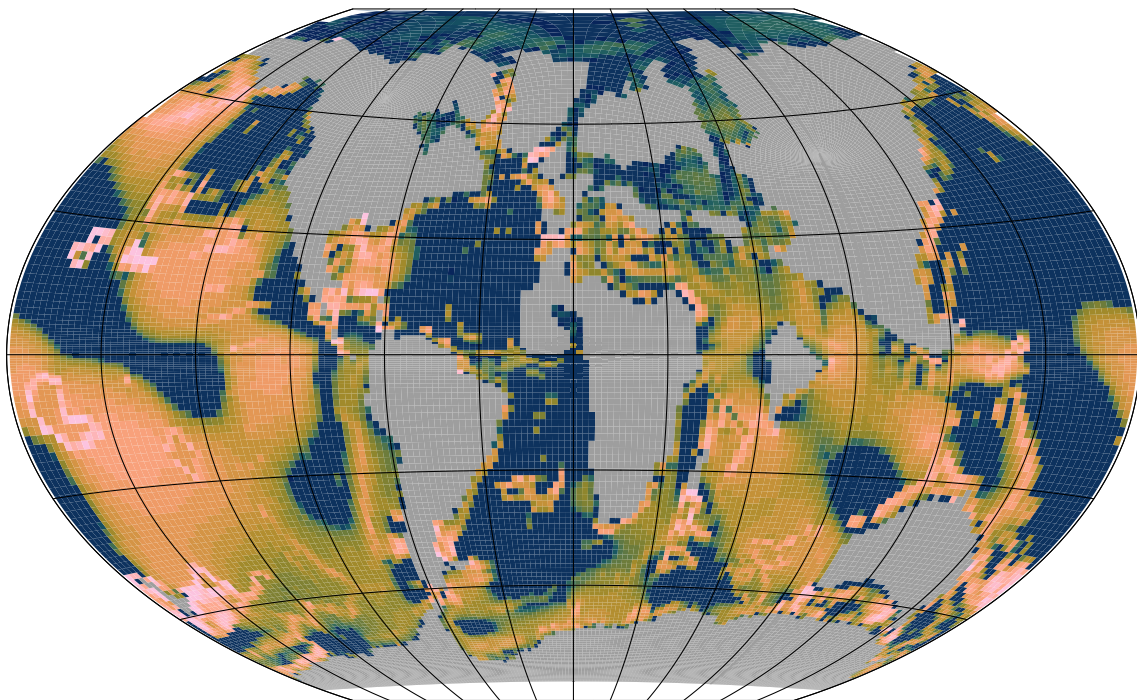


Figure S1. Early Eocene M2 tide dissipation rates from Green and Huber (2013) at model resolution.

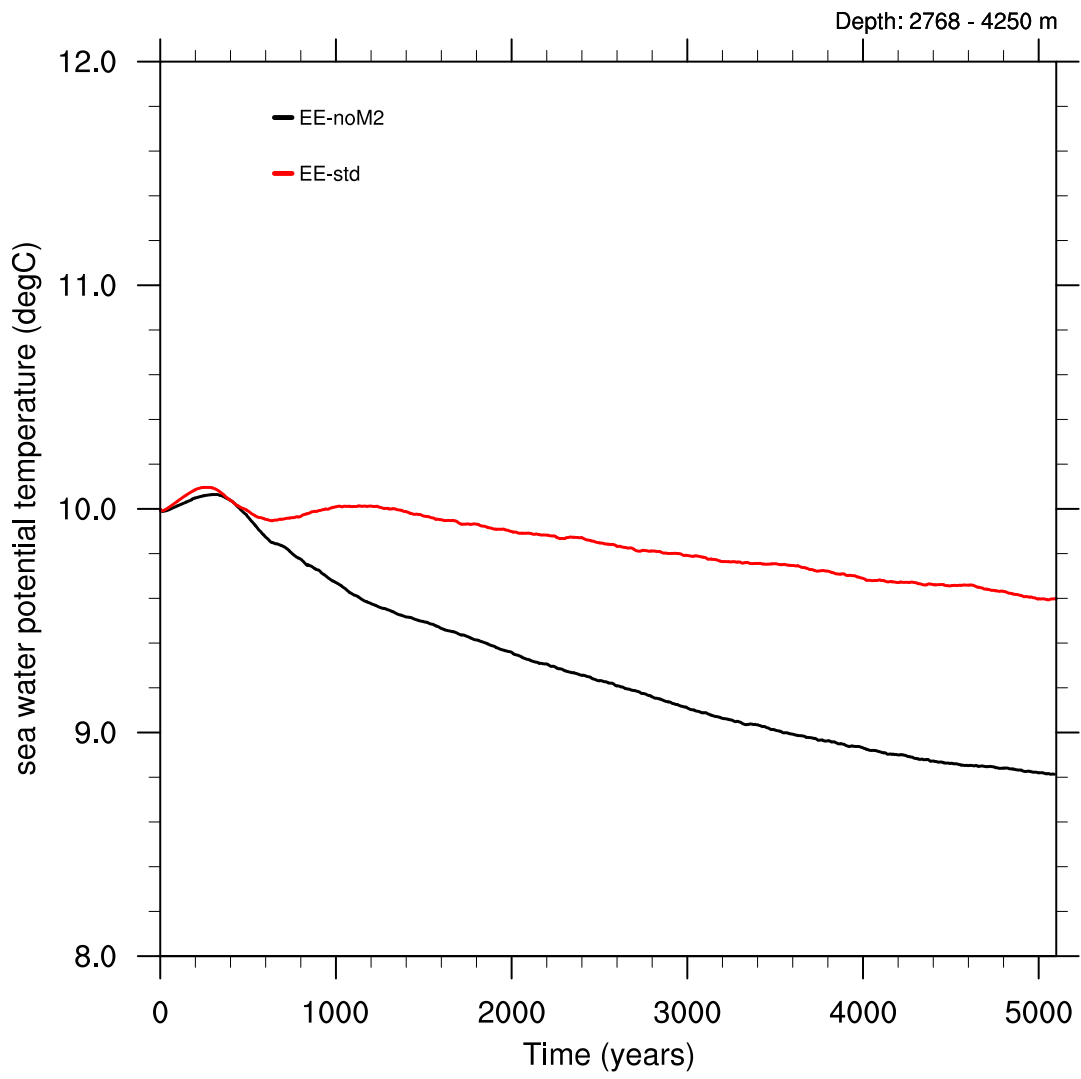


Figure S2. Timeseries of deep ocean temperatures for EE-noM2 (black) and EE-std (red).

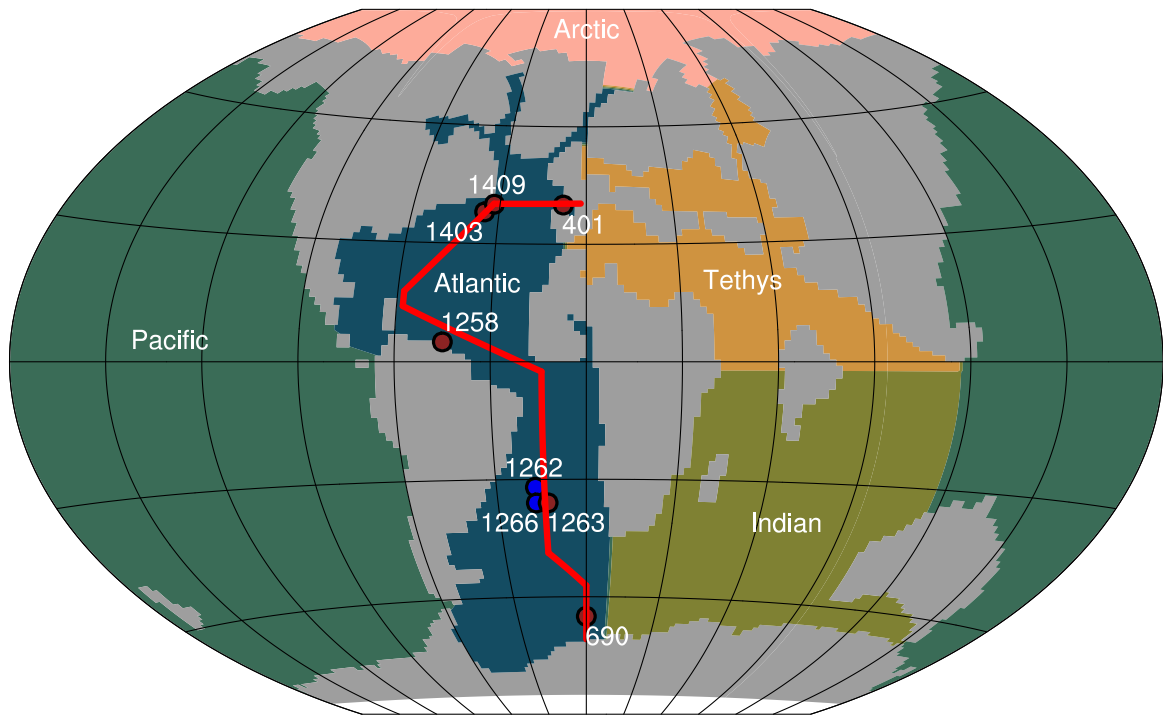


Figure S3. Ocean basins in the Early Eocene. The red contour is the Atlantic transect used in Figure 9. The locations of relevant sites are shown as well: ODP Site 690 (Zhou et al. 2014), ODP Sites 1262, 1263 and 1266 (Pälike et al. 2014, Zhou et al. 2014, Xue et al. 2022), ODP Site 1258 (Pälike et al. 2014), IODP Site 1403 and 1409 (Xue et al. 2023) and DSDP Site 401 (Pälike et al. 2014).

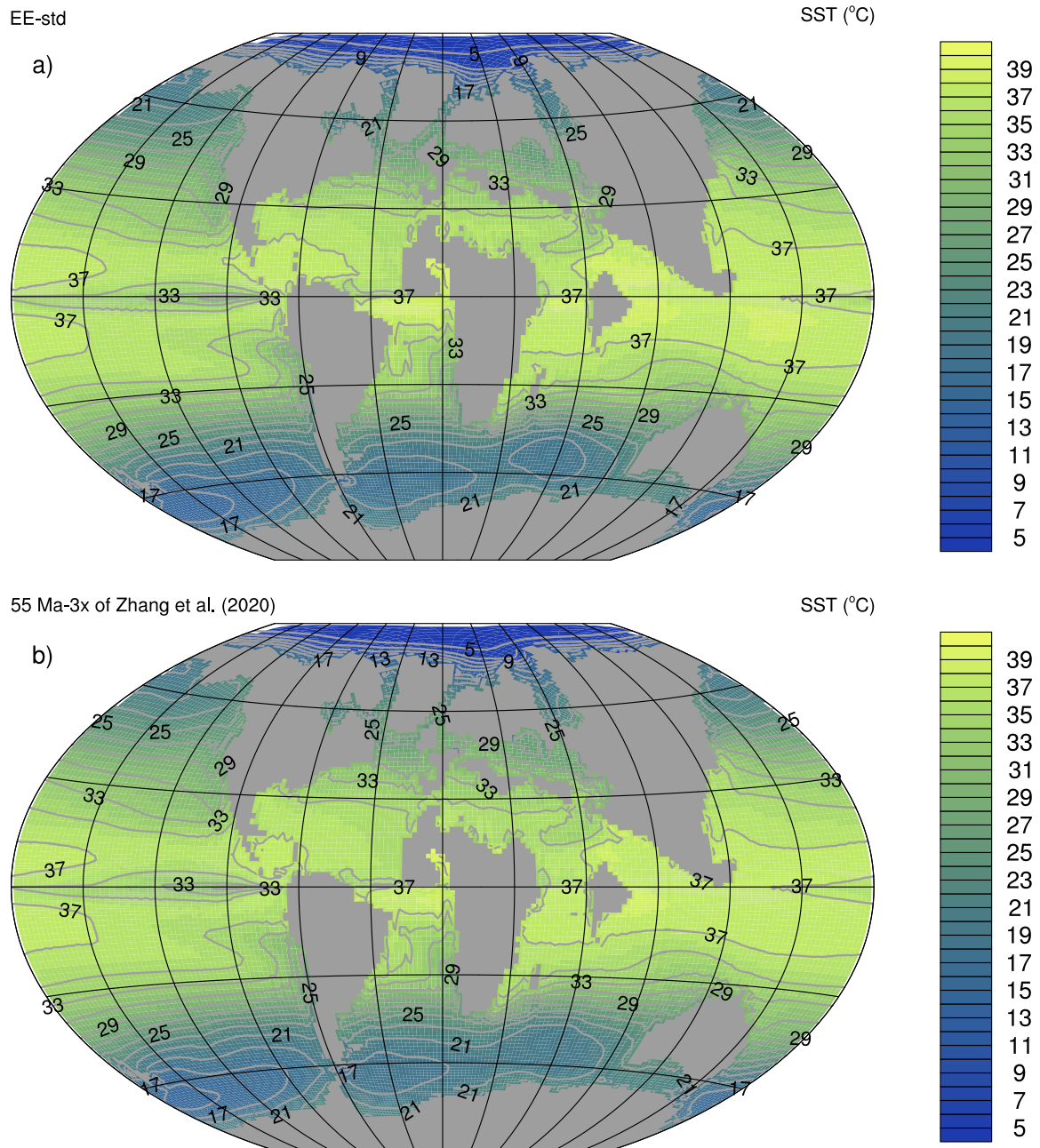


Figure S4. Summer sea surface temperature (°C) in (a) EE-std and (b) the 55 Ma-3x simulation of Zhang et al. (2020). We show summer SST, rather than annual mean, because this is what is presented on Fig. 2a of Zhang et al. (2020)(in contrast to what the legend of the figure reads in Zhang et al. (2020)).

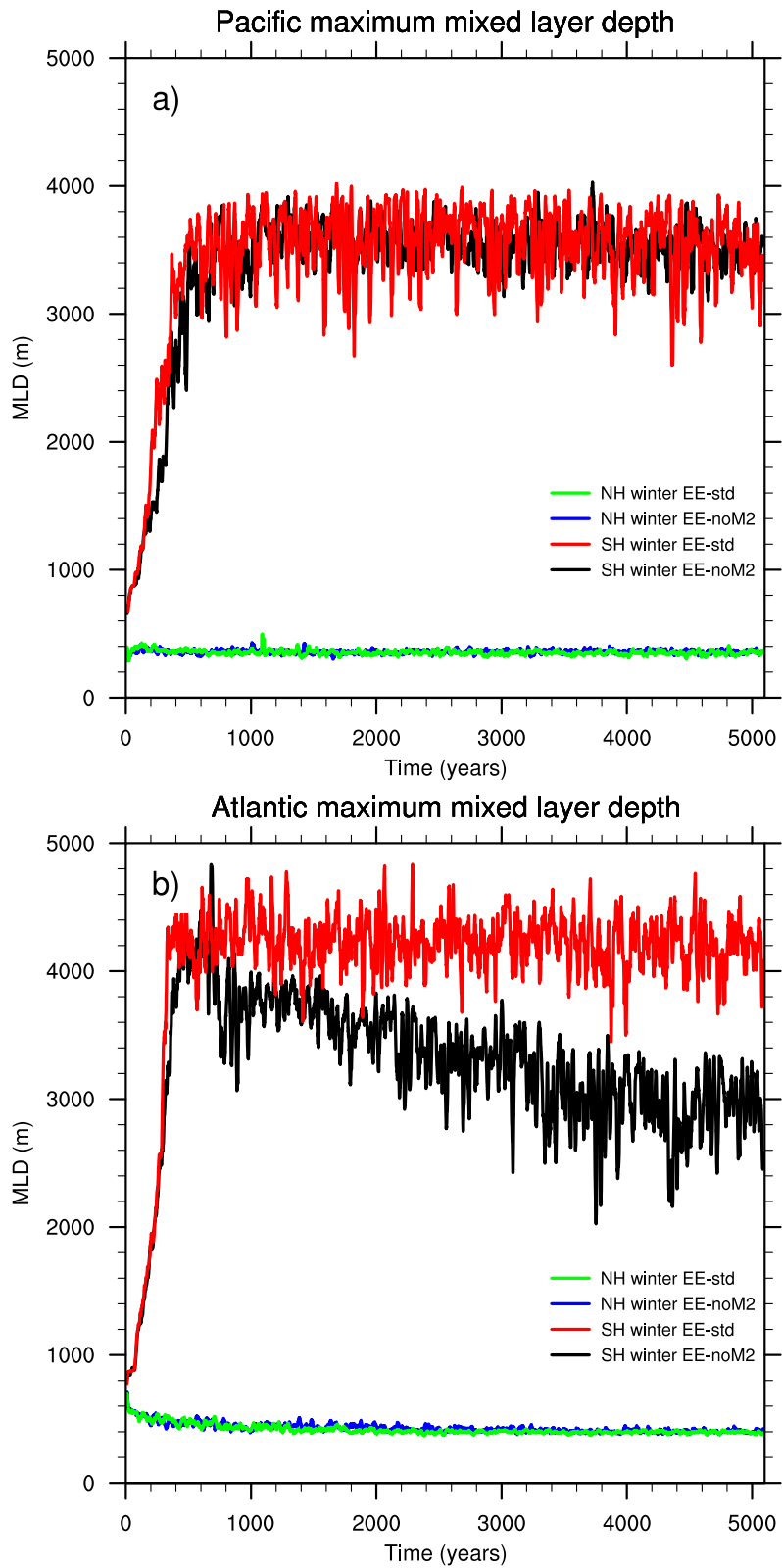


Figure S5. Timeseries of maximum winter mixed-layer depths (m) in the Atlantic and Pacific basin (Fig. S3). Black and red lines represent Southern Hemisphere MLD in EE-noM2 and EE-std respectively. Blue and green lines represent Northern Hemisphere MLD in EE-noM2 and EE-std respectively.

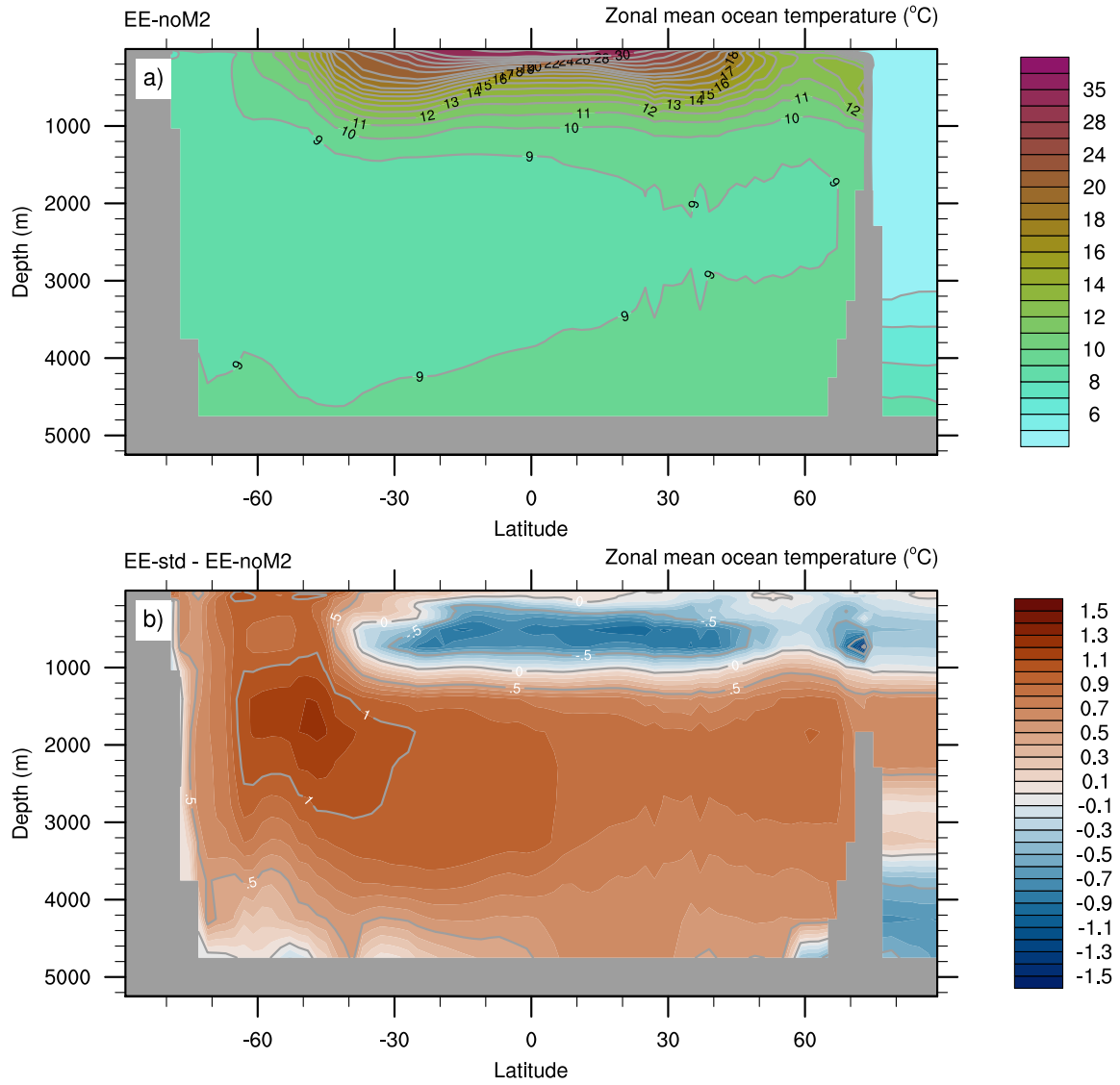


Figure S6. (a) Global zonal mean ocean temperature (°C) in EE-noM2. (b) Global zonal mean ocean temperature difference (°C) in EE-std relative to EE-noM2.

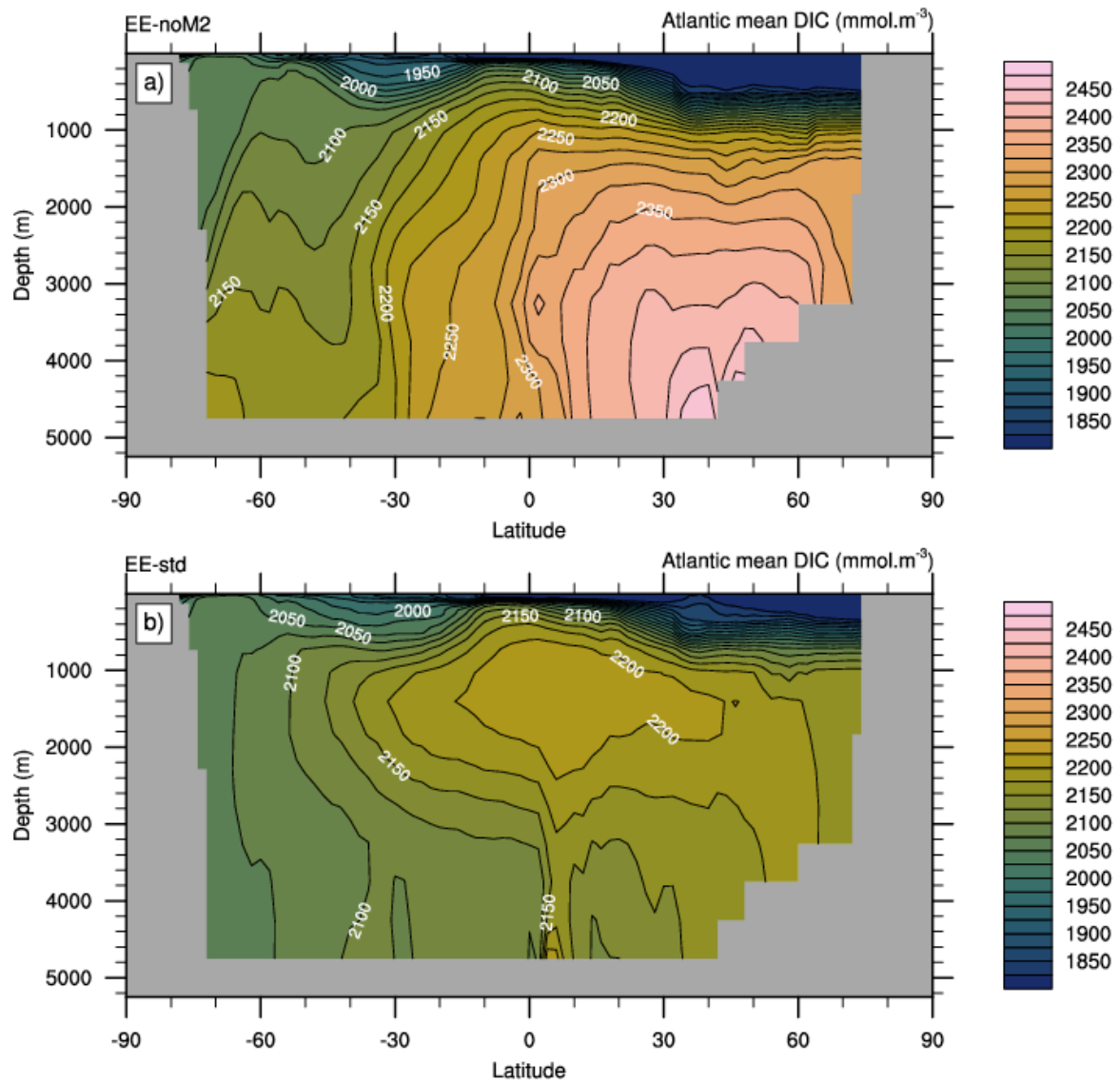


Figure S7. Zonally-averaged dissolved inorganic carbon concentrations (mmol.m^{-3}) across the Atlantic in EE-noM2 (a) and EE-std (b).

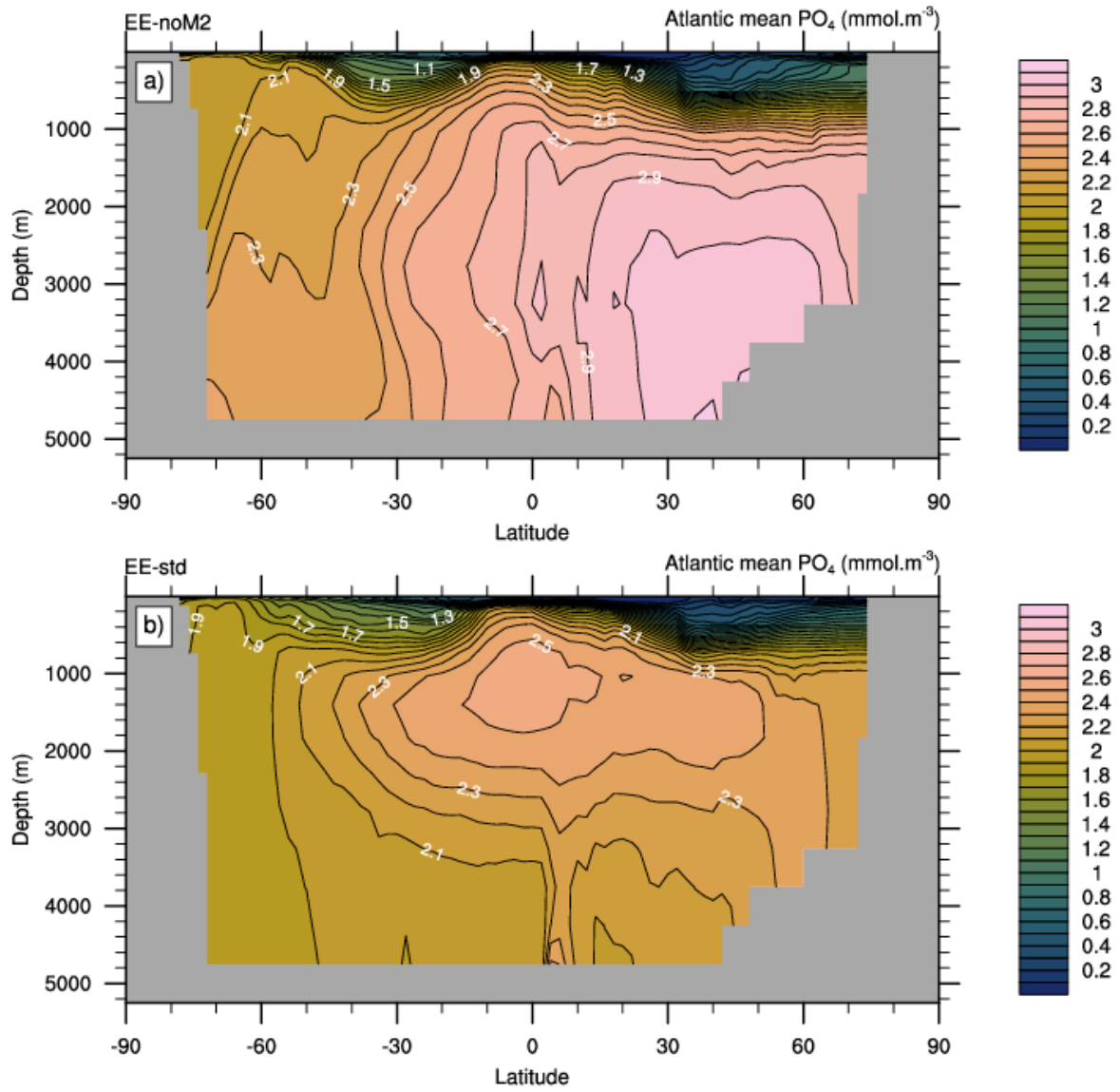


Figure S8. Zonally-averaged phosphate concentrations (mmol.m^{-3}) across the Atlantic in EE-noM2 (a) and EE-std (b).

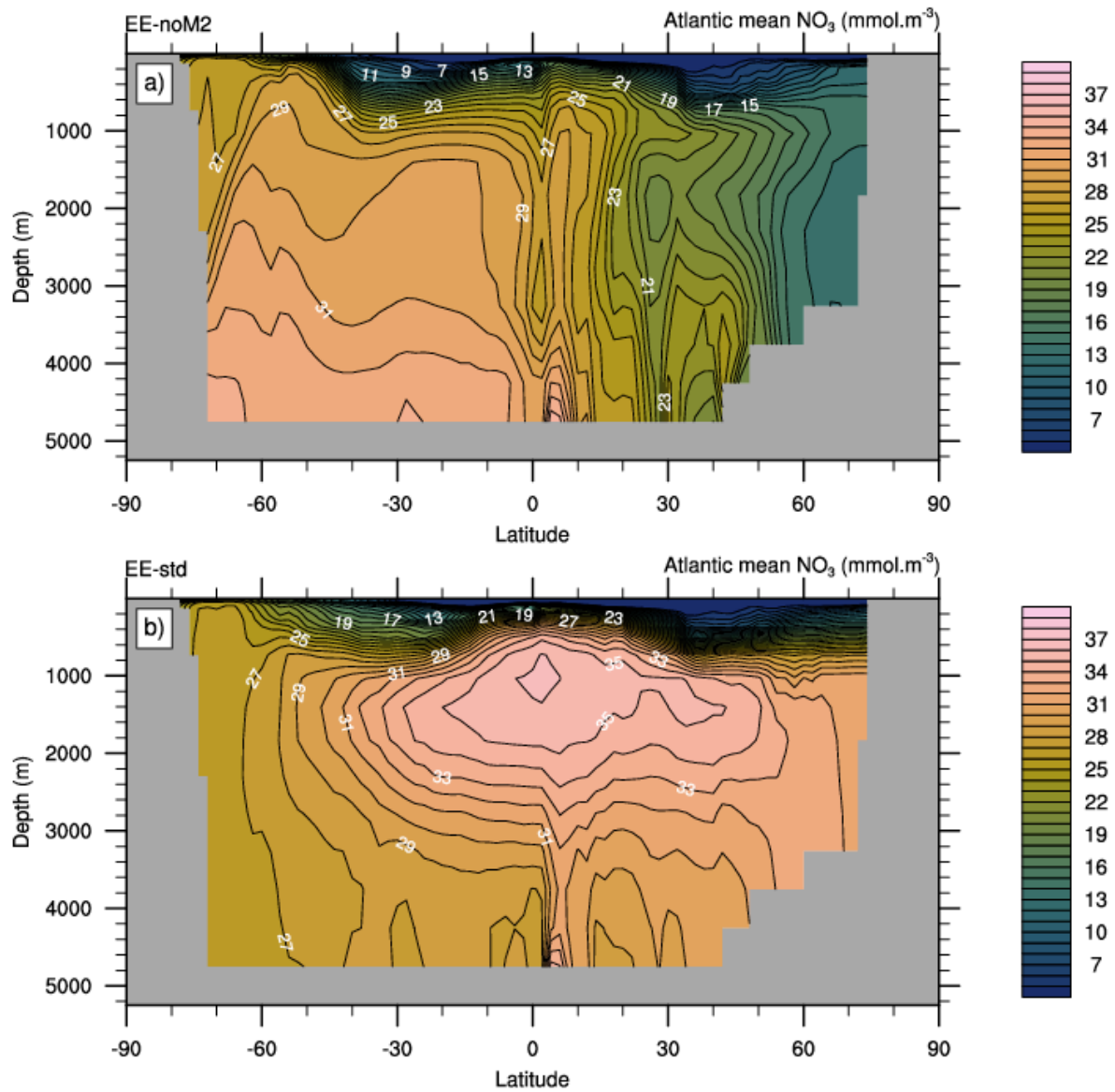


Figure S9. Zonally-averaged nitrate concentrations (mmol.m^{-3}) across the Atlantic in EE-noM2 (a) and EE-std (b).

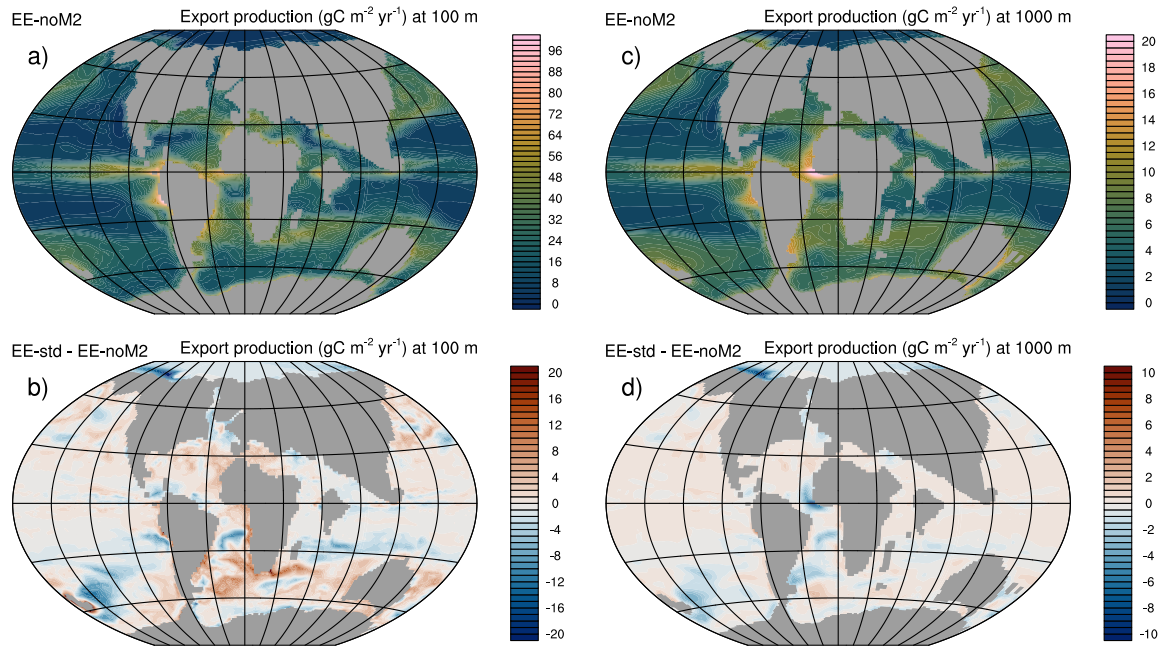


Figure S10. Export production ($\text{gC m}^{-2} \text{yr}^{-1}$) at 100 m (a) and 1000 m (c) in EE-noM2. Export production difference ($\text{gC m}^{-2} \text{yr}^{-1}$) at 100 m (b) and 1000 m (d) between EE-std and EE-noM2.

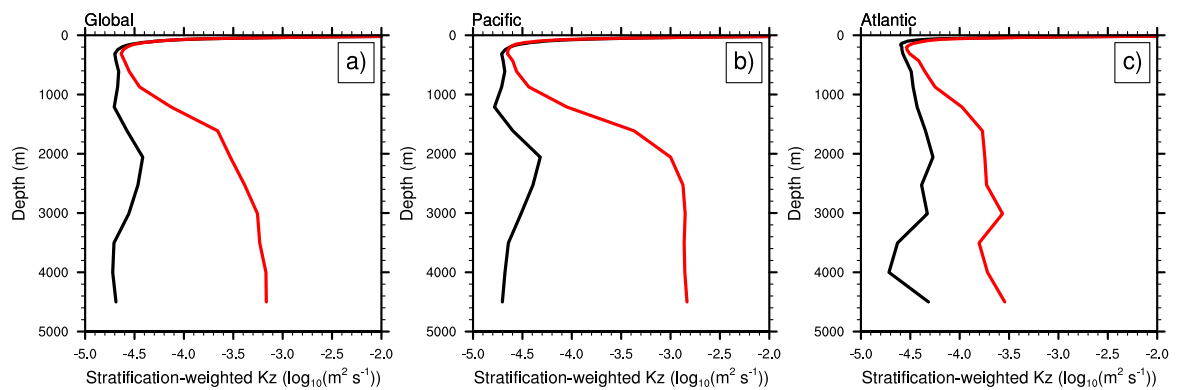


Figure S11. (a) Global, (b) Pacific and (c) Atlantic mean stratification-weighted vertical diffusivity ($\log(\text{m}^2 \text{s}^{-1})$) in EE-noM2 (black) and EE-std (red).

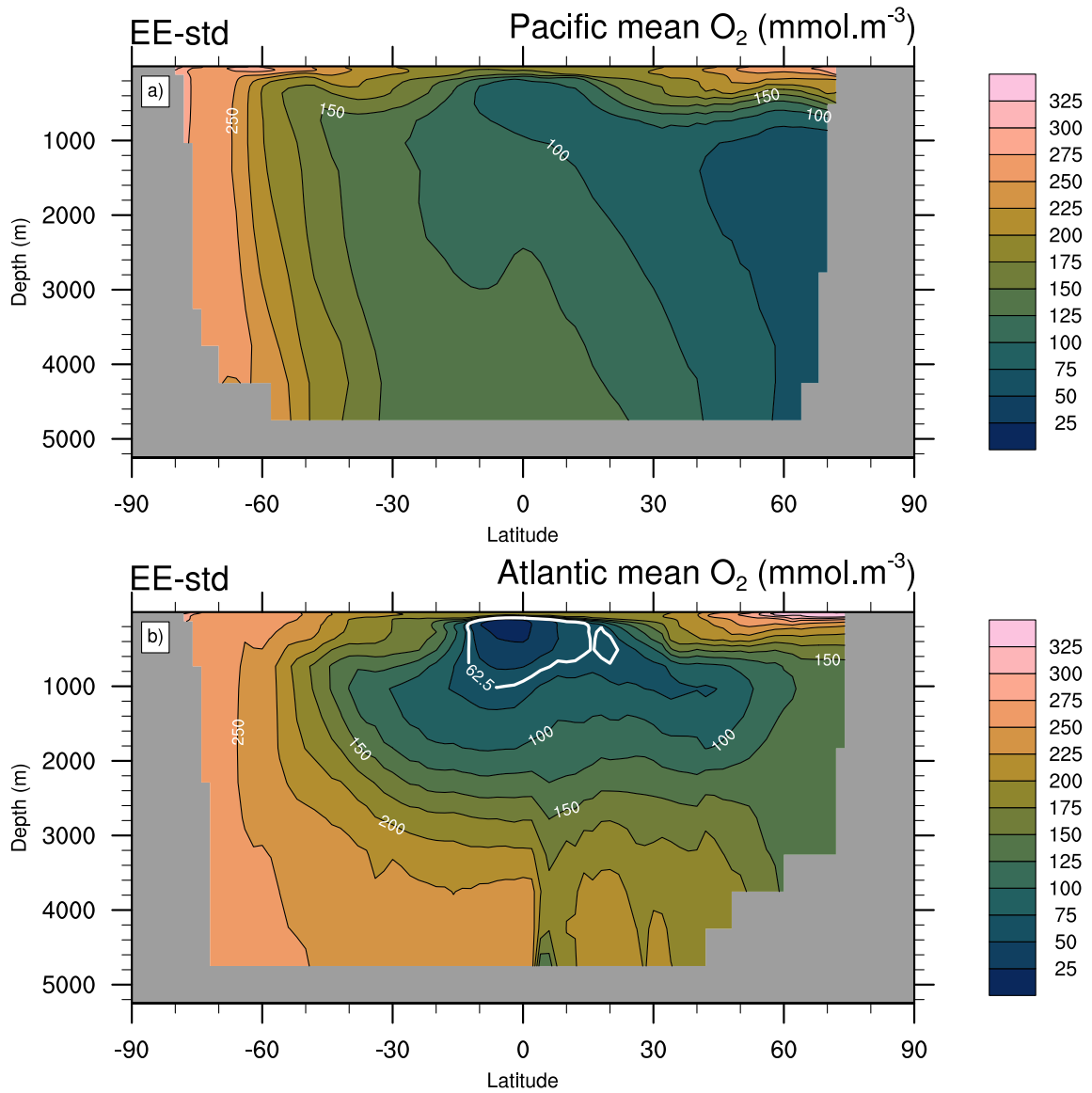


Figure S12. Zonally-averaged (a) Pacific and (b) Atlantic dissolved oxygen concentrations (mmol.m^{-3}) in EE-std. Panel (b) is identical to Fig. 6b.

References

Green, J.A.M., Huber, M., 2013. Tidal dissipation in the early Eocene and implications for ocean mixing. *Geophys. Res. Lett.* 40, 2707–2713. <https://doi.org/10.1002/grl.50510>

Pälike, C., Delaney, M.L., Zachos, J.C., 2014. Deep-sea redox across the Paleocene-Eocene thermal maximum. *Geochem. Geophys. Geosystems* 15, 1038–1053. <https://doi.org/10.1002/2013GC005074>

Xue, P., Chang, L., Dickens, G.R., Thomas, E., 2022. A Depth-Transect of Ocean Deoxygenation During the Paleocene-Eocene Thermal Maximum: Magnetofossils in Sediment Cores From the Southeast Atlantic. *J. Geophys. Res. Solid Earth* 127, e2022JB024714. <https://doi.org/10.1029/2022JB024714>

Xue, P., Chang, L., Thomas, E., 2023. Abrupt Northwest Atlantic deep-sea oxygenation decline preceded the Palaeocene-Eocene Thermal Maximum. *Earth Planet. Sci. Lett.* 618, 118304. <https://doi.org/10.1016/j.epsl.2023.118304>

Zhang, Y., Huck, T., Lique, C., Donnadieu, Y., Ladant, J.-B., Rabineau, M., Aslanian, D., 2020. Early Eocene vigorous ocean overturning and its contribution to a warm Southern Ocean. *Clim. Past* 16, 1263–1283. <https://doi.org/10.5194/cp-16-1263-2020>

Zhou, X., Thomas, E., Rickaby, R.E.M., Winguth, A.M.E., Lu, Z., 2014. I/Ca evidence for upper ocean deoxygenation during the PETM. *Paleoceanography* 29, 964–975. <https://doi.org/10.1002/2014PA002702>

Zhou, X., Thomas, E., Winguth, A.M.E., Ridgwell, A., Scher, H., Hoogakker, B.A.A., Rickaby, R.E.M., Lu, Z., 2016. Expanded oxygen minimum zones during the late Paleocene-early Eocene: Hints from multiproxy comparison and ocean modeling. *Paleoceanography* 31, 1532–1546. <https://doi.org/10.1002/2016PA003020>